

Geomorphic Evaluation of Radar
Imagery of Southeastern Panama
and Northwestern Colombia

by Anthony J. Lewis

B. S., West Chester State College, 1962

M. S., Oregon State University, 1968

Professor in Charge

D. S. Simonett

Committee Members

J. P. Eagleman
Wakefield Dort Jr.
T. R. Smith
R. K. Moore

Conformable Evidences of Kanak Immunity
of Southeastern Palau and
Northern Caroline

SECTION 1000
1000

GEOMORPHIC EVALUATION OF RADAR IMAGERY
OF SOUTHEASTERN PANAMA AND NORTHWESTERN COLOMBIA

by

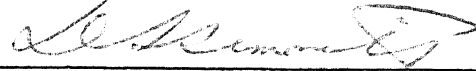
Anthony J. Lewis

B.S., West Chester State College, West Chester, Pennsylvania, 1962
M.S., Oregon State University, 1968

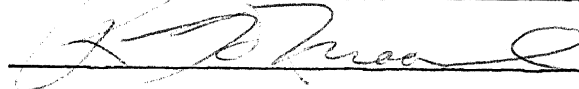
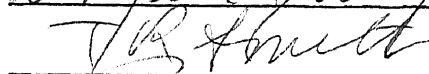
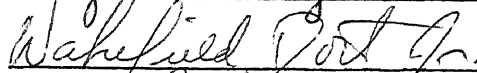
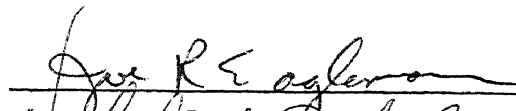
February 1971

Submitted to the Department of Geography
and the Faculty of the Graduate School of
the University of Kansas in partial fulfill-
ment of the requirements for the degree of
Doctor of Philosophy.

Dissertation Committee:



Chairman



MAY, 1971

ACKNOWLEDGEMENTS

This study could not have been completed without (1) the financial sponsorship of Project THEMIS, funded by the Department of the Army, Engineer Topographic Laboratories, Contract No. DAAK02-68-C-0089 granted to the Remote Sensing Laboratory, Center for Research, Inc., (CRINC) University of Kansas; (2) the logistical field support in Panama by the U. S. Army Engineer Topographic Laboratories (USAETL) and the Inter-American Geodetic Survey (IAGS); the technical and secretarial support and intellectual stimulation provided by the personnel at the Center for Research, Inc.; and the moral support by my family.

Recognition is warranted for Col. Alexander Pearson (USAETL) and Sr. Salvador Saldana (IAGS) for aiding me on my "maiden voyage" into the Darien.

Several people at CRINC deserve special recognition. Harold "Granny" MacDonald provided stimulation and encouragement throughout every phase of this study for which I am indebted. Fawwaz T. Ulaby provided assistance at critical times. W. P. Waite gave unselfishly hours of his time for discussion of my many technical problems concerning radar geometry. David E. Schwarz read early drafts and helped with illustration lay-out.

Ralph Gelvin and Stan Phillippe both did excellent jobs in the mensuration and manipulation of my data. Stan also aided in the production of Plates II and III.

The drafting was done mainly by Gary Dunlap, Marilyn Morain, and John Ratzlaff; photographic work by Dwight Egbert and Jim Busse; and typing by Donna Opperman. George Gunnels and Bob Haralick provided assistance when troubles arose in my computer programming. Gary Thomann and George Dalke also provided technical advice.

The critical reading of my dissertation by my committee, especially, Drs. D. S. Simonett, L. F. Dellwig, J. P. Eagleman, and R. K. Moore, was of invaluable assistance in polishing the manuscript. Dr. Simonett, my major professor, as well as making very useful criticisms of my

dissertation ably guided me through my doctorate work. Dr. Dellwig was also of special importance to me during my last two years at the University of Kansas.

To my parents I owe a lifetime of fond memories. To Barbara, my wife who shared the good and bad times while in graduate school, I am indebted for much more than my degree. To my children Sharon, Tony II, Mathew, and our expected June addition, I only hope that you have parents and a wife like I have.

PAX.

TABLE OF CONTENTS

	<u>Page</u>
ACKNOWLEDGEMENT	i
CHAPTER 1 - INTRODUCTION	
1.1 Background	1
1.2 Purpose	3
1.3 Methodology	6
1.4 Anticipated Results	8
CHAPTER 2 - RELATIVE RELIEF AND SLOPE MEASUREMENTS FROM RADAR IMAGERY	
2.1 Introduction	10
2.2 Radar Image Presentation	10
2.3 Relief Displacement	19
2.3.1 Radar Parallax	19
2.3.2 Radar Layover	25
2.3.2.1 Relative Relief Determined from Radar Layover	31
2.3.2.2 Slope Determination from Radar Layover	35
2.4 Radar Power Return	35
2.4.1 Slope Determination from Radar Power Return . .	35
2.5 Radar Shadow	39
2.5.1 Types of Elevated Terrain	49
2.5.2 Relative Relief Determined from Radar Shadows .	54
2.5.3 Slope Determination from Radar Shadows	57
2.5.3.1 Individual Slopes	57
2.5.3.2 Regional Slopes	59
2.6 Radar Foreshortening	61
2.6.1 Slope Determination from Radar Shadows	64
2.6.2 Relative Relief Determined from Radar Shaodws .	65
CHAPTER 3 - QUALITATIVE EVALUATION OF RADAR-DERIVED GEOMORPHIC DATA	
3.1 Introduction	69
3.2 Regional Geomorphology	69
3.2.1 Route 17 Study Area	70

	<u>Page</u>
3.2.1.1 Background	70
3.2.1.2 Radar Geomorphic Regions — Criteria and Delineation	70
3.2.1.3 Topographic-Derived Geomorphic Map	74
3.2.1.4 Comparison of Radar and Topographic- Derived Geomorphic Maps	74
3.2.2 Geomorphic Map of Darien Province	77
3.3 Individual Geomorphic Features	78
3.3.1 Coastal Features within the Study Area	79
3.3.1.1 Shoreline Coastal Configuration	79
3.3.1.2 Tidal Flats	79
3.3.1.3 Mangrove Coasts	82
3.3.1.4 Beach Ridges and Wave Refraction	82
3.3.1.5 Barrier Reefs and Surf Zone	82
3.3.1.6 Shell Reefs	82
3.3.1.7 Non-Vegetated Areas Behind Mangrove Coasts	87
3.3.1.8 Estuarine Meanders	88
3.3.1.9 Delta Features - Atrato Delta	93
3.3.2 Coastal Features Outside of Panama	99
3.3.3 Miscellaneous Features	99
3.3.4 Drainage Basin Analysis	101
3.4 Summary	103

CHAPTER 4 – EVALUATION OF RADAR-DERIVED SLOPE DATA

4.1 Radar Foreshortening	105
4.1.1 Background	105
4.1.2 Methodology	106
4.1.3 Results	107
4.1.4 Explanation and Limitations of Results	115
4.2 Radar Shadow Frequency	118
4.2.1 Background	118
4.2.2 Methodology	118
4.2.3 Results	122
4.2.4 Extension of Radar Shadow Frequency Method into Darien Province	129
4.2.5 Advantages and Limitations of Radar Shadow Frequency Method	131
4.3 Radar Power Return	136
4.3.1 Background	136
4.3.2 Methodology	136
4.3.3 Results	137
4.3.4 Explanation and Limitation of Results	138

CHAPTER 5 - EVALUATION OF RADAR-DERIVED RELATIVE RELIEF
DATA

5.1 Radar Foreshortening	139
5.1.1 Background	139
5.1.2 Methodology	139
5.1.3 Results	140
5.1.4 Explanation and Limitations of Results	149
5.1.5 Recommendations	150
5.2 Radar Shadow.	150
5.2.1 Background	150
5.2.2 Methodology	150
5.2.3 Results	150
5.2.4 Explanation and Limitation of Results	152
5.2.5 Recommendations	152

CHAPTER 6 - SUMMARY

6.1 Conclusions	153
6.2 Recommended Future Work	154

LIST OF FIGURES

		<u>Page</u>
CHAPTER 1		
Figure 1.1	Uncontrolled Radar Mosaic of Study Area (Prepared by Raytheon-Autometrics Corporation). . .	4
Figure 1.2	Location Map of Study Area	5
CHAPTER 2		
Figure 2.1	Radar Image Presentation (Modified from Barr, 1968).	12
Figure 2.2	Relationship of Slant Range to Ground Range (From Beatty, et al., 1965)	14
Figure 2.3	Relationship of Depression Angle (β) to Aspect (Ψ) and Incident (ϕ) Angles when the Terrain is Flat	15
Figure 2.4	Relationship of G_R to S_R with Varying β	17
Figure 2.5	Radar Range Geometry (Modified from Beatty, et al., 1965)	18
Figure 2.6	Relationship of G_r to S_r with Varying β	20
Figure 2.7	Relief Displacement	21
Figure 2.8	Radar Parallax (From Beatty, et al., 1965)	23
Figure 2.9	Radar Layover of Elevated Objects (From Leonardo, 1963)	26
Figure 2.10	Radar Layover as a Function of Depression Angle (β).	27
Figure 2.11	Incident Angle (ϕ)	28
Figure 2.12	Effect of Range Position on Incident Angle Assuming Level Terrain (MacDonald, 1970)	29
Figure 2.13	Effect of Terrain Slopes (α) on Incident Angle (ϕ) . .	30
Figure 2.14	Geometry for Calculating Relative Relief from Radar Layover and Radar Shadow (Modified from Levine, 1960)	32

Figure 2.15	Relationship of Radar Layover (L_R) to Negative Incident Angle ($-\phi$) at a Constant Object Height (h)	34
Figure 2.16	Imaging Conditions Necessary for Determining Terrain Slope (α) from Power Return (P_r)	38
Figure 2.17	Relationship of Radar Shadow (Slant Range Length) with Depression Angle (β)	40
Figure 2.18	Effect of viewing angle on the terrain slope (α). Note as the viewing angle changes from perpendicular, the terrain slope becomes smaller. This relationship is analogous to true and apparent dip	41
Figure 2.19	Relationship of Θ , the angle described by the flight direction and strike of the crestline, with α_b , the true backslope angle of terrain in shadow. This is also a nomogram for correcting the apparent backslope angle to true backslope angle. For example, if a slope at a depression angle (β) and the angle between the flight path and strike of the crestline is 40° , then the true backslope must be greater than 47.5°	43
Figure 2.20	Absolute error in terrain backslope (α_b) as a function of depression angle (β) and the angle described by the flightline and the strike of the crestline (Θ)	44
Figure 2.21	Percentage of error in terrain backslope (α_b) as a function of the angle described by the flightline and the strike of the crestline (Θ) and depression angle (β)	45
Figure 2.22	Simplified Radar Shadow Geometry (From McAnerney, 1966)	46
Figure 2.23	Relationship of S_g to h at a constant β	47
Figure 2.24	Relationship of S_g to β at constant h	48
Figure 2.25	Relationship of the distance on the imagery between equal segments of depression angles with position in the range (After McCoy, 1967)	50
Figure 2.26	Simple Types of Elevated Terrain Features (Modified from Barr, 1968)	52

	<u>Page</u>
Figure 2.27	Radar Shadow Geometry (Modified from Goodyear Aerospace Corporation, 1966) 55
Figure 2.28	Radar Shadow Geometry for Levine's Method (From McAnerney, 1966) 58
Figure 2.29	Relationship of Slope Foreshortening (L_f) with Incident angle (ϕ) on Slant Range Imagery 63
Figure 2.30	Radar Foreshortening Geometry when Using Two Images with the Same Look Direction (From Dalke and McCoy, 1969) 66
Figure 2.31	Radar Foreshortening Geometry when Using Two Look Directions (From Dalke and McCoy, 1969) 66
 CHAPTER 3	
Figure 3.1	Geomorphic regions of Route 17 based on apparent relief and textural appearance interpreted directly from radar imagery 71
Figure 3.2	Radar chips from the four major landform regions in Darien Province, Panama: plains, low hills, high hills, and mountains 73
Figure 3.3	Comparison of radar imagery and topographic maps, Instituto Cartografico Tommy Guardia, Sheet # 11, La Palma, Panama, 1:250,000, 1966 80
Figure 3.4	Radar imagery, tidal flats along Pacific Coast east-central Panama, mouth of Rio La Maestra lower left of imagery 81
Figure 3.5	Radar imagery, beach ridges along Pacific Coast, east-central Panama, mouth of Rio Bayano left center of imagery 83
Figure 3.6	Coral sand islands on leeward slope of barrier reef, surf zone (arrows) outline windward part of reef 83
Figure 3.7	Radar imagery and aerial photograph of shell reefs (1), mangrove (2), and non-vegetated areas associated with semi-dry mangrove coasts (3) east of Garachine in San Miguel Bay 85

Figure 3.8	Conditions near a shell reef and the steps by which a reef may be formed. Stippled pattern represent shell reefs. Arrows indicate the direction of water currents. Irregular line represents shore line (after Grave, 1905).	86
Figure 3.9	Schematic diagram of estuarine meanders.	89
Figure 3.10	Radar imagery and silhouette diagrams, zones of estuarine meanders within stippled areas.	90
Figure 3.11	Location map of estuarine meanders in eastern Panama	92
Figure 3.12	Atrato Delta coastline conditions, 1954	95
Figure 3.13	Comparison between radar imagery (1967) and coastline conditions of 1954	96
Figure 3.14	Vegetation patterns in the Atrato Delta on radar imagery and as mapped by Vann (1959)	97
Figure 3.15	Radar imagery of Atrato Delta illustrating the detection of offshore river mouth bars	100
Figure 3.16	Radar imagery depicting Karst topography in Route 17.	100
Figure 3.17	Map and radar derived drainage pattern of Rio Surcurti Basin in Route 17.	102
CHAPTER 4		
Figure 4.1	Cumulative Frequency Curves of Map-and Radar-Derived Terrain Slope (α) Data — Annamoriah, West Virginia	123
Figure 4.2	Cumulative Frequency Curves of Map-and Radar-Derived Terrain Slope (α) Data — Humbolt Range I, Nevada	124
Figure 4.3	Cumulative Frequency Curves of Map-and Radar-Derived Terrain Slope (α) Data — Humbolt Range II, Nevada	125

Figure 4.4	Cumulative Frequency Curves of Map-and Radar-Derived Terrain Slope (α) Data — Stansbury Mts., Utah.	126
Figure 4.5	Cumulative Frequency Curves of Map-and Radar-Derived Terrain Slope (α) Data — Chrome Ridge-Onion Mtn., Oregon	127
Figure 4.6	Cumulative Frequency Curves of Map-and Radar-Derived Terrain Slope (α) Data — Seven Mile Peak, Oregon	128
Figure 4.7	Radar Imagery of Seven Mile Peak and Chrome Ridge - Onion Mtn., Oregon. Seven Mile Peak area exhibits rounded, difficult to define crests; whereas the crests in the Chrome Ridge-Onion Mtn. area are knife-like, easy to define crests similar to the type of crests found in the other test areas	130
Figure 4.8	Cumulative Frequency Curves of Radar-Derived Terrain Slope (α) Data for Darien Province, Panama - Plains.	132
Figure 4.9	Cumulative Frequency Curves of Radar-Derived Terrain Slope (α) Data for Darien Province, Panama - Low Hills	133
Figure 4.10	Cumulative Frequency Curves of Radar-Derived Terrain Slope (α) Data for Darien Province, Panama - High Hills	134
Figure 4.11	Cumulative Frequency Curves of Radar-Derived Terrain Slope (α) Data for Darien Province, Panama - Mountains	135

LIST OF TABLES

		<u>Page</u>
CHAPTER 2		
Table 2.1	Conditions Necessary for Radar Layover.	31
Table 2.2	Relationship of Terrain Back Slope (α_b) with Depression Angle (β) for the Occurrence of Radar Shadows	39
Table 2.3	Percent Radar Foreshortening (F_p) as a Function of Incident Angle (ϕ)	64
CHAPTER 3		
Table 3.1	Radar-derived geomorphic regions for Route 17	72
Table 3.2	Dudley's physiographic divisions of Route 17	75
Table 3.3	Percentage of areal agreement between Radar- and Topographic-Derived landform maps of Route 17	77
CHAPTER 4		
Table 4.1	Classes Used to Subdivide Radar-Derived Data for Correlation — Regression Analysis.	107
Table 4.2	Correlation and Regression Analysis of Map- and Radar-Derived Terrain Slope (α) Data — Opposite Look Configuration.	108
Table 4.3	Correlation and Regression Analysis of Map- and Radar-Derived Terrain Slope (α) Data — Opposite Look Configuration.	109
Table 4.4	Correlation and Regression Analysis of Map- and Radar-Derived Terrain Slope (α) Data — Same Look, Slope Facing Towards Sensor Configuration.	110
Table 4.5	Correlation and Regression Analysis of Map- and Radar-Derived Terrain Slope (α) Data — Same Look, Slope Facing Towards Sensor Configuration.	111

	<u>Page</u>
Table 4.6 Correlation and Regression Analysis of Map- and Radar-Derived Terrain Slope (α) Data — Same Look, Slope Facing Away From Sensor Configuration. . .	112
Table 4.7 Correlation and Regression Analysis of Map- and Radar-Derived Terrain Slope (α) Data — Same Look, Slope Facing Away from Sensor Configuration. . .	113
Table 4.8 Test Areas for Radar Shadow Frequency Method for Determining Cumulative Frequency Slope Curves . . .	119
Table 4.9 Correlation Analysis of Radar Power Return (P_r) and Topographic-Derived Terrain Slope (α) of Route 17	137
 CHAPTER 5	
Table 5.1 Correlation and Regression Analysis of Map-and Radar-Derived Relative Relief Data — Opposite Look, Slope Facing Sensor Configuration	141
Table 5.2 Correlation and Regression Analysis of Map-and Radar-Derived Relative Relief Data — Opposite Look, Slope Facing Sensor Configuration	142
Table 5.3 Correlation and Regression Analysis of Map-and Radar-Derived Relative Relief Data — Opposite Look, Slope Facing Away From Sensor Configuration . .	143
Table 5.4 Correlation and Regression Analysis of Map-and Radar-Derived Relative Relief Data — Opposite Look, Slope Facing Away from Sensor Configuration . .	144
Table 5.5 Correlation and Regression Analysis of Map-and Radar-Derived Relative Relief Data — Same Look, Slope Facing Away from Sensor Configuration ..	145
Table 5.6 Correlation and Regression Analysis of Map-and Radar-Derived Relative Relief Data — Same Look, Slope Facing Away from Sensor Configuration . .	146
Table 5.7 Correlation and Regression Analysis of Map-and Radar-Derived Relative Relief Data — Same Look, Slope Facing Sensor Configuration	147
Table 5.8 Correlation and Regression Analysis of Map-and Radar-Derived Relative Relief Data — Same Look, Slope Facing Sensor Configuration	148
Table 5.9 Correlation and Regression Analysis of Relative Relief Data Derived from Sampling Topographic Maps and from Radar Shadow Methods	151

LIST OF PLATES

	<u>Page</u>
CHAPTER 3	
Plate I	Regional Geomorphology of Darien Province, Panama and Northwestern Colombia. 165
CHAPTER 4	
Plate II	Radar Landform Classification - Central Darien Province, Panama. 166
Plate III	Radar Landform Classification - Southwestern Darien Province, Panama. 167

CHAPTER 1

INTRODUCTION

1.1 Background

The accurate description of the shape and dimensions of landforms is the first step in any geomorphic study. Although both verbal and quantitative methods of description are functional in landform analysis and should be used to complement each other, morphometry, the mathematical description of landforms, is the more objective and consistent method.

Most geomorphologists will agree that the three most important vertical dimensions used in landform classification and analysis are elevation, relief, and slope. Of the three dimensions, slope is perhaps the cardinal parameter, or at least the most widely used. Quantitative measurements of slope have been used in landform classification schemes (Hammond, 1954; Wood and Snell, 1960); in studies relating landform elements to other physical phenomena (Chorley, 1957; Salisbury, 1962 and 1965; Simonett, 1967; Storie, 1933); in studies relating landform elements to cultural phenomena (Bakhtina and Smirnova, 1968; Glendinning, 1937; Hoag, 1962; MacGregor, 1957; Shaudys, 1956); and in studies of covariance of landform elements (Melton, 1958; Peltier, 1954; Shaudys, 1956; Salisbury, 1962).

To date, assembling slope and other morphometric data has involved the collection and the presentation of data obtained in the field, from topographic maps, and from aerial photography. Now, imaging radar systems are available for testing as an additional source of morphometric data.

Airborne imaging radar systems have several advantages over photographic systems. They can scan a broad swath of terrain (up to 65 km wide) in a single pass, presenting the imaged area on a continuous strip of film closely resembling a shaded relief map. Even at the scale

of 1:500,000 (one inch equals 13 km), the detail is sufficient for mapping at a scale of 1:250,000 (Pierson, et al., 1965). Although the resolution is less than that of aerial photography, the reduction of "ground clutter" or excessive detail increases the interpreter's effectiveness on a macro- and probably a meso-scale. For example, McCoy (1967) found that radar-derived geomorphic data showed a consistent relationship with geomorphic data obtained from 1:24,000 topographic maps. In addition, radar imaging systems have a near all-weather, 24-hour imaging capability, an advantage of special importance for studying areas masked either by darkness (e.g., polar regions) or by clouds (e.g., tropical environments). With these advantages radar may prove to be the primary sensor where field data collection and photography are not practical (MacDonald and Lewis, 1969 a and b).

General applications of radar to the entire geoscience field¹ are dealt with by Beatty, et al., (1965), Simons and Beccassio (1964), Feder (1960), McAnerney (1966), Pierson, et al., (1965), and others. However, in most studies the documentation of the potentials of imaging radar systems for geomorphic analyses has not progressed beyond the stage of speculation.

Levine (1960) and McAnerney (1966) developed methods for determining the spot elevation of an object by measuring the length of the object's radar shadow. Both of the above methods measure the vertical distance of the object from a datum plane and, as such, are measuring relative relief unless the datum plane of the object's base is sea level, at which time the total relief is equivalent to the true elevation. As potential methods of collecting morphometric data from radar, the techniques of Levine and McAnerney are of interest to the geomorphologist and warrant testing.

In a later study Dalke and McCoy (1969) developed and tested a method for measuring terrain slope from radar imagery using the principle

¹For a more complete list of references relating to the applications of radar imagery for geoscience purposes, see R. L. Walters, 1968, "Radar Bibliography for Geosciences," CRES Technical Report 61-30.

of radar foreshortening. They also suggested using the depression angle at which radar shadowing began as an estimate of regional slope.

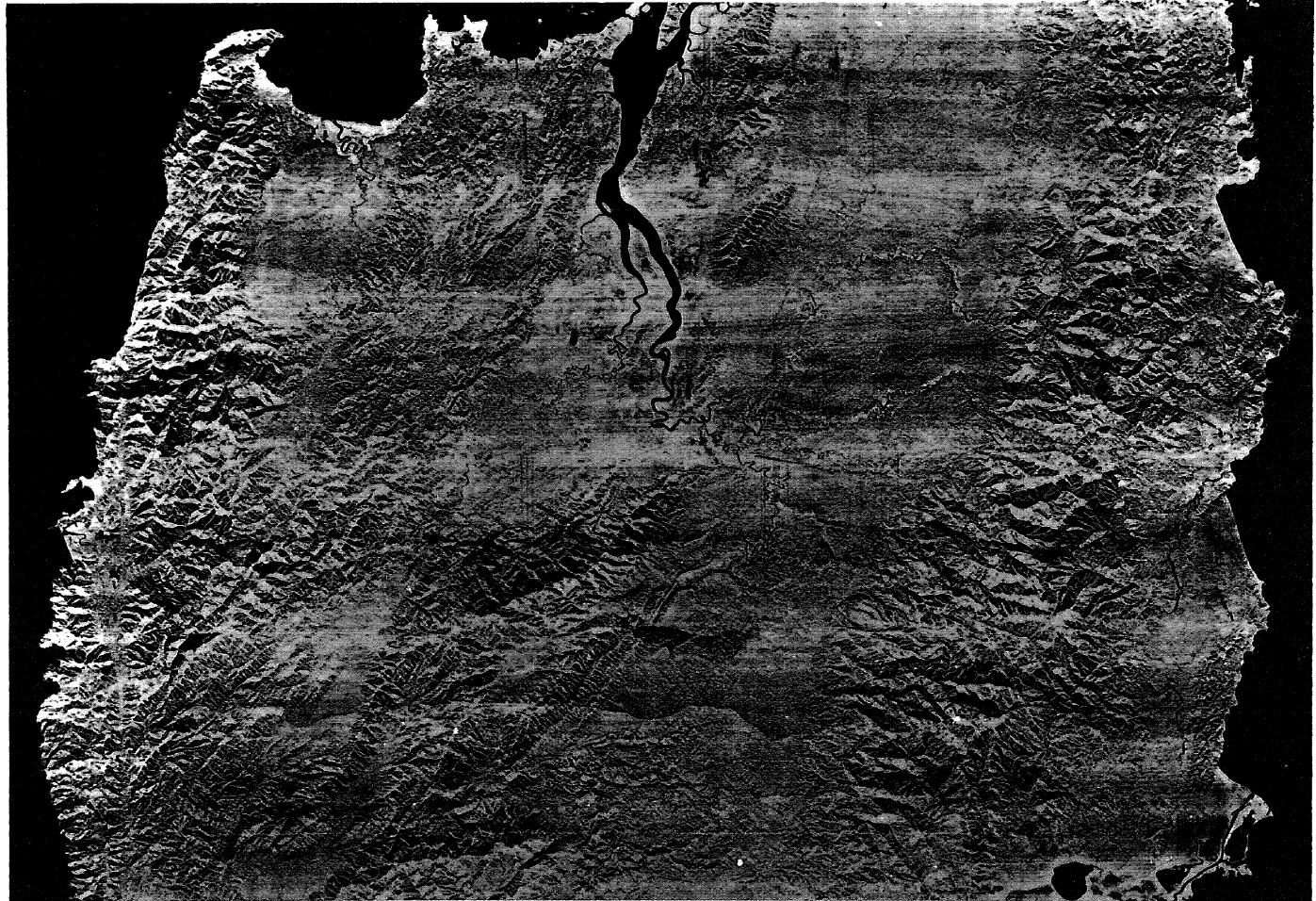
Although the methods employed by Levine and McAnerney for measuring the elevation from a datum plane (actually relative relief) and by Dalke and McCoy for measuring terrain slope are mathematically valid and have been tested experimentally, their operational practicality for regional sized studies has received little or no attention. The recent acquisition of radar imagery flown under Project RAMP (Radar Mapping of Panama) for the purpose of selecting potential sea-level canal routes across the Isthmus of Panama affords the opportunity to test the operational practicality of the techniques available for collecting morphometric data from radar imagery. Under this project the entire Darien Province, the eastern part of the San Blas Province, and the northwestern part of Colombia — over 17,000 square kilometers of terrain — were imaged at four different look directions each approximately 90° apart and at a scale of approximately 1:172,000.¹ Included in the area imaged was Route 17, a proposed sea-level canal route for which a detailed map is available. Route 17 can, therefore, serve as a study area (Figure 1.2) for testing the reliability and consistency of techniques for deriving morphometric data from radar. If the techniques prove reliable, they could be extended into the Darien Province where reliable morphometric data from maps are non-existent. Multiple radar coverage of extensive area in the Darien Province utilizing different look-directions and different depression angles also provides a unique opportunity to test the variance of radar-derived data with changing look-direction and depression angle.

1.2 Purpose

The purpose of this study is to evaluate the potential of radar imagery for use in geomorphic analysis, using southeastern Panama, including

¹An uncontrolled radar mosaic of part of the study area was prepared by Raytheon-Autometrics Corporation (Figure 1.1).

RADAR MOSAIC



DARIEN PROVINCE, REPUBLIC OF PANAMA
AND
NORTHWEST COLOMBIA

Scale: 1:1,000,000

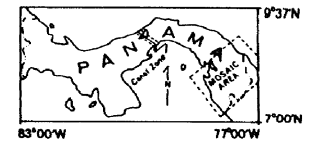


Figure 1.1 Uncontrolled Radar Mosaic of Study area
(Prepared by Raytheon-Autometrics Corporation)

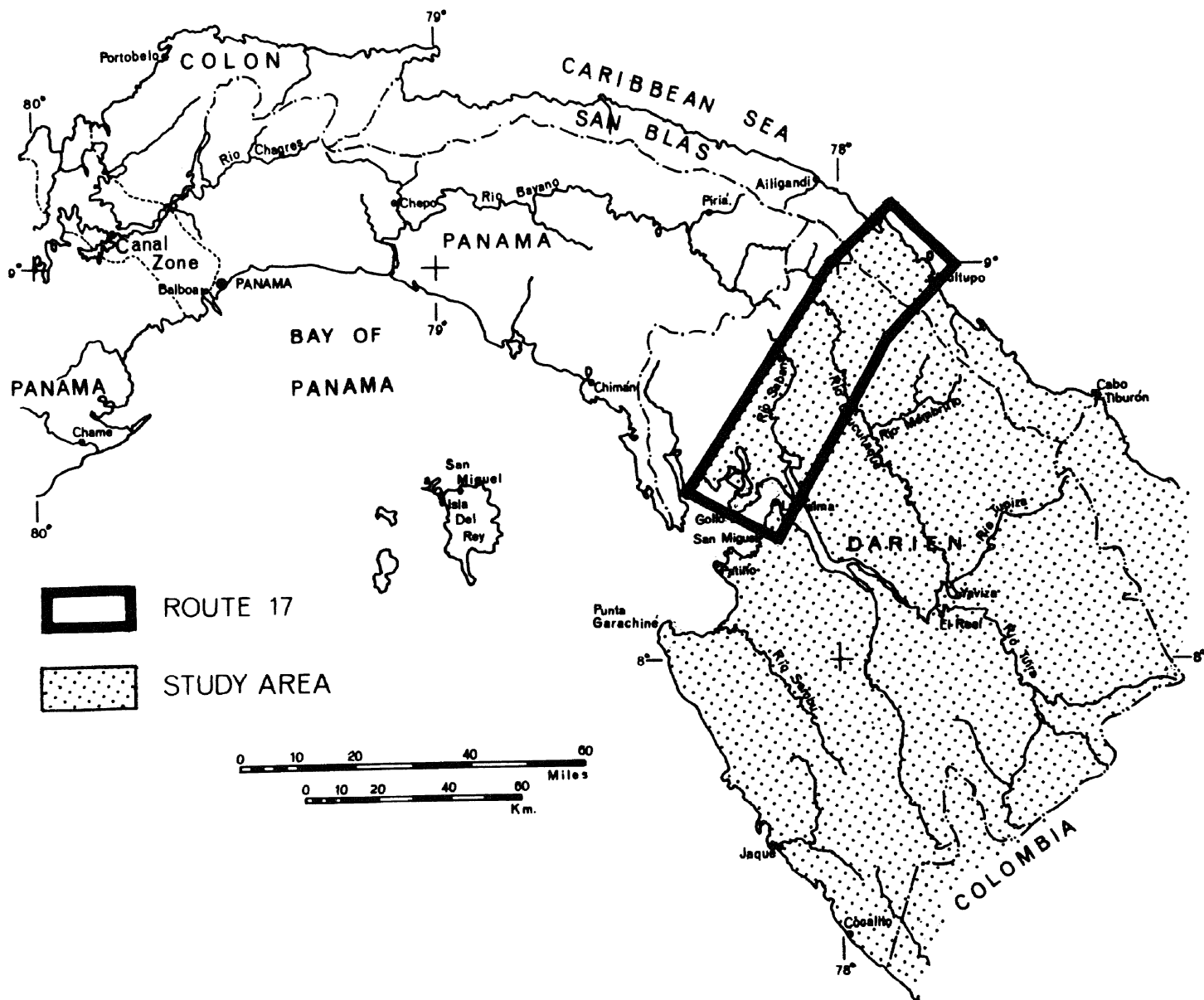


Figure 1.2 Location Map of Study Area

Route 17, and northwestern Colombia as the test site (Figure 1.2). More specifically, radar-derived morphometric data will be compared to morphometric data from 1:50,000 maps of Route 17 and from the limited aerial photography of eastern Panama. The consistency of radar-derived morphometric data will be tested at different depression angles and look-directions. The study is directed at solving the following questions:

- A. What are the radar-terrain conditions necessary for the occurrence of radar shadowing, radar layover, and radar foreshortening?
- B. How does the magnitude or extent of radar shadows, layover, and foreshortening vary with such radar-terrain conditions as depression angle, incident angle, terrain slope, and relative relief?
- C. How may such radar characteristics as radar shadows, layover, foreshortening, parallax, and power return be used for determining terrain slope and relative relief?
- D. What is the value of radar imagery for gathering qualitative geomorphic information on a regional scale?
- E. What is the reliability of the methods by Levine (1960), McAnerney (1966), and the author for determining relative relief from radar shadowing?
- F. What is the operational practicality of the Dalke-McCoy method for measuring slope (actually the average slope for a single terrain slope)?
- G. What is the reliability of using radar shadow frequency to determine the cumulative frequency distribution of slope angles for a given landform region?

1.3 Methodology

A review of the literature disclosed that neither radar geomorphology nor the geomorphology of southeastern Panama and northwestern Colombia

has received the attention they warrant. Accurate maps of the regional geomorphology of the area were nonexistent and only the references previously cited in the introduction elaborate on radargrammetric techniques of any utility to the geomorphologists.

Preliminary interpretations from the radar imagery were made prior to visiting the study area during March and April, 1968. One month was then spent in the Darien area visiting selected areas and collecting field data with logistical support provided by the U. S. Army Corps of Engineers and the Inter-American Geodetic Survey (IAGS) in cooperation with the government of the Republic of Panama. A general reconnaissance of the terrain was made — employing helicopter and fixed wing transportation for aerial reconnaissance as well as piragua (native boats) for river traverses — to help strengthen interpretations and permit extension of information into regions not visited in the field. The dearth of roads and general inaccessibility of the study area kept overland travel to a minimum.

Route 17 was used to test the ability to qualitatively delineate landform regions on radar imagery based on tone and texture. The final product was then compared to a regional landform map (Dudley, 1966) derived from topographic map data. The comparison was favorable and the method was therefore extended into Darien Province where no topographic maps are available at a scale larger than 1:250,000. The final product was a 1:250,000 map of the regional geomorphology of the study area using radar tone and texture as the main parameters, although drainage patterns and densities along with the knowledge accrued during field reconnaissance were incorporated.

Using topographic maps of Route 17 recently constructed by the Army Map Service and radar imagery of the same area, the methods for determining relative relief from radar shadows and terrain slope from radar foreshortening were tested. Morphometric data derived from radar shadow frequency across the entire range of the imagery were compared to similar map extracted data for six areas in the United States. The method was then extended to Darien Province where cumulative frequency curves of

slope were derived from radar imagery for two complete strips across the Province using the landform regions from the geomorphic map of the Darien prepared from radar imagery. This provides a quantitative statement of slope values for the qualitatively described landform regions.

1.4 Anticipated Results

Although this study only incorporates imagery from one radar system,¹ the methods utilizing radar geometry are applicable to all imaging radar systems.² The evaluation of the various methods tested for deriving radar morphometric data however are more equivocal, because of the problems regarding data extraction from the imagery. The discussion of the problems encountered along with the suggestions for system modifications and for improving data collection should provide a springboard for future radar oriented geomorphic studies.

The application of radar-derived data, both qualitative and quantitative, will be demonstrated in the construction of: (1) a map of the regional geomorphology of the entire Darien study area at a scale of 1:250,000 based primarily on macro-texture resulting from radar shadowing; and (2) cumulative frequency slope curves derived from radar shadow frequency for the major landform regions along two bands, each approximately 10 miles wide and 100 miles long (1,000 square miles), traversing the Darien area from the Caribbean Sea to the Pacific Ocean. This is an extraordinary accomplishment when one considers not only the large area involved but also that the standard sources for deriving such data, accurate large scale topographic maps or large scale relatively cloud-free aerial photography, are non-existent for the study area. This illustrates the usefulness of radar imagery as a proxy for topographic maps and aerial

¹Westinghouse side-looking airborne radar (SLAR) imagery operating in the K-band and imaging in slant range.

²Including ground range systems providing the proper transfer factor is applied to convert ground range measurements to slant range.

photography not only for general geomorphic reconnaissance studies but also for collecting quantitative morphometric data for large regions.

There is little doubt that the geomorphic map and accompanying cumulative frequency slope curves represent the most accurate, comprehensive geomorphic data of its kind available for the Darien area. The radar-derived terrain information will provide a strong basis for potential resource studies of this underdeveloped area and will also provide genetic geomorphic information based on previous studies relating slope characteristics to process, structure, lithology, state of development, and relative age of the surface.¹ The potential of radar imaging systems for terrain and resource studies in similar, poorly-mapped environments is also an important outcome of this study.

¹See Zakrzewska (1967) for review and discussion of articles dealing with functional and genetic oriented geomorphic studies.

CHAPTER 2

RELATIVE RELIEF AND SLOPE MEASUREMENTS FROM RADAR IMAGERY

2.1 Introduction

Side-looking radar imagery has not been utilized to the fullest possible extent for measuring relative relief and individual and regional slopes. Radargrammetry has been relegated to a secondary position in relation to photogrammetry largely due to the poorer resolution and a lower order of accuracy of radar imaging systems. However, the widely publicized all-weather advantages of radar systems may act as an acceptable tradeoff for resolution where conditions so warrant, especially in areas where photography is very difficult.

Various theoretical methods for measuring slope angles and relative relief have been devised in the past; however, most of the methods have not been carried beyond the initial stage of discovery. Each of the methods used for determining slope and relief utilizes one of the following characteristics of imaging radar systems:

- (1) relief displacement,
- (2) power return,
- (3) radar shadow,
- (4) radar foreshortening.

2.2 Radar Image Presentation

Depending upon the design of the imaging system, the sweep of the cathode-ray tube (CRT) can be made proportional to slant range or ground range. Being a ranging device, radar records objects in respect to the distance from the aircraft to the object, thus forming a slant range image. Distortions arise from this unique characteristic of recording distance

rather than angle relationships. Figure 2.1 illustrates the slant range distortion. Objects A, B, and C represent objects of equal size in the near, middle, and far range, respectively, i.e., $A = B = C$. Compression of the image is greatest in the near range; therefore on a slant range presentation $A_1 < B_1 < C_1$. The resulting distortion is hyperbolic.

By applying a hyperbolic correction to the sweep of the cathode-ray tube (CRT), an image approximating ground range can be formed. The scale relationship between the image and the ground becomes linear, and $A_2 = B_2 = C_2$ again.

In order to reduce the amount of blank area (area of no-return) on the radar imagery, a time delay (t_o) must be applied to the sweep on the CRT. The delay is proportional to slant range distance where imaging begins and is simply defined as

$$t_o = \frac{2(S_{R0})}{c} \quad (2.1)$$

where

t_o = sweep delay time

S_{R0} = distance in slant range from the aircraft to the terrain
nearest the ground track being imaged

c = speed of light

Making the assumption that the earth is flat and the wavefront describes a straight line, several relationships can be identified between slant range (S_R), ground range (G_R), and aircraft altitude (H). From Figure 2.2 it can be seen that since

$$S_R^2 = H^2 + G_R^2 \quad (2.2)$$

then

$$S_R = \sqrt{H^2 + G_R^2} \quad (2.3)$$

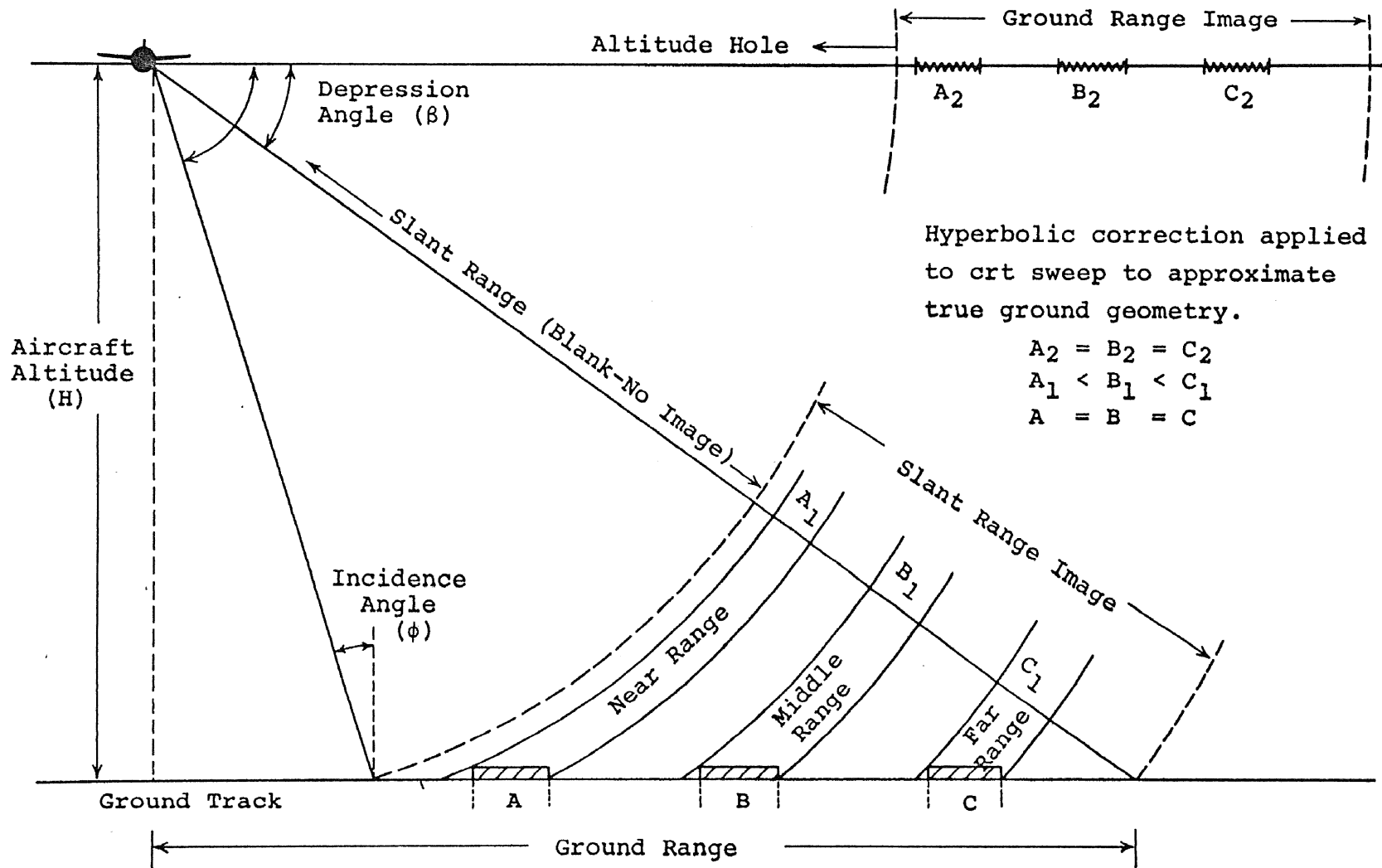


Figure 2.1 Radar Image Presentation
(Modified from Barr, 1968)

and

$$G_R = \sqrt{S_R^2 - H^2} \quad (2.4)$$

The ground range distance can be calculated, therefore, by determining the slant range distance from the slant range markers on the imagery and the aircraft altitude from data obtained during the flight. Also certain trigonometric relationships facilitate radar measurements and can be derived from Figure 2.3. The depression angle (β) is equal to aspect angle (Ψ) and the complement of incident angle (ϕ) when the terrain is level. In mathematical notation,

$$\beta = \Psi \quad (2.5)$$

and

$$\beta + \phi = 90^\circ \quad (2.6)$$

The depression angle also has the following relationships:

$$\sin \beta = \frac{H}{S_R} \quad (2.7)$$

and

$$\cos \beta = \frac{G_R}{S_R} \quad (2.8)$$

Equation 2.7 will become very useful in the later determination of relative relief. Equation 2.8 will be used to illustrate the relationship of ground range to slant range with changing depression angle. This relationship is presented in Figure 2.4 which illustrates that in the far range, i.e., low depression angles, slant range and ground range distance from the aircraft to the target approach unity as the cosine of the depression angle (β) approaches one.

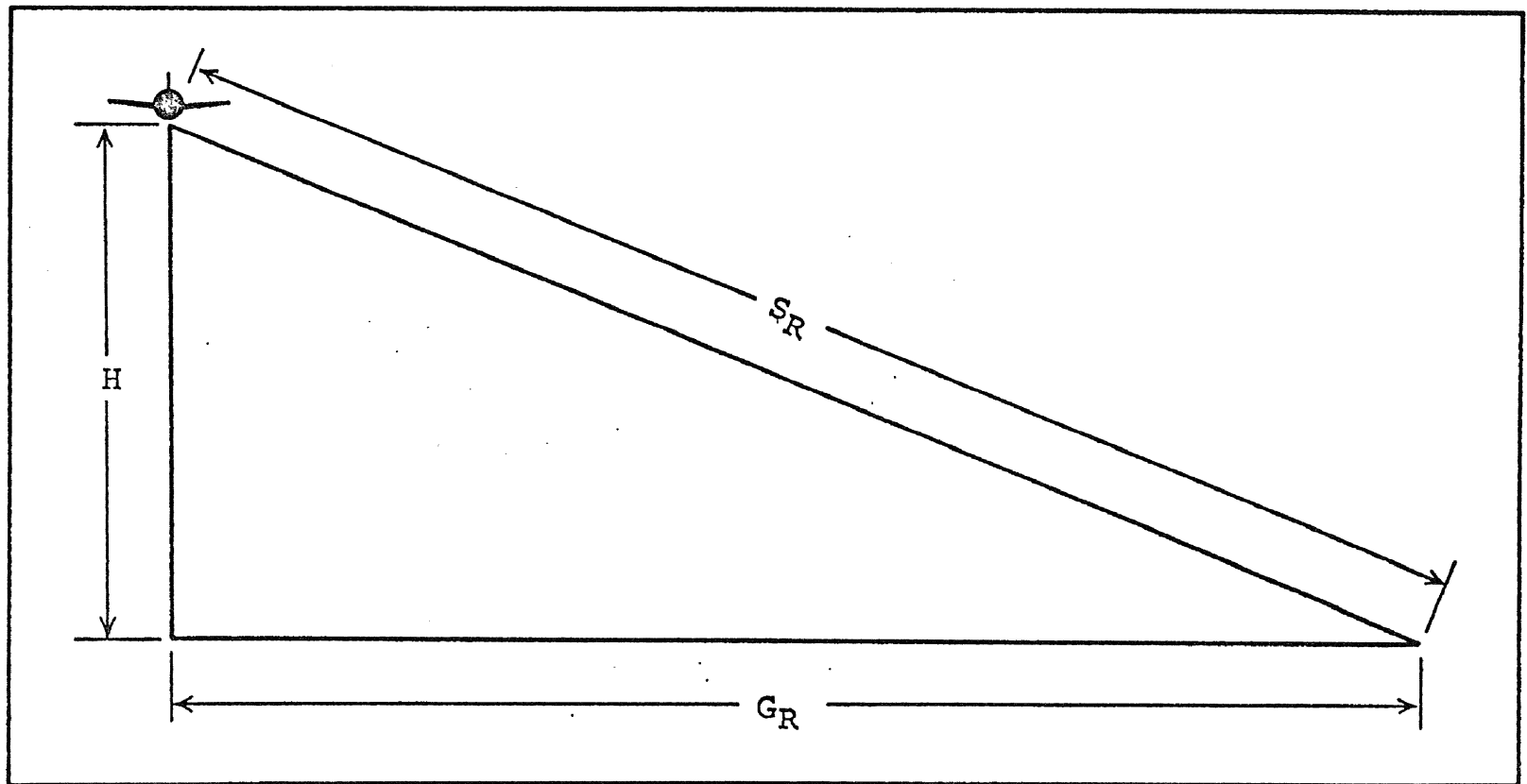


Figure 2.2 Relationship of Slant Range to Ground Range.
(From Beatty, et al., 1965)

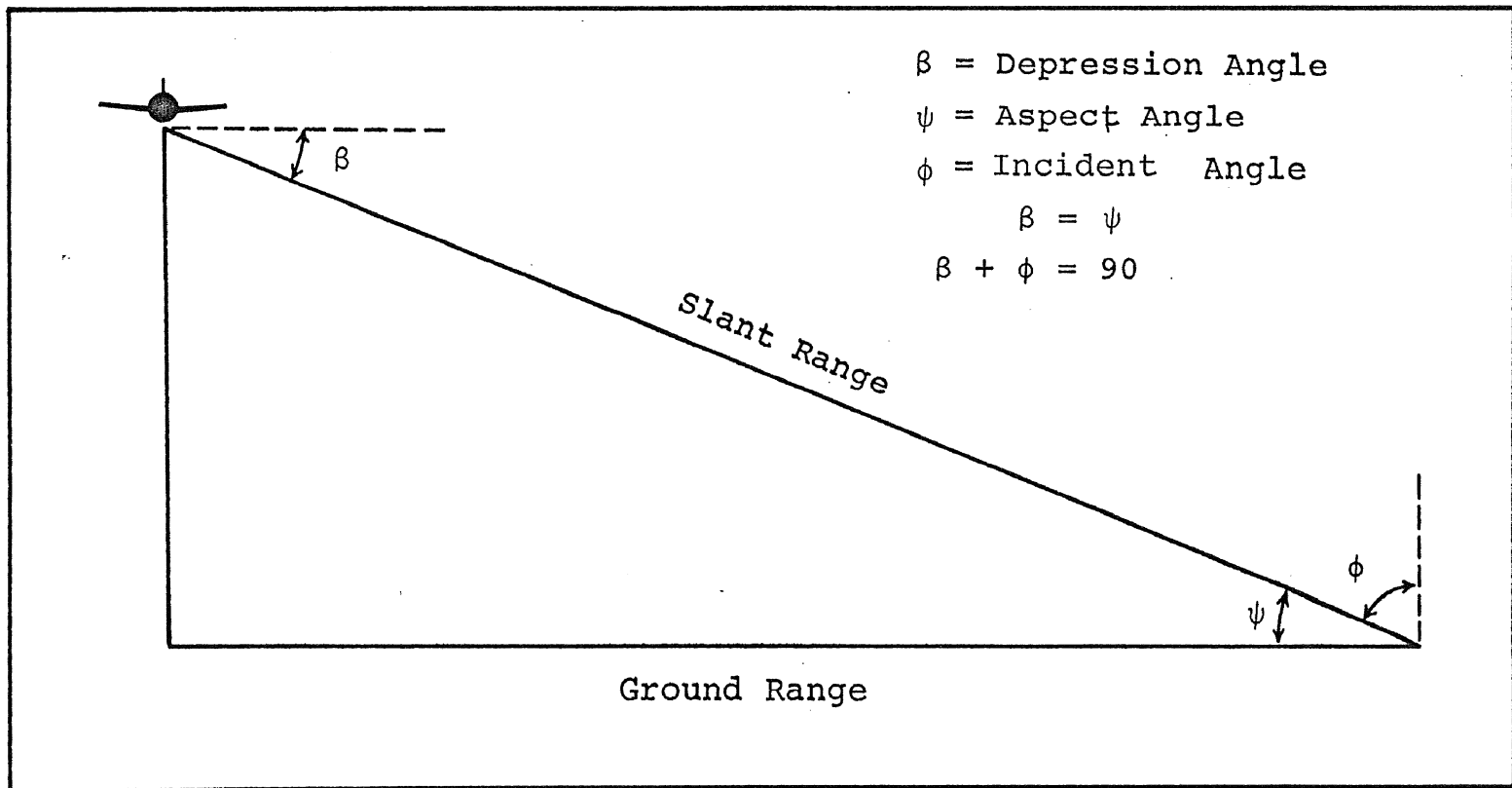


Figure 2.3 Relationship of Depression Angle (β) to Aspect (ψ) and Incident (ϕ) Angles when the Terrain is Flat.

Ground range distance between two objects being imaged is found by the use of similar triangles and Equation 2.4. It can be seen from Figure 2.5 that triangles ABC and CDE are similar and therefore the corresponding sides are proportional. The ground range distance (G_r) between objects at E and C is related to the slant range distance (S_r) between D and C as the slant range distance (S_{R2}) from the aircraft to the object C is related to ground range distance (G_{R2}) from the nadir (B) to C. In mathematical shorthand the relationship is as follows:

$$\frac{G_r}{S_r} = \frac{S_{R2}}{G_{R2}} \quad (2.9)$$

or

$$G_r = S_r \frac{S_{R2}}{G_{R2}} \quad (2.10)$$

It can be seen from Equations 2.8 and 2.9 that the ratio of G_r to S_r is the reciprocal of the ratio of G_R to S_R and is therefore equal to $1/\cos \beta$ or $\sec \beta$.

$$\frac{G_r}{S_r} = \frac{1}{\cos \beta} = \sec \beta \quad (2.11)$$

The distance G_r between points C and E can also be determined using the altitude of the aircraft (H) and the aspect angle (Ψ)¹ at C and E.

From Figure 2.4 it can be seen that

$$\tan \Psi = \frac{H}{G_R} \quad (2.12)$$

or

$$G_R = \frac{H}{\tan \Psi} \quad (2.13)$$

¹Depression angle (β) can also be used since from Equation 2.5, $\Psi = \beta$.

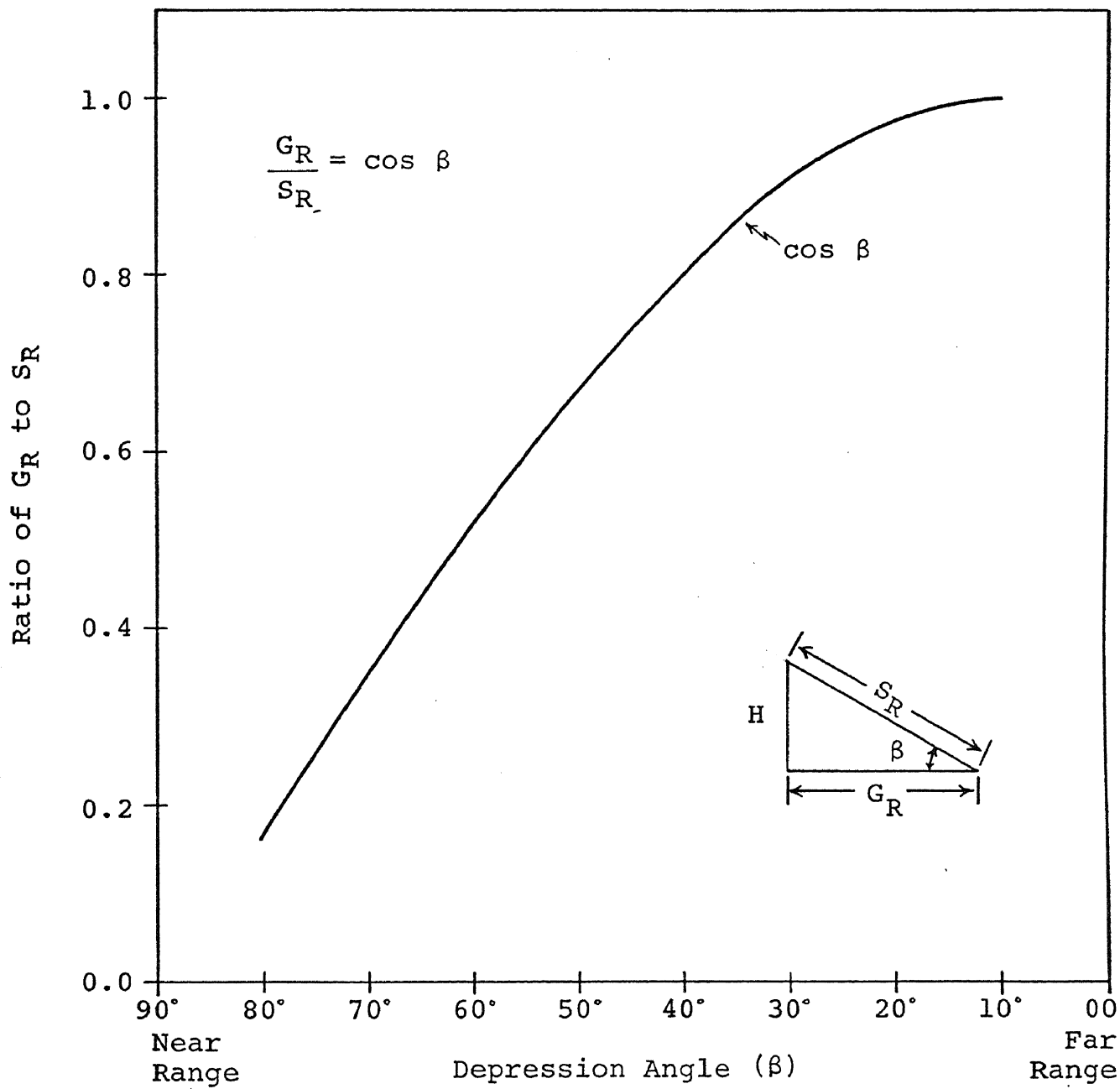


Figure 2.4 Relationship of G_R to S_R with Varying β .

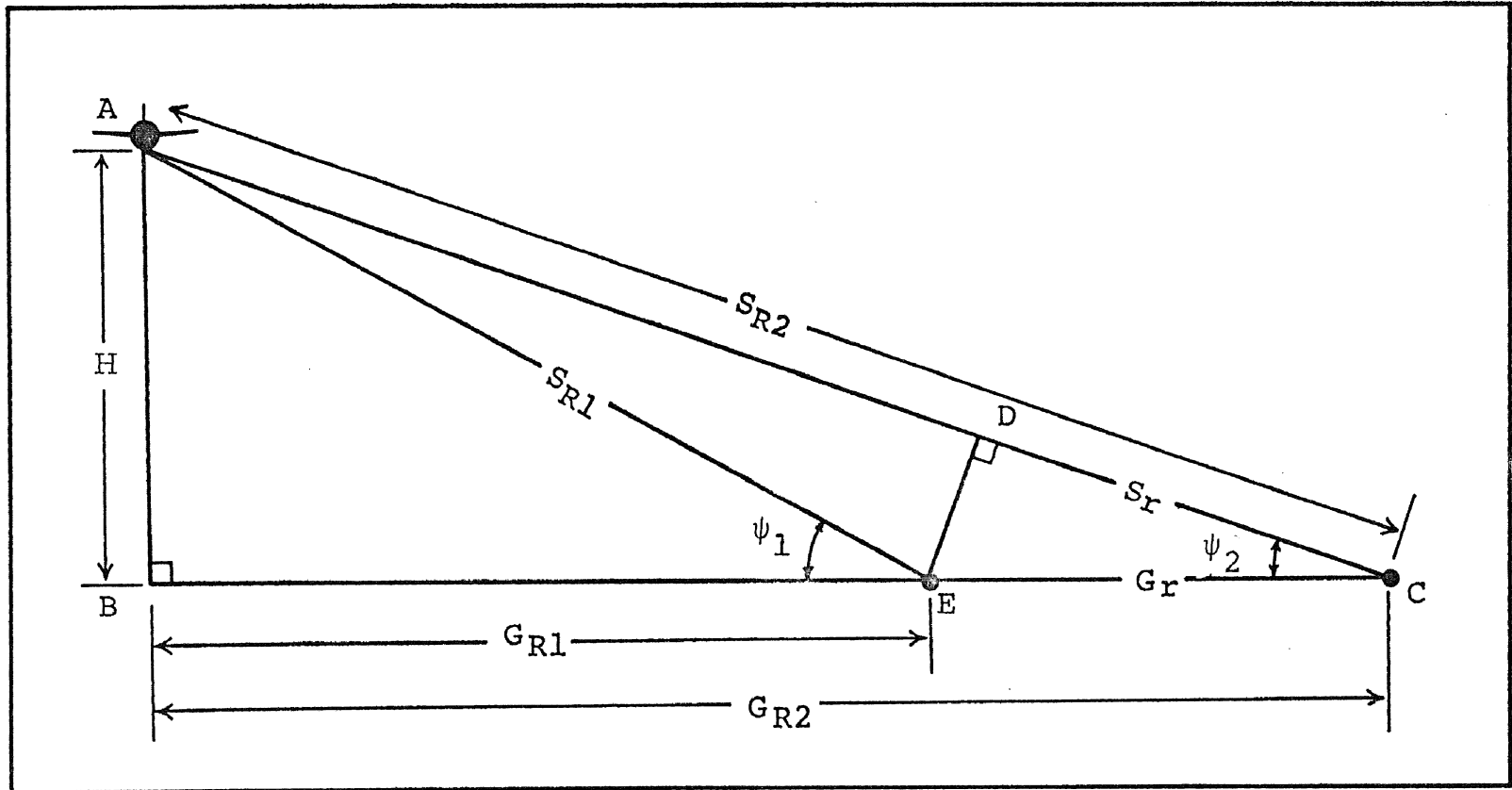


Figure 2.5 Radar Range Geometry. (Modified from Beatty, et al., 1965)

Therefore by solving for G_{R1} and G_{R2} and then subtracting G_{R1} from G_{R2} , G_r can be determined.

$$G_r = \frac{H}{\tan \Psi_2} - \frac{H}{\tan \Psi_1} \quad (2.14)$$

$$G_r = H \left(\frac{1}{\tan \Psi_2} - \frac{1}{\tan \Psi_1} \right) \quad (2.15)$$

$$G_r = H(\cot \Psi_2 - \cot \Psi_1) \quad 1 \quad (2.16)$$

Figure 2.6 illustrates the function of depression angle (β) on the ratio G_r/S_r . Both G_r/S_r and G_R/S_R approach unity as the depression angle decreases; however, they approach each other from the opposite direction. Whereas, G_r/S_r decreases to one with decreasing β , G_R/S_R increases to one with decreasing β .

2.3 Relief Displacement

2.3.1 Radar Parallax

Radar relief displacement is an inherent characteristic of side-looking imaging radar systems and is towards the nadir if the object is above the datum (topographic high) and away from the nadir if the object is below the datum (topographic low). The relief displacement, therefore, is in the opposite direction from the displacement direction in optical camera systems (Figure 2.7).

¹Although G_r in this equation specifically refers to the ground range distance between points C and E, the same equation can be used to determine the swath width if the depression angle is known for the extreme far and near ranges.

Note: This equation (G_r/S_r) is approximate and applies only to very short distance. The full formula over longer distances is $G_r/S_r = \sec \beta + \tan \beta$.

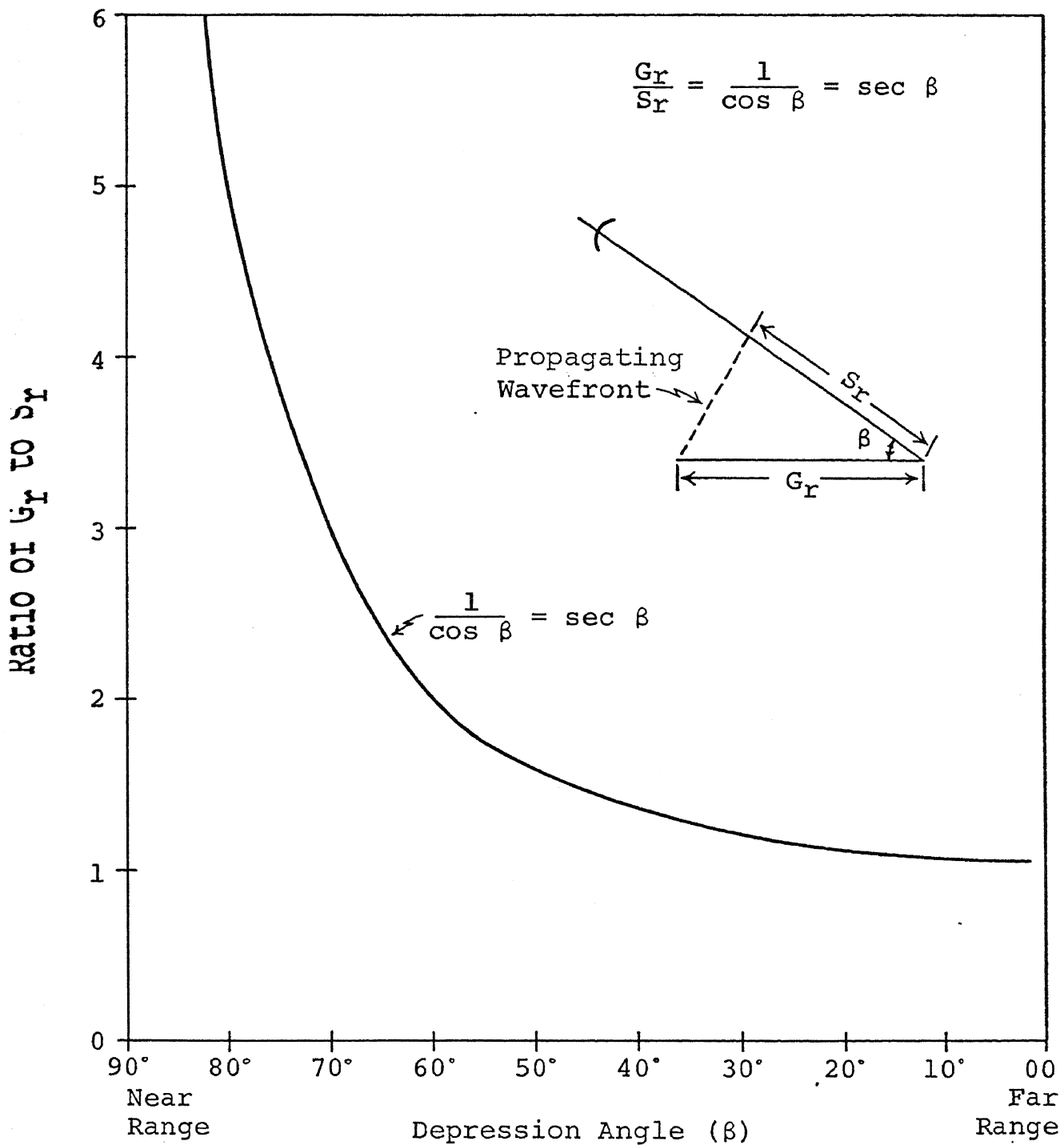


Figure 2.6 Relationship of G_r to S_r with Varying β .

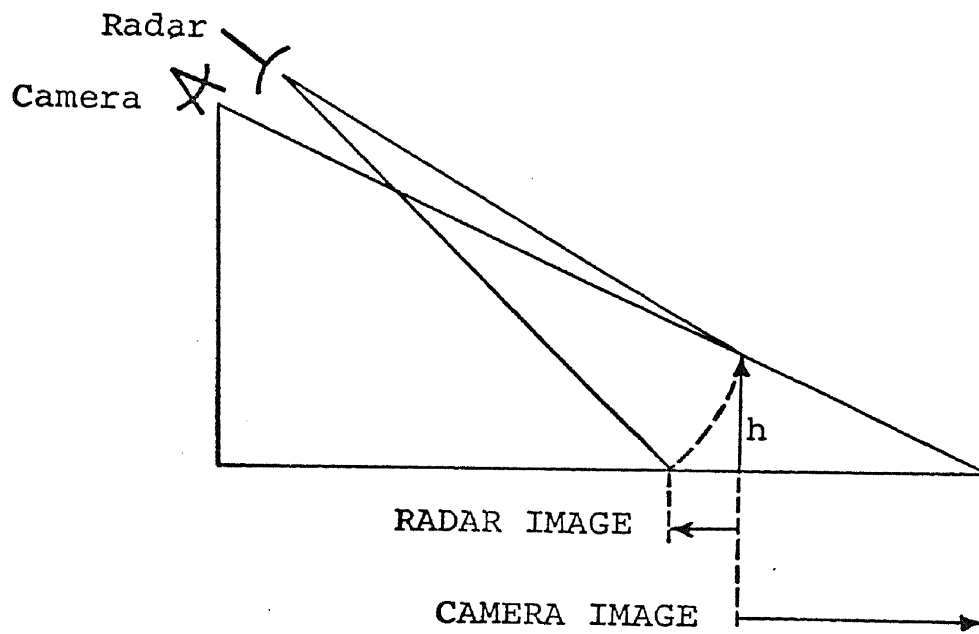


Figure 2.7 Relief Displacement.

When one object is imaged twice at two different look-directions, i.e., opposite side configuration (Figure 2.8A), or two different altitudes, i.e., same side configuration (Figure 2.8B), then radar parallax can be measured and radar stereoscopy attained. Radar parallax is defined as the sum of the displacement of the object on the two images (Beatty, et al., 1965). Levine (1960) shows the development of the parallax triangle along with the uses of radar parallax, a subject to be covered subsequently. LaPrade (1963) in an experimental study of radar stereoscopy, illustrates the effect of flight configuration on radar parallax and defines the optimum flight configuration for opposite-side and same-side radar stereoscopy.

Several equations have been derived by Levine (1960, pp. 166-169) to determine the elevation above a datum plane from the parallax of an elevated target that is encountered with double coverage of side-looking radar systems. Relative relief determination can be made from the radar parallax of elevated objects resulting from flights flown (1) in opposite look-directions, but the same altitude and (2) at different altitudes but the same look-direction.

When opposite look-directions are used to derive measurements of the elevation above a datum plane (h) from parallax magnitude (p) and ground range distance to the target (G_R), the solution is accomplished by the following equation (Levine, 1960, p. 168):

$$h = H - \sqrt{H^2 - \frac{2pG_{R1}G_{R2}}{b}} \quad (2.17)$$

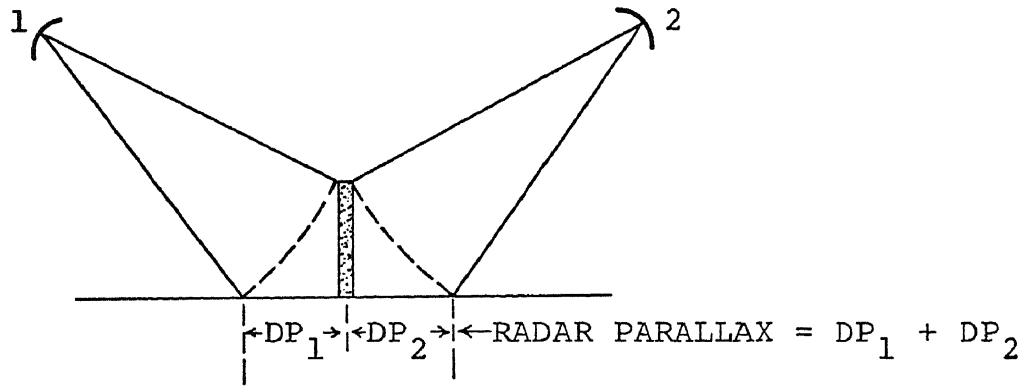
if

$$G_{R1}^2, G_{R2}^2 \gg h(2H-h)$$

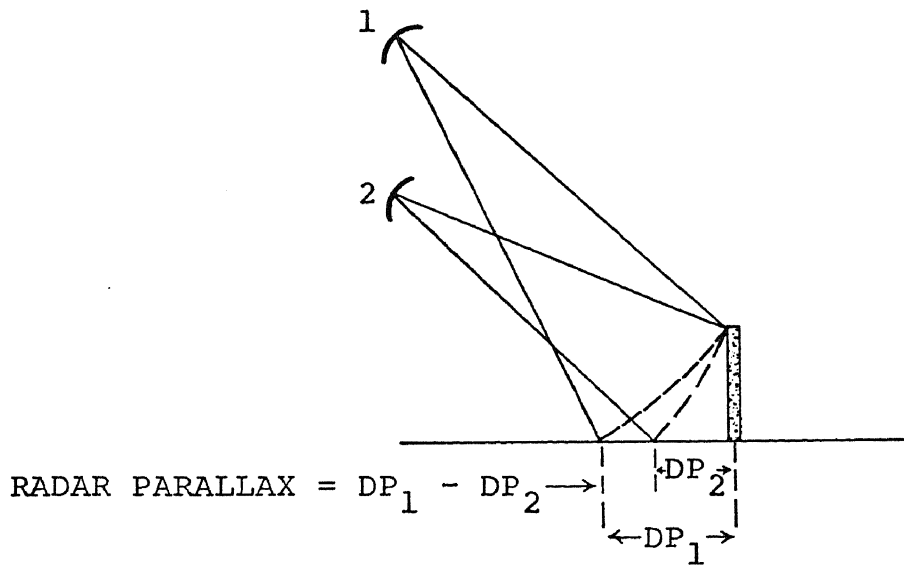
where

- (1) p is the parallax magnitude (Figure 2.8)
- (2) b is the distance between the nadir of the two flights
- (3) G_R is the ground range distance to the object and is equal to

Equation 2.4, $\sqrt{S_R^2 - H^2}$



(A) OPPOSITE SIDE CONFIGURATION



(B) SAME SIDE CONFIGURATION

Figure 2.8 Radar Parallax. (From Beatty, et al., 1965)

- (4) H and h are the height of the aircraft and elevation of the target, respectively.

When the flights have the same look-direction but are flown at different altitudes, the determination of elevation is not as involved as in the previous case, being reduced to

$$h = \frac{p(G_R)}{\Delta H} \quad (2.18)$$

where

- (1) ΔH is the difference between the H_1 and H_2
- (2) the rest of the parameters are the same as previously defined (Levine, 1960).

Shadow parallax (p_s) can also be used for elevation determinations; however, the equation which gives elevation in terms of shadow parallax would be unwieldy and require numerous unnecessary measurements and calculations when compared to another method involving only radar shadow which produces the same result. For example, the measurement of shadow parallax (p_s) requires (1) overlapping flights, (2) the finding and measuring of radar shadow of the object on each of the overlapping strips of radar imagery, and (3) the calculation of shadow parallax; whereas, the radar shadow method requires only one imaging flight and one measurement. Although the accuracy of the two methods has not been tested, and theoretically the accuracy is the same, the practical application of the shadow parallax method is less, the source of error is greater, and the calculation of height is more involved. For these reasons, shadow parallax is not considered to be a functional method for elevation determination.

Primarily, radar parallax appears to be useful when conditions negate the use of radar shadows, such as where shadows are non-existent or are cast on highly sloping terrain.

2.3.2 Radar Layover

Radar layover is an extreme case of relief displacement. By measuring range, the placement of an object or part of an object on the imagery becomes a direct function of the distance from the aircraft to the object. In certain cases the top of an object is closer to the aircraft than the bottom and therefore is recorded sooner. Figure 2.9 demonstrates this principle. Points B, C, D, E, and F are presented on radar imagery in relation to the time at which each is intercepted by the spherical wavefront generated by the radar system in the aircraft (A).

The first point detected by the wavefront is B, and it would be recorded first on the image. As the wavefront progresses across the terrain, point C is intercepted and recorded; however, point D is also intercepted at the same time as C and therefore both are recorded simultaneously. Points E and F are also recorded together but at a later time than C and D. The result is that the top of the feature is presented before the base of the feature. In all probability, the return from C and D, and from E and F are not distinguishable from each other and thus are in a sense lost to the interpreter. The sequence at which the points along the terrain are imaged produces an image that appears inverted.

Radar layover is not dependent upon the absolute distance from the aircraft to the feature, but rather the difference in slant range distance between the top and the bottom of the feature (Figure 2.10). This is in turn a function of (1) the wavefront angle, which is related to the depression angle or the position in the slant range and, (2) the slope of the terrain or object. Figure 2.10 also illustrates that radar layover is most prevalent in the near range, i.e., high depression angles, and where terrain slope is steep.

Incident angle, the angle formed by the radar beam and the perpendicular to the object's surface at the point of incidence (Figure 2.11) is of prime concern when the conditions for radar layover are defined. Figures 2.12 and 2.13 illustrate the two parameters that affect incident angle. Figure 2.12 demonstrates the increase in incident angle from near to far range, providing the terrain slope is constant. However,

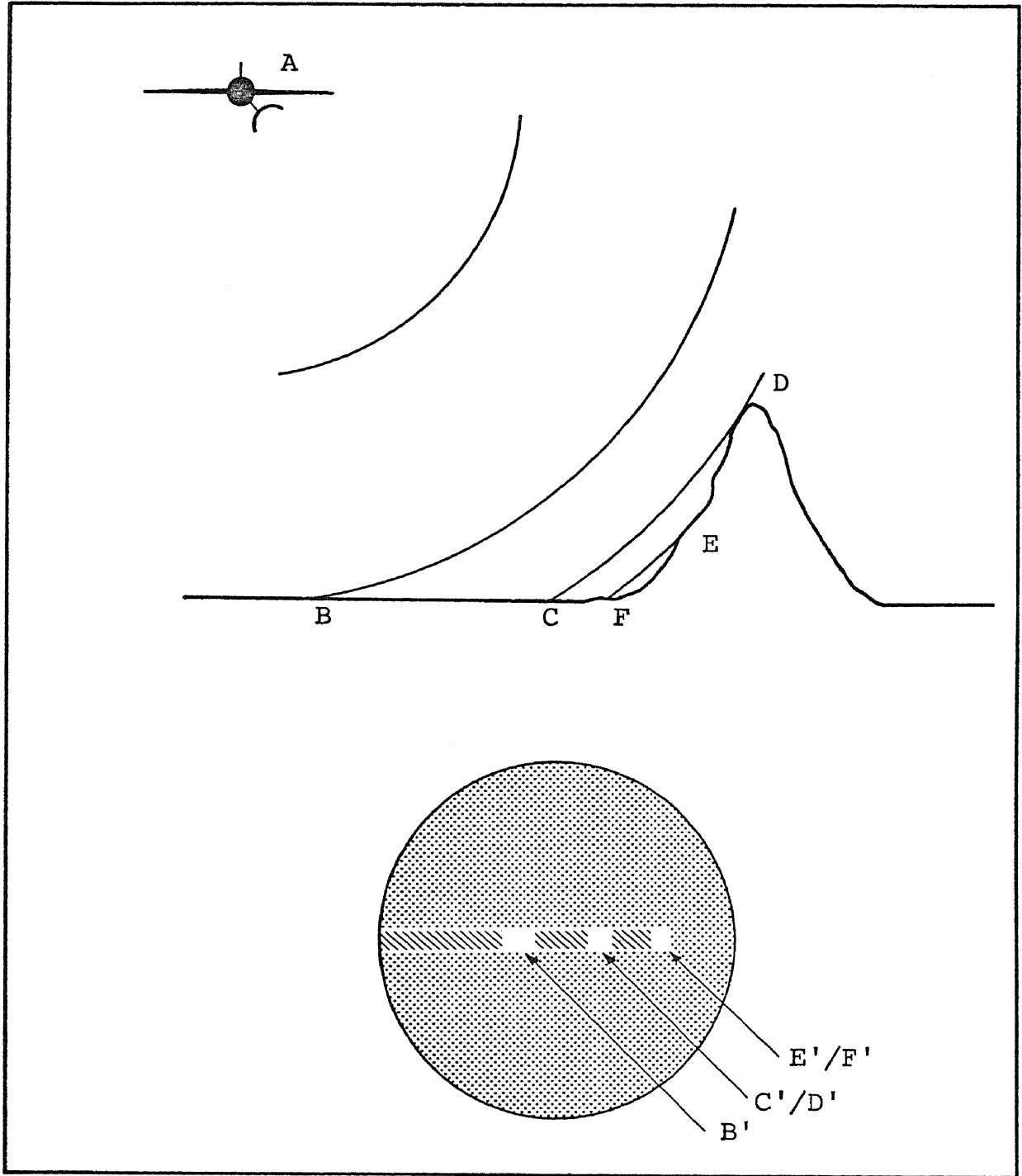


Figure 2.9 Radar Layover of Elevated Objects. (From Leonardo, 1963)

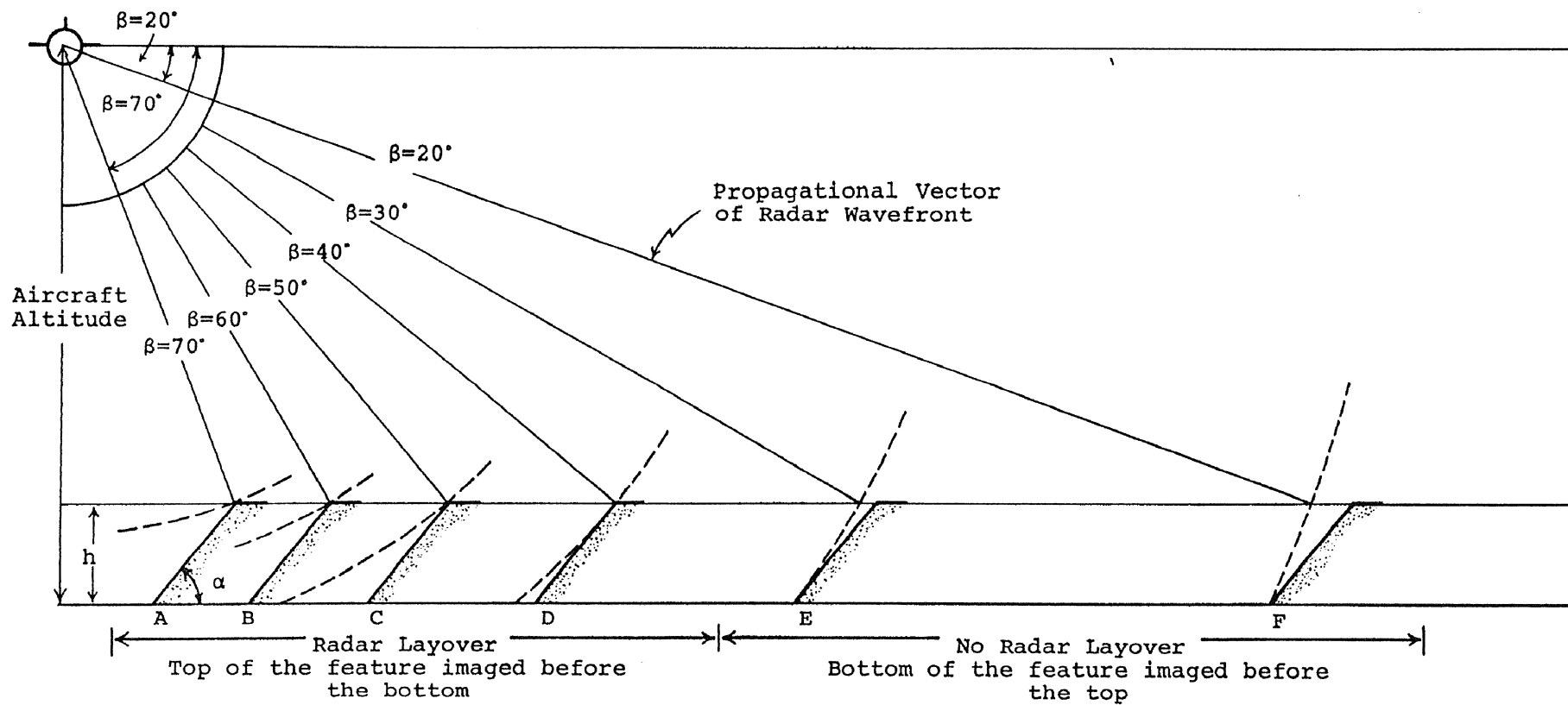


Figure 2.10 Radar Layover as a Function of Depression Angle (β)

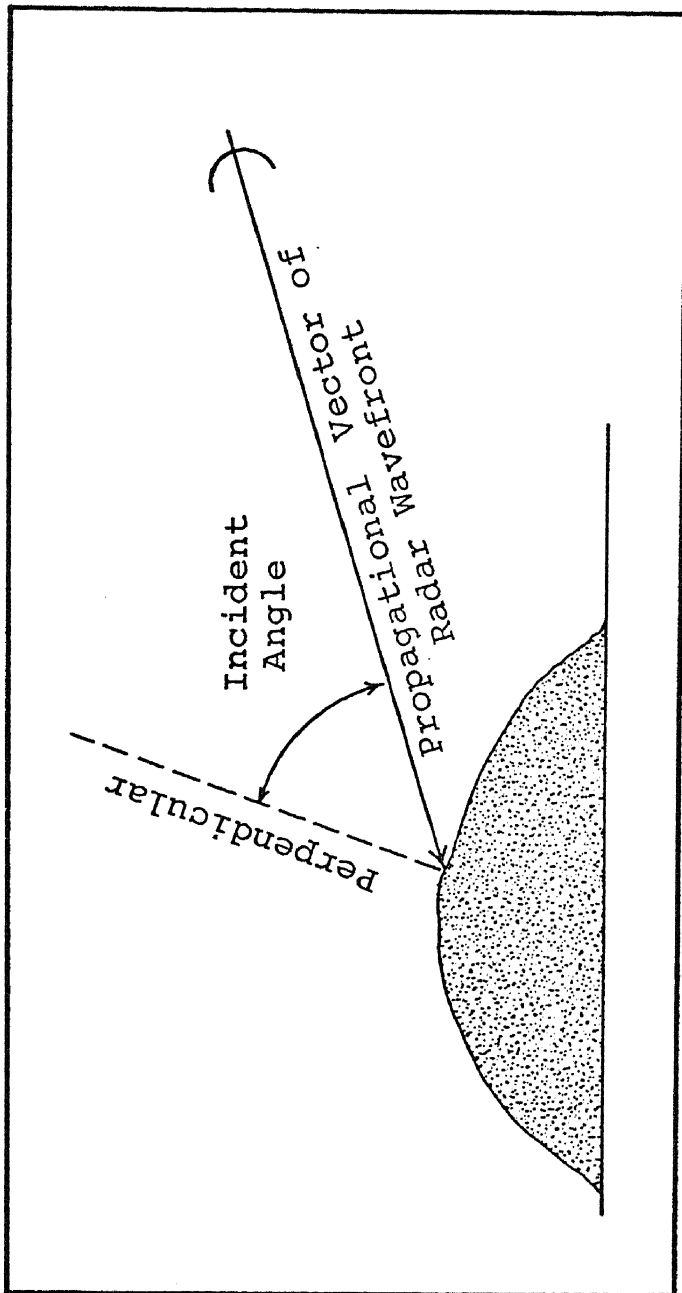


Figure 2.11 Incident Angle (ϕ).

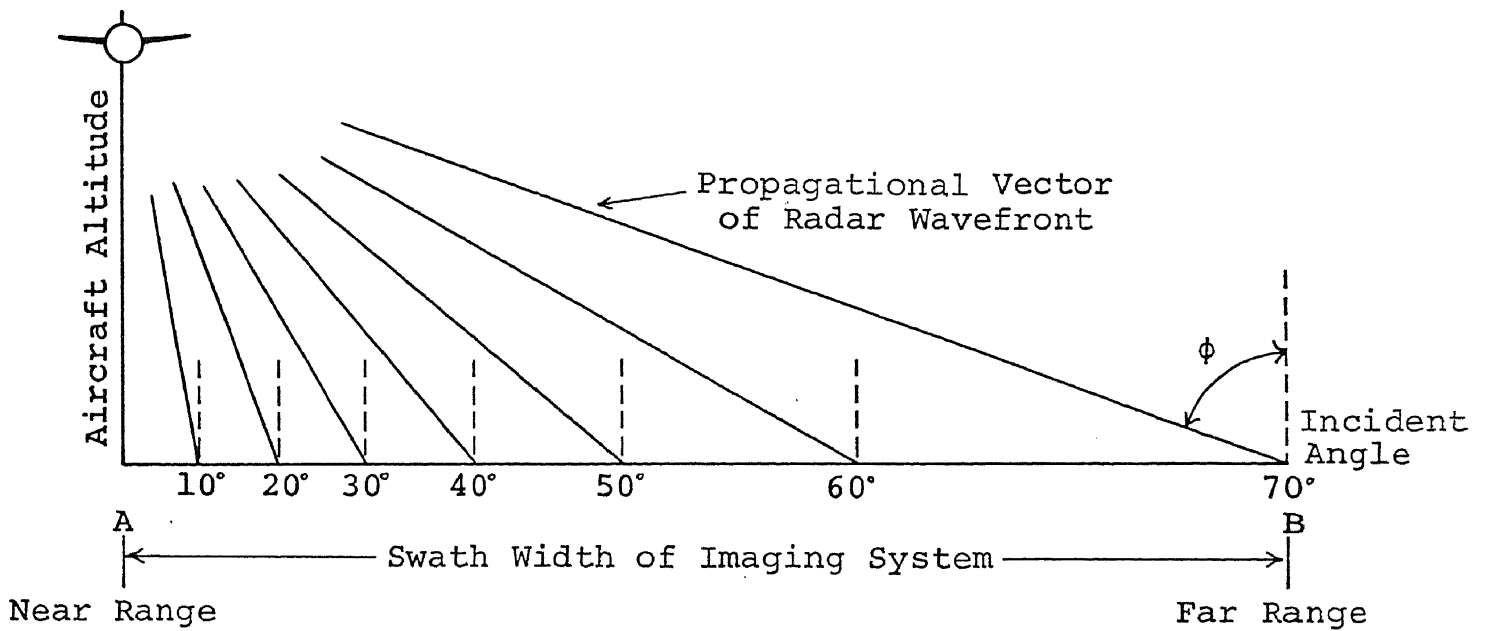
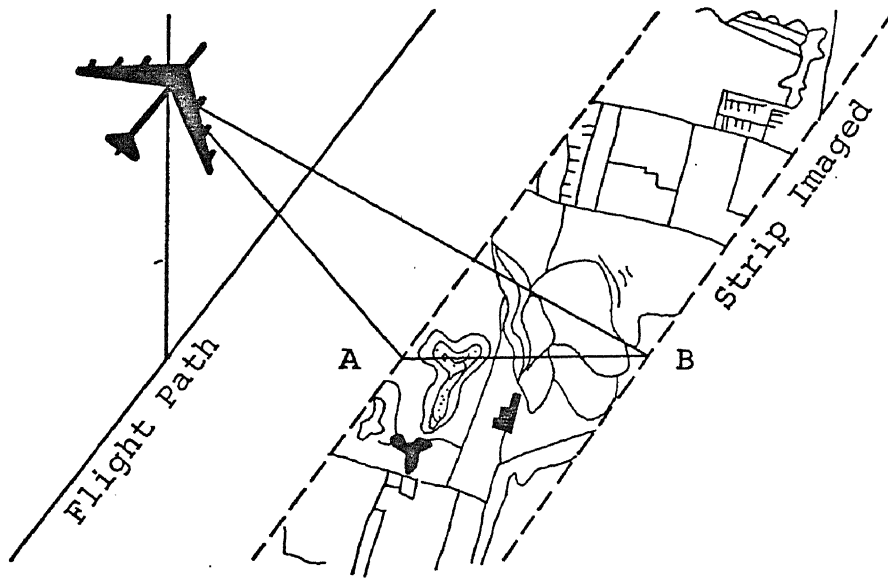


Figure 2.12 Effect of Range Position on Incident Angle Assuming Level Terrain (MacDonald, 1970).

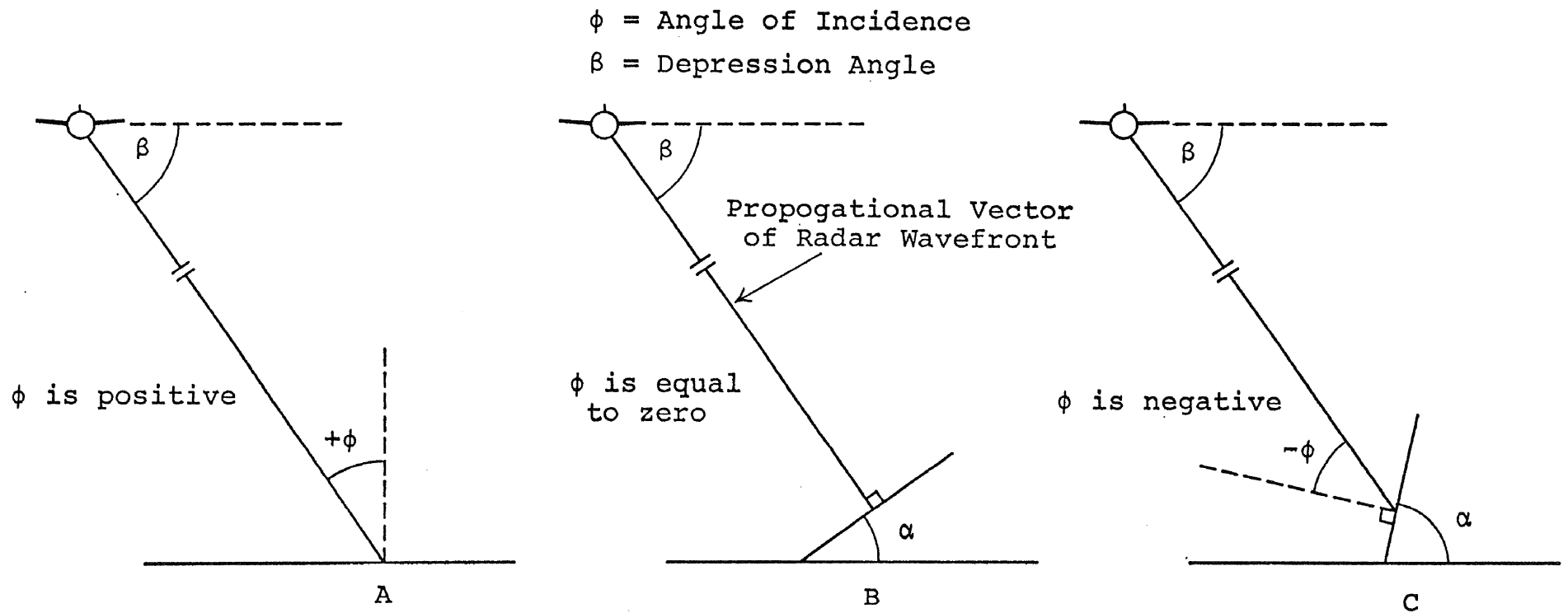


Figure 2.13 Effect of Terrain Slopes (α) on Incident Angle (ϕ).

assuming a constant position in range and therefore a constant depression angle (β), a decrease in incident angle with increasing terrain slope is evident in Figure 2.13.

For simplicity, if we assume the wavefront to be a straight line,¹ then it can be stated that radar layover is encountered when and only when the incident angle is negative as illustrated in Figure 2.12C. Therefore, the most probable case for radar layover is where steep slopes are found in the near range (Figure 2.12A). The conditions for the existence of radar layover are more definitive in Table 2.1, in terms of depression angle (β) and terrain slope (α).

TABLE 2.1
CONDITIONS NECESSARY FOR RADAR LAYOVER

Terrain Slope (α)	Depression Angle (β)	Incident Angle (ϕ)
>80°	10° Far Range	Negative
>70°	20°	Negative
>60°	30°	Negative
>50°	40°	Negative
>40°	50°	Negative
>30°	60°	Negative
>20°	70°	Negative
>10°	80° Near Range	Negative

2.3.2.1 Relative Relief Determined From Radar Layover

LaPrade and Leonardo (1969), using several assumptions, developed the equations for using radar layover (L_R) to determine the height of a feature above a datum plane (h).² The assumptions are as follows:

- (1) the target is at a great distance from the radar compared to the height of the target (Figure 2.14A),
- (2) the wavefront impinging on the target describes a plane (see Figure 2.14B).

¹A reasonably valid assumption when the distance to the target is large as is usually the case.

²This is really relative relief (R_R) unless the datum plane is sea level.

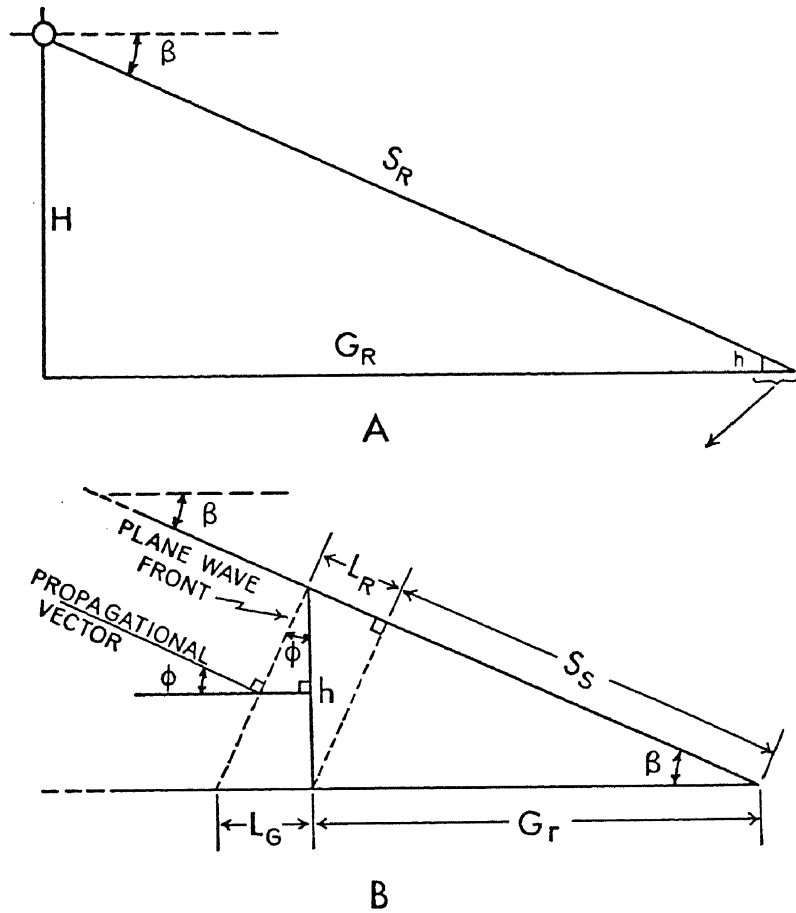


Figure 2.14 Geometry for Calculating Relative Relief from Radar Layover and Radar Shadow.
(Modified from Levine, 1960)

Referring to Figure 2.14B and using similar triangles, LaPrade and Leonardo (1969) stated that

$$\frac{h}{L_R} = \frac{S_R}{H} \quad (2.19)$$

or

$$h = L_R \frac{S_R}{H} \quad (2.20)$$

where h and L_R have already been defined and S_R is the total slant range distance and H is the aircraft's altitude.

From Figure 2.14B, the relationship of a radar layover (L_R), measured in the slant range, to the incident angle (ϕ) can be derived and stated as $L_R = f(\phi)$. Mathematically this relationship is represented in Figure 2.15 and defined in Equation 2.21.

$$L_R = h \sin(-\phi) \quad (2.21)$$

where ϕ is restricted to the fourth quadrant, between 270° and 360° , if measured clockwise, or from 0° to -90° if measured counter-clockwise. As previously stated, a prerequisite for radar layover is that ϕ be negative, as defined in Figure 2.13; therefore, ϕ will be measured in a counter-clockwise fashion as the perpendicular of the terrain slope varies with the propagational vector of the radar beam (Figure 2.14B).

Although this method is theoretically sound, it has several limitations: first, in the more optimum portion of the imagery, that is, the middle and far range, radar layover is a rare occurrence; second, the physical measuring of radar layover on imagery of natural terrain is extremely difficult since the backscatter coefficient from the top of the object is usually the same as the radar return from the base of the object and the surrounding terrain; and third, incident angle (ϕ) is an unknown unless both the depression angle (β) and terrain slope (α) are known.

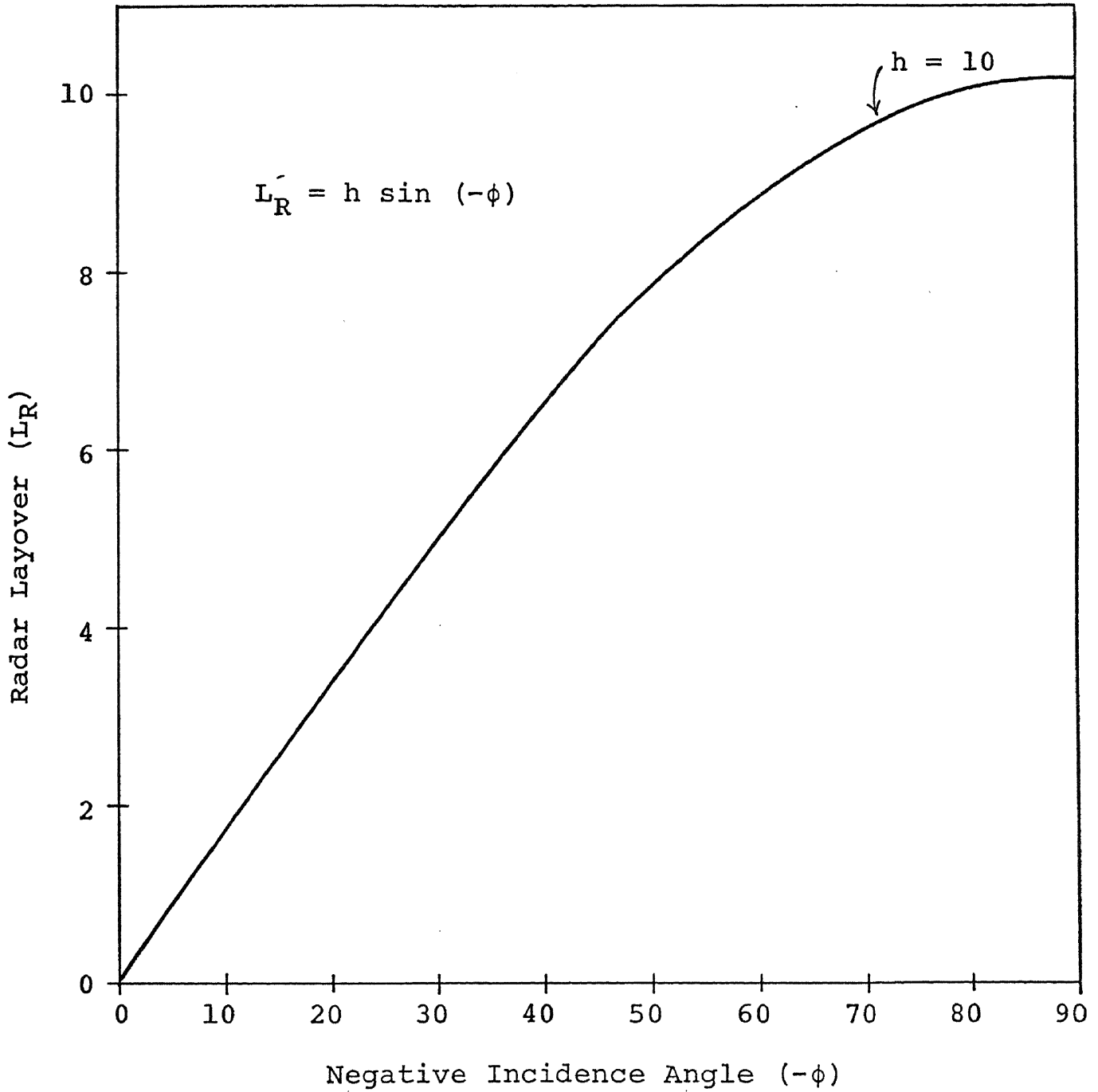


Figure 2.15 Relationship of Radar Layover (L_R) to Negative Incidence Angle ($-\phi$) at a Constant Object Height (h).

2.3.2.2 Slope Determination From Radar Layover

Since radar layover, like radar shadowing, is a function of depression angle (β) and terrain slope (α), the existence or non-existence of radar layover at a given depression angle provides terrain slope information. The use, limitations, and output from employing radar layover are the same as those involved in employing the radar shadow method to be discussed later.

The areal occurrence of radar layover is minute when compared to the areal occurrence of radar shadows, and therefore, the prime importance of utilizing radar layover as a discriminant of terrain slope is in conjunction with and as a supplement to the radar shadow method.

2.4 Radar Power Return

2.4.1 Slope Determination From Radar Power Return

A theoretical method for measuring terrain slope using the amount of radar backscatter from the slope has been derived by Cosgriff, Peake, and Taylor (1960). Radar signals are normally returned from the terrain to the receiver by a scattering process (reradiation) with the intensity of radar return from the terrain (signal strength) determining the relative degree of brightness on the radar imagery. The fundamental parameters that affect radar return are given by Taylor (1959) as being (1) surface roughness, (2) incident angle, (3) polarization, (4) frequency, and (5) complex dielectric constant. Since incident angle (ϕ) is a function of depression angle (β) and terrain slope (α) (Figure 2.13 and Equation 2.36), it can be seen that radar return is, at least partially, related to terrain slope. Although the influence of terrain slope may be modest when other parameters, such as surface roughness, vary greatly, it plays a predominant role in radar return from rolling topography where the type and amount of vegetation cover is constant.

This slope determining method by Cosgriff, Peake, and Taylor (1960) represents a simplification of the radar equation given in Equation 2.22:

$$P_r = \frac{\sigma G^2 P_o \lambda^2 |F(\beta, \gamma)|^4}{4(\pi)^3 S_R^4} \quad (2.22)$$

where

- P_r = average received pulse power
- σ = radar cross section
- G = maximum antenna gain
- P_o = transmitted power
- λ = wavelength
- $f(\beta, \alpha)$ = normalized one-way antenna voltage pattern
- β = depression angle
- γ = azimuth beamwidth
- S_R = slant range distance to the illuminated sector

By holding all of the parameters constant, except incident angle and terms that can be expressed as a function of incident angle, the equation can be reduced to

$$P_r \simeq C \left(1 + \frac{\sin 2\alpha}{\sin 2\beta} \right) \quad (2.23)$$

where C is some constant determined by the rest of the radar equation. The constant (C) can be eliminated if P_r is measured twice, from opposing directions, but at the same depression angle (Figure 2.16). The two measurements of P_r , designated P_r' and P_r'' , can be expressed as the power ratio (r) given by the following equation:

$$r = \frac{P_r'}{P_r''} \quad (2.24)$$

The terrain slope (α) is then defined by Cosgriff, Peake, and Taylor (1960) as

$$\sin 2\alpha = \sin 2\beta \frac{(1 - r)}{(1 + r)} \quad (2.25)$$

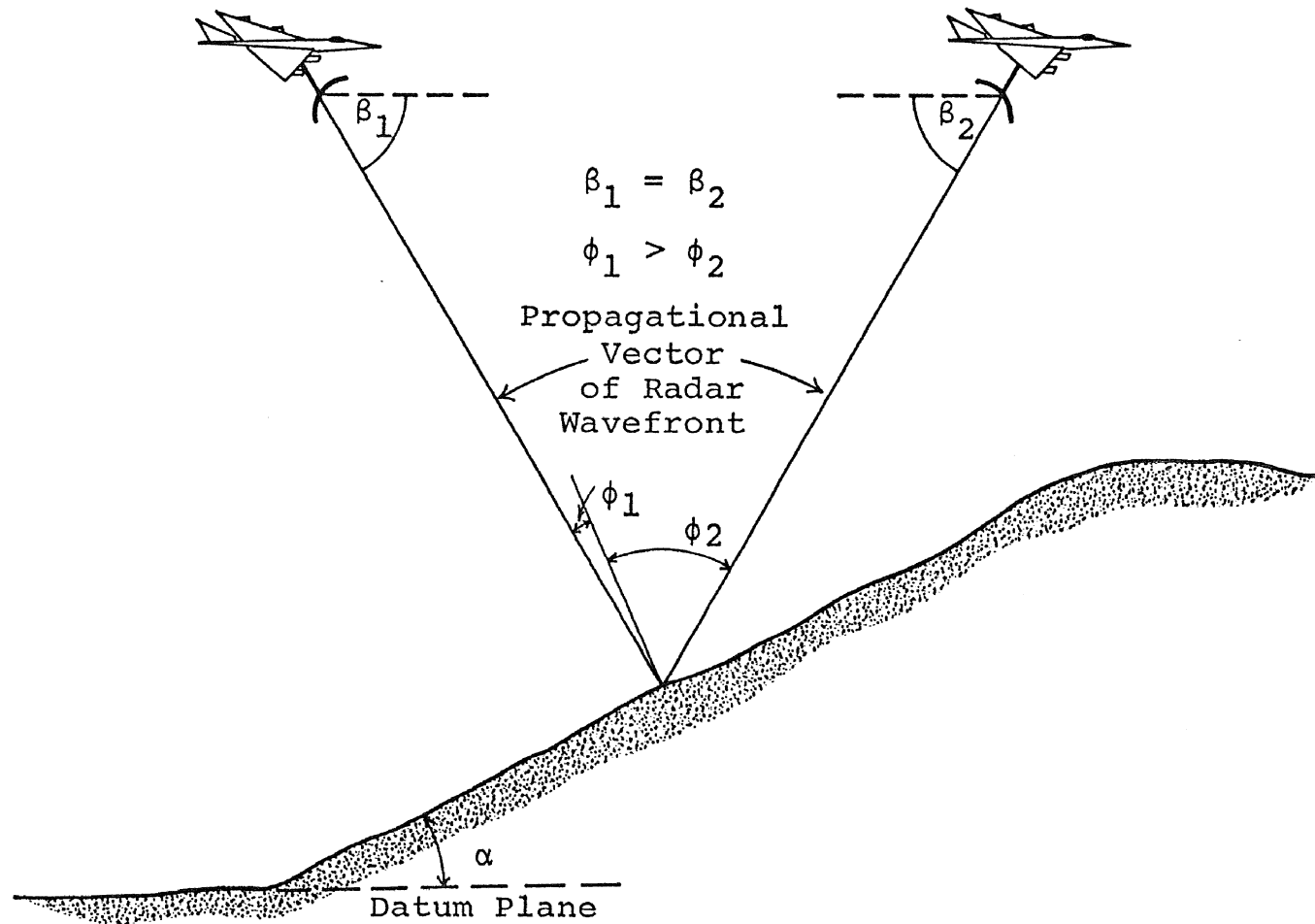


Figure 2.16 Imaging Conditions Necessary for Determining Terrain Slope (α) from Power Return (P_r).

For this procedure to be reliable, several conditions are necessary, and they are as follows (Cosgriff, Peake, and Taylor, 1960):

- (1) rolling terrain, i.e., large scale or contour roughness height, is greater than $C\tau/2$ (one half the pulse length),
- (2) small scale roughness is such that radar return (σ) is independent of depression angle β , i.e., surface roughness $>1/2$ wavelength (λ),
- (3) terrain slope (α) is small enough to exclude radar shadowing.¹

The method presented by Cosgriff, Peake, and Taylor has two limitations when radar imagery is used to determine P_r . The first, an areal limitation, is an outgrowth of the need to have two measurements of P_r in the opposite direction but at the same depression angle. Very little of the radar imagery presently available meets such a requirement. The second is an accuracy limitation, since it is necessary to: (1) make P_r measurements in terms of image gray-scale values measured on a densitometer; and (2) assume that the relationship between gray-scale value and P_r is linear. The use of radar scatterometry data² would eliminate these two restrictions inherent in radar imagery.

Another possible means of relating terrain slope (α) to power return (P_r) but utilizing only one measurement of P_r can be derived from Equation 2.23. By using P_r measurements from a constant depression angle (β), the value of P_r becomes a direct function of terrain slope, i.e., $P_r = f(\alpha)$. Since P_r as recorded on radar imagery and as measured by densitometric methods is functionally directly related to the transmissivity (T) of the radar image, $T = f(P_r)$ it follows that T is a function of terrain slope (α), $T = f(\alpha)$. Although the functional relationship between T and α is correct, the mathematical relationship is not at the present time known and its calculation is not within the scope of this study.³

¹Other conditions are given by Cosgriff, Peake, and Taylor (1960), however they are primarily related to system operation.

²Measurement data from a radar system used to determine radar scattering coefficients (normalized radar cross-section).

³The correlation of T to α as a first order polynomial relationship and as a first order approximation is given in Chapter 4.

2.5 Radar Shadow

The parameters that determine whether or not a terrain feature will produce radar shadow are depression angle (β) and the terrain slope of the slope facing away from the radar beam (α_b). The relationship between β and α_b is such that three cases are possible. They are: (1) the backslope is fully illuminated and no shadow results; (2) the backslope is partially illuminated, producing a condition analogous to the twilight zone, commonly referred to as grazing; and (3) the backslope is obscured (protected) from the impinging beam causing a no-return area of radar shadow (Figure 2.17). More definitely, the conditions for the three cases can be expressed as a function of β and α_b (Table 2.2). When the backslope is illuminated (no shadow), the angle of the backslope is less than the depression angle ($\alpha_b < \beta$); whereas, when grazing occurs, the two angles are equal ($\alpha_b = \beta$). Radar shadow, on the other hand, is exhibited when the terrain slope is greater than depression angle ($\alpha_b > \beta$); and it increases in both a probabilistic frequency occurrence and length as β decreases (Figure 2.17). As would be expected, radar shadowing is more intensive in the far range, that is, at the lower depression angles.

The condition necessary for radar shadowing as defined in Table 2.2 is valid only when the strike of the crestline is perpendicular to the propagational vector of the radar wavefront or parallel to the flight line (Figure 2.18). This arises because as the angle described between the flight line and the strike of the crestline (Θ) increases, the angle at which α_b will shadow at a given depression angle also increases. The

TABLE 2.2
RELATIONSHIP OF TERRAIN BACKSLOPE (α_b)
WITH DEPRESSION ANGLE (β) FOR THE OCCURRENCE OF RADAR SHADOWS

Case	Condition
No Shadow	$\alpha_b < \beta$
Grazing	$\alpha_b = \beta$
Shadow	$\alpha_b > \beta$

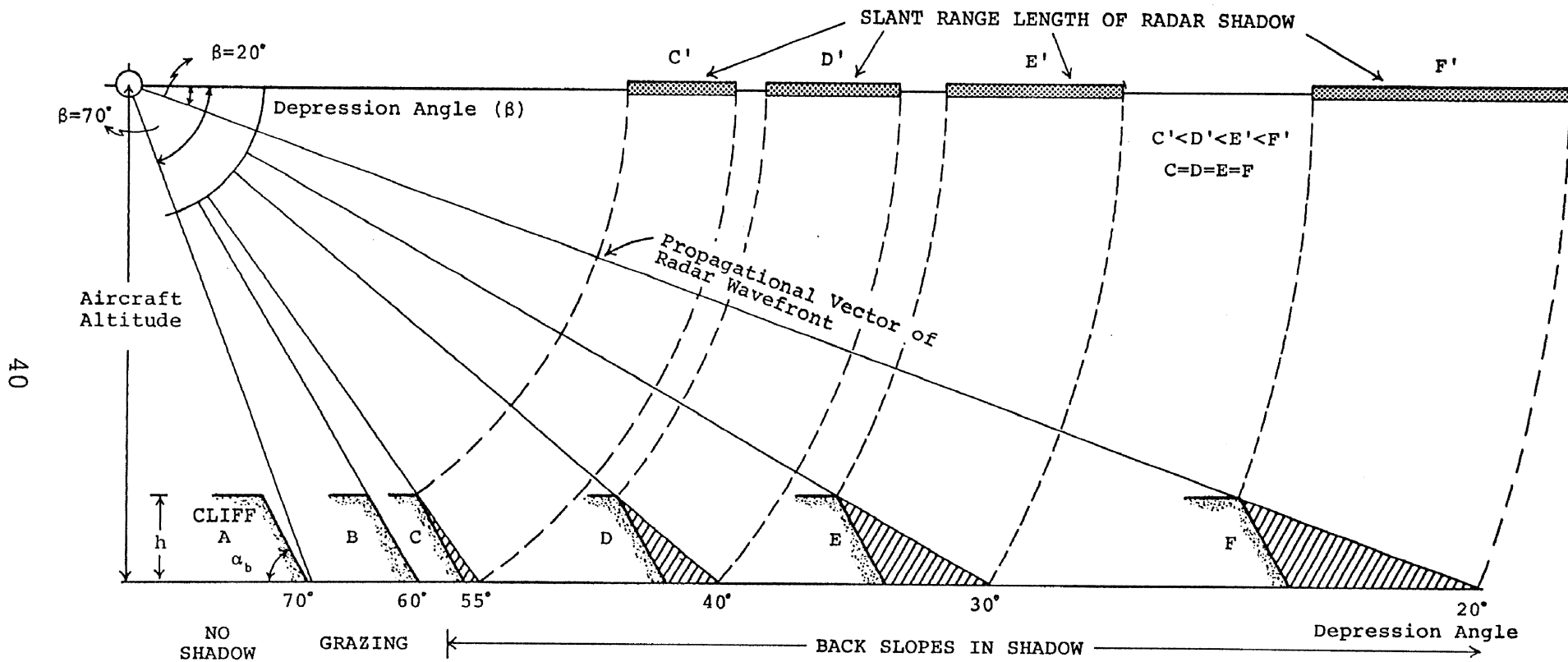


Figure 2.17 Relationship of Radar Shadow (Slant Range Length) with Depression Angle (β)

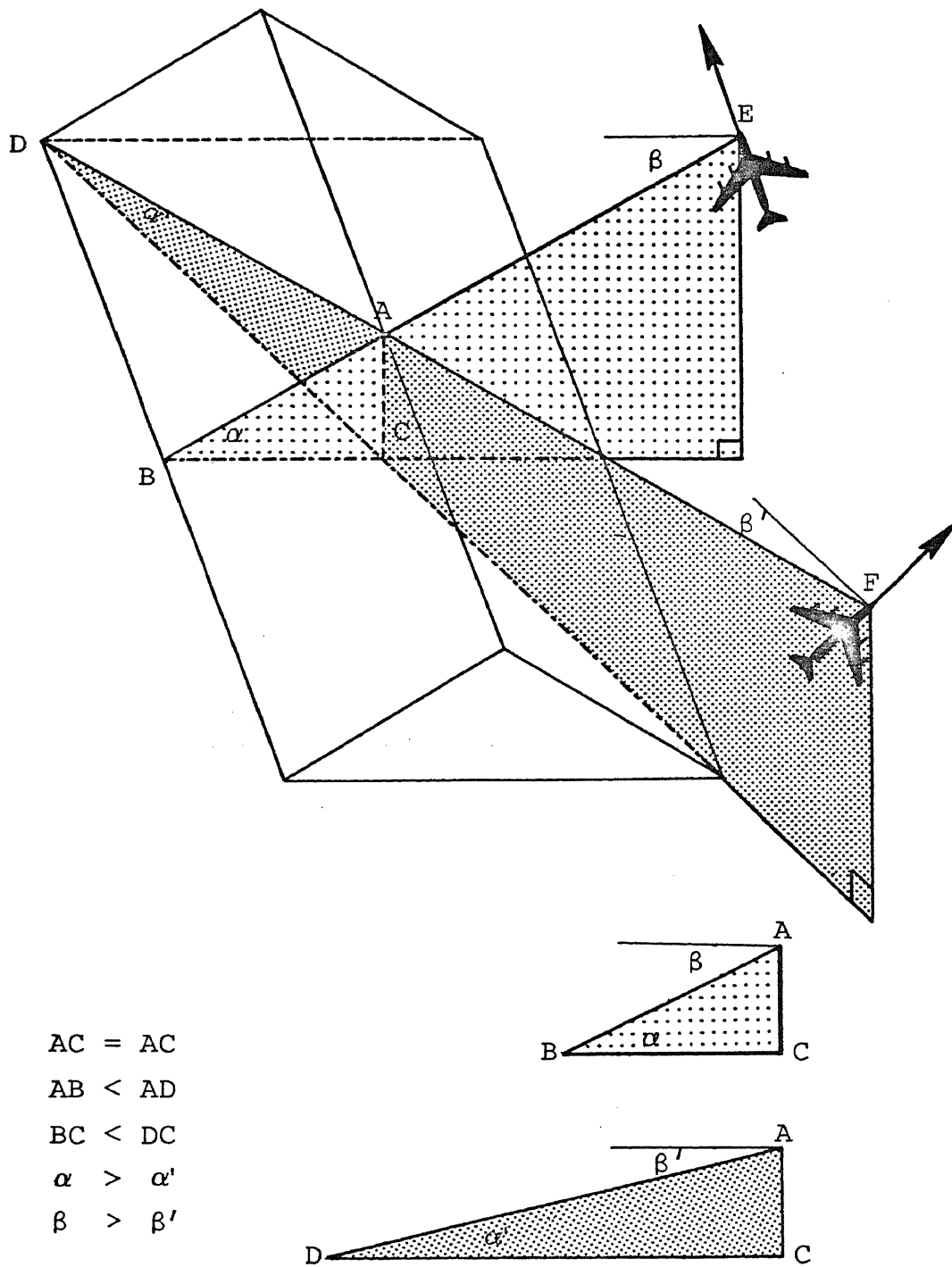


Figure 2.18 Effect of viewing angle on the terrain slope (α). Note as the viewing angle changes from perpendicular the terrain slope becomes smaller. This relationship is analogous to true and apparent dip.

effect of Θ on the angle at which α_b will shadow at a given (β) is given in Figure 2.19. As the figure illustrates, if a terrain backslope has a $\beta = 40^\circ$ and a $\Theta = 40^\circ$, then the backslope will not shadow until $\alpha_b > 47.5^\circ$. The absolute amount of error and the percentage of error related to selected values for Θ and β are given in Figures 2.20 and 2.21 respectively. As illustrated in Figures 2.20 and 2.21, where $\Theta < 80^\circ$ the absolute error encountered, regardless of the value for β , is less than 5° ; whereas the percentage of error is less than 15 per cent. Where $\Theta \geq 50^\circ$, the amount of absolute error, especially where β is between 15 and 45° , skyrockets. The graph of percent error (Figure 2.21) illustrates that percent error is more a function of β than Θ , whereas the absolute error (Figure 2.20) is the reverse, i.e., more affected by a change in Θ than β .

Once the conditions for the occurrence of radar shadow are satisfied, the length of the radar shadow in slant range (S_s) is directly related to the height of the terrain feature above a datum plane (h) and the total slant range distance from the aircraft to the far tip of the radar shadow (S_R) and inversely related to aircraft altitude (H) (Figure 2.22). This relationship is given in Equation 2.26.

$$S_s = \frac{hS_R}{H} \quad (2.26)$$

Expressed in terms of β , Equation 2.26 becomes

$$S_s = \frac{h}{\sin\beta} \quad (2.27)$$

or

$$S_s = h \csc \beta \quad (2.28)$$

Using Equation 2.27, Figures 2.23 and 2.24 were generated to illustrate how S_s varied when one parameter was varied and the other held constant. Figure 2.23 makes it clear that the effect of h on S_s is linear; whereas Figure 2.24 illustrates the geometric variation in S_s

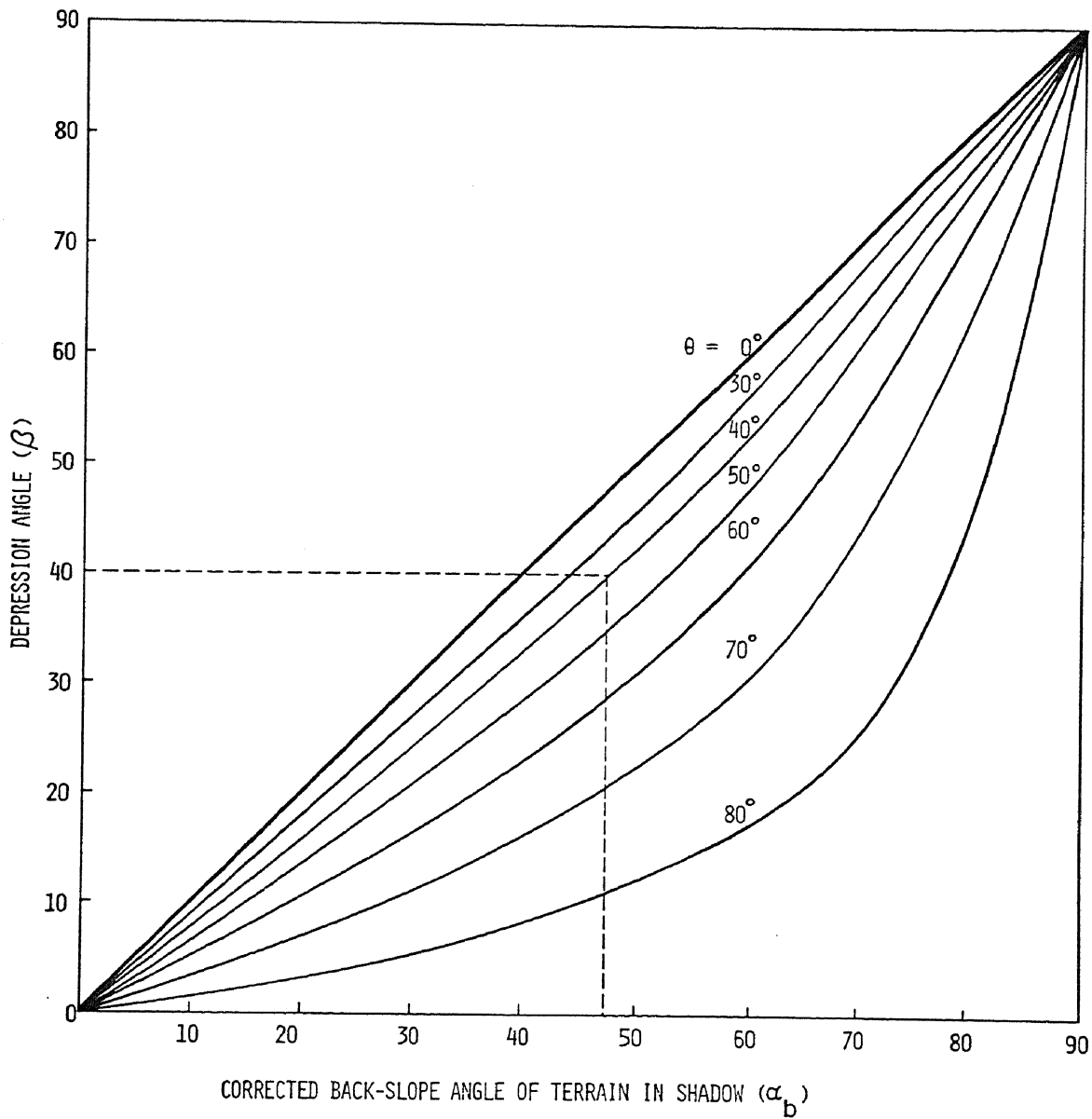


Figure 2.19 Relationship of Θ , the angle described by the flight direction and strike of the crestline, with α_b , the true back-slope angle of terrain in shadow. This is also a nomogram for correcting the apparent back slope angle to true back slope angle. For example, if a slope at a depression angle (β) and the angle between the flight path and strike of the crestline is 40° then the true back slope must be greater than 47.5° .

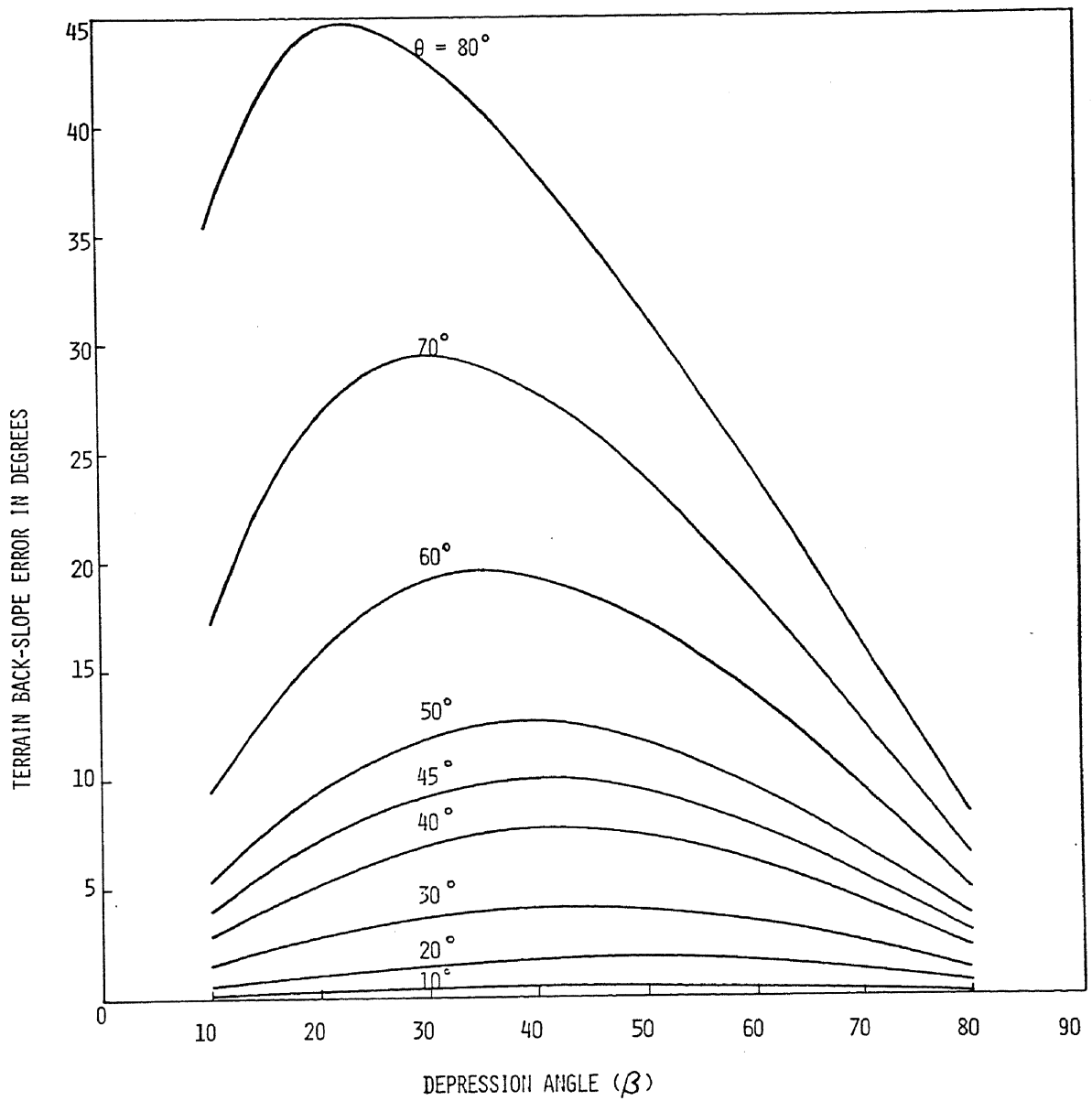


Figure 2.20 Absolute error in terrain backslope (α_b) as a function of depression angle (β) and the angle described by the flightline and the strike of the crestline (θ)

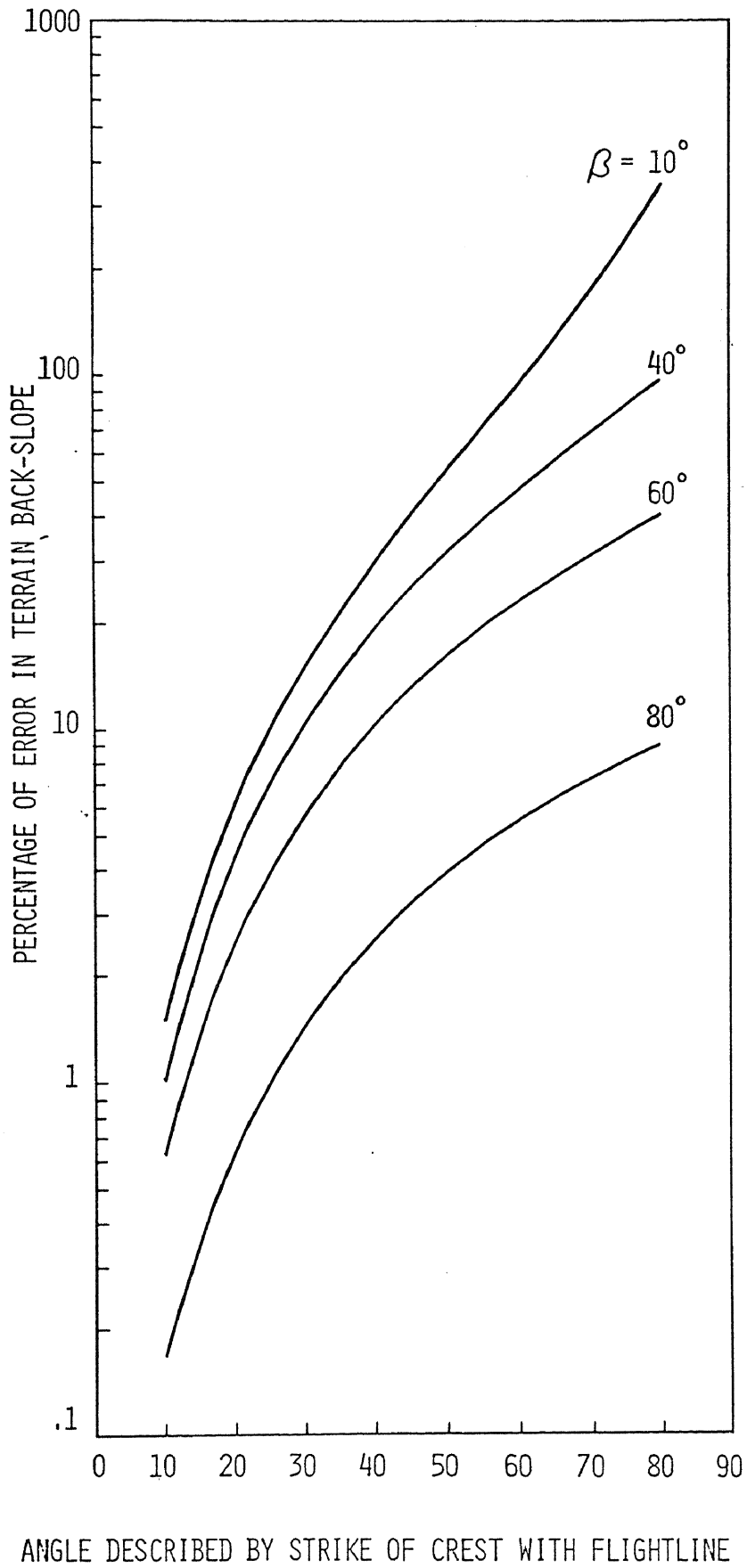


Figure 2.21 Percentage of error in terrain back-slope (α_b) as a function of the angle described by the flightline and the strike of the crestline (θ) and depression angle (β).

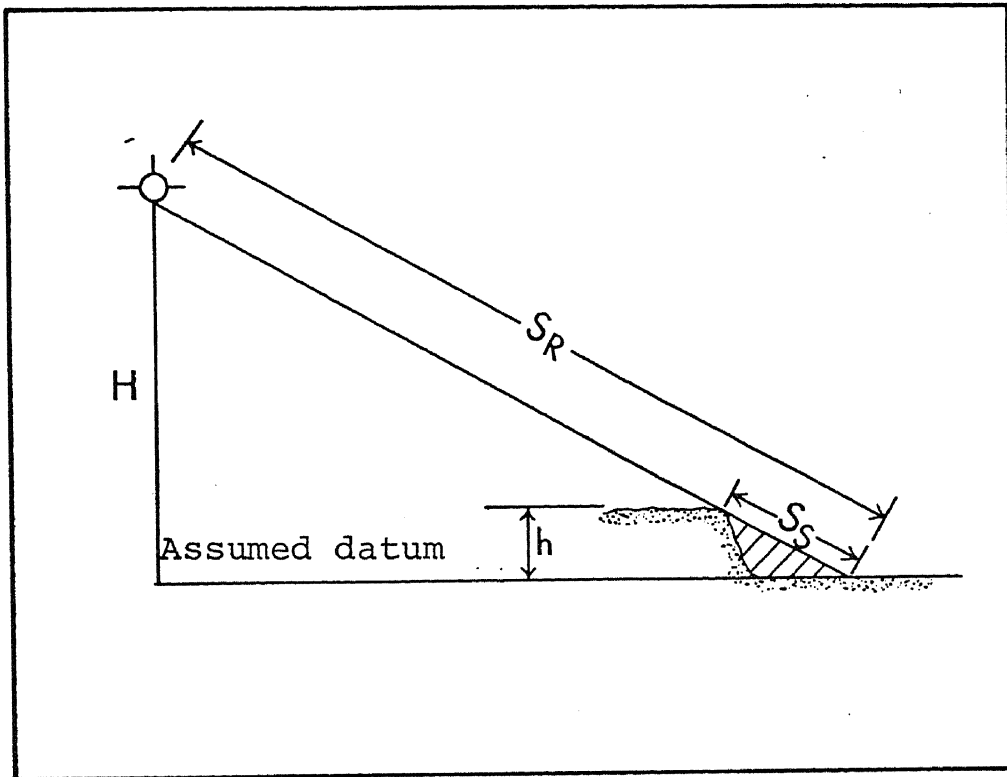


Figure 2.22 Simplified Radar Shadow Geometry.
(From McAnerney, 1966)

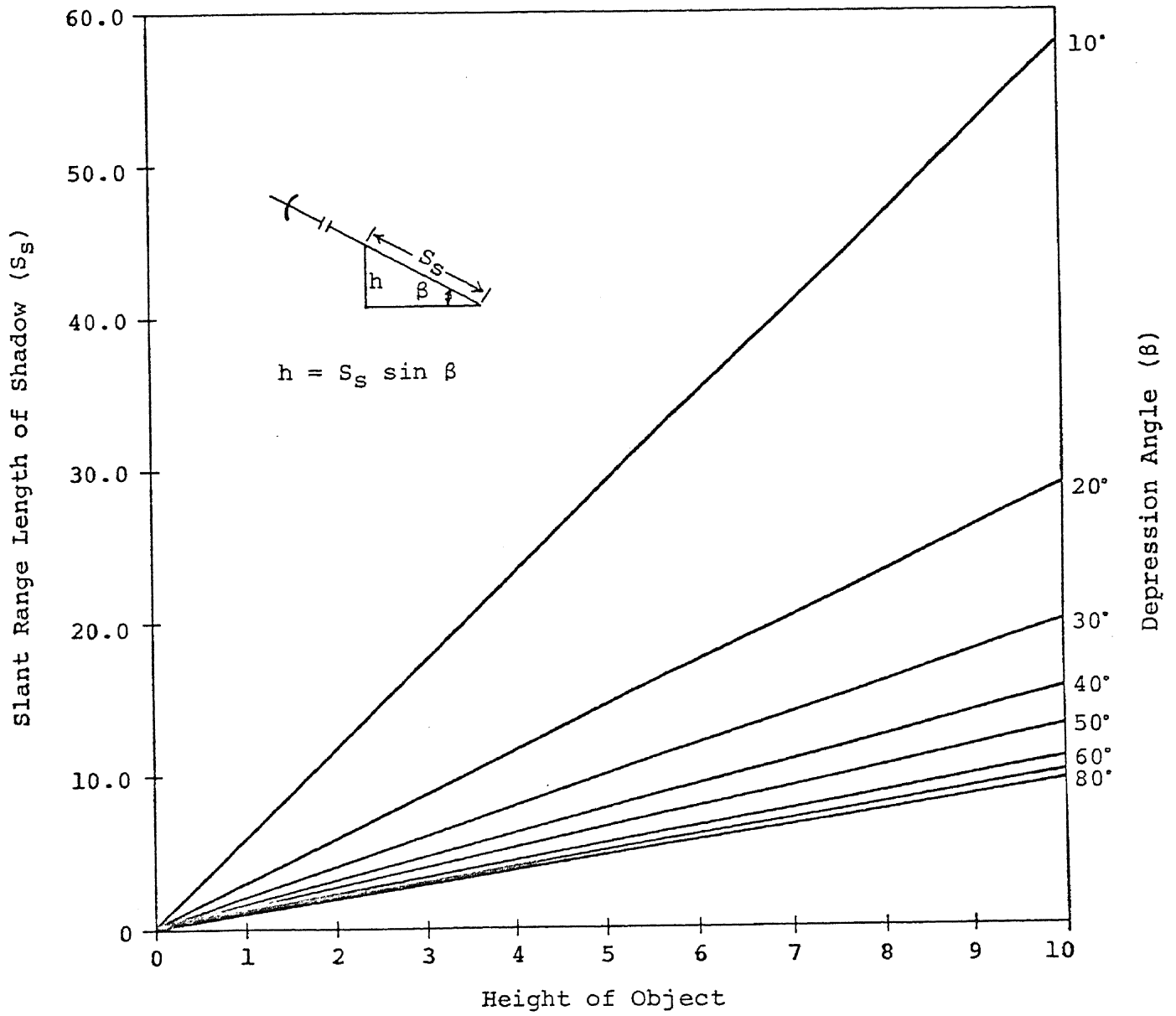


Figure 2.23 Relationship of S_s to h at a constant β

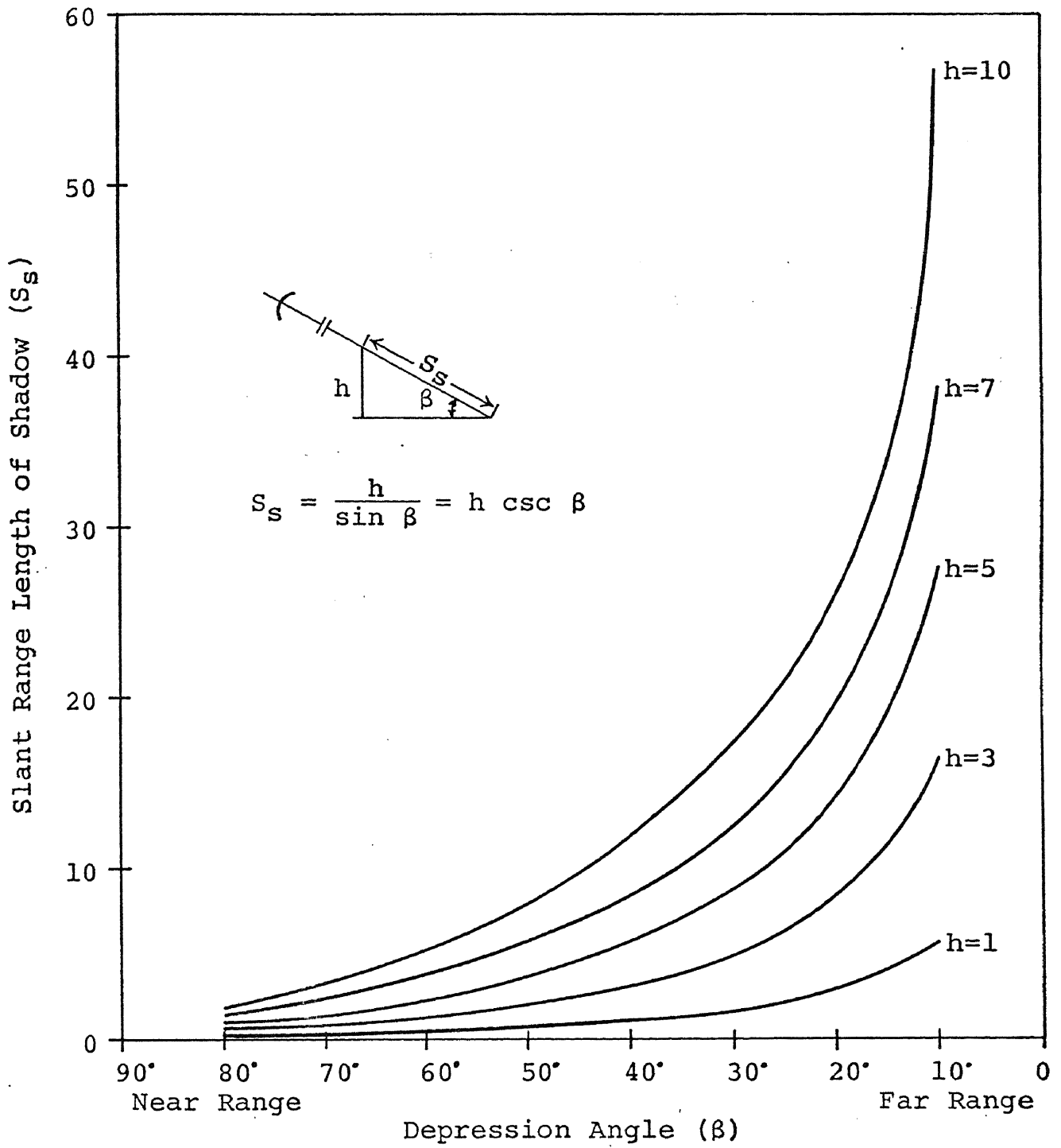


Figure 2.24 Relationship of S_s to β at constant h .

when β is less than 40° or 50° . This is an important consideration when analyzing the order of accuracy and the optimum range position for making the most accurate elevation measurements.

Figure 2.24 suggests that the accuracy of elevation determination theoretically would be better in the far range where $\beta < 30^\circ$. The reason for this is that the percent of error normally encountered in taking measurements decreases with increasing object size, or in this case, shadow length. The concept of increasing the accuracy of terrain elevation measurements is also substantiated in Figure 2.25, where, because of compression in the near range and expansion in the far range, the other variable (β) in Equation 2.27 can be more accurately measured at low depression angles. For example, from Figure 2.25, the accuracy of measuring the depression angle (β) between 20° and 30° is twice the accuracy encountered between 30° and 40° and over four times that between 70° and 80° .

The geometry and mathematical relationships involved in explaining the occurrence of radar shadowing is also applicable to solar shadowing since sun angle is defined the same as aspect angle (ψ) (Figure 2.3) and equal to depression angle (β). Two major limitations in using solar shadowing on orbital photography are: (1) solar shadowing is restricted to only two directions and is therefore of little value in landform regions strongly exhibiting an east-west grain; and (2) since the sun angle on a given photograph is essentially constant to duplicate the number of data points used to construct the cumulative frequency curves from radar shadowing would necessitate eight photographic passes either in the morning or the afternoon.

2.5.1 Types of Elevated Terrain

Although terrain features are nearly always complex in nature, simplified models used with the proper constraints can serve as a useful tool for understanding the relationship of imaging radar systems with terrain types and the restrictions terrain type impose on methods of elevation determinations. With imaging radar, the type of terrain feature recorded on imagery is determined by the relative time it takes a radar

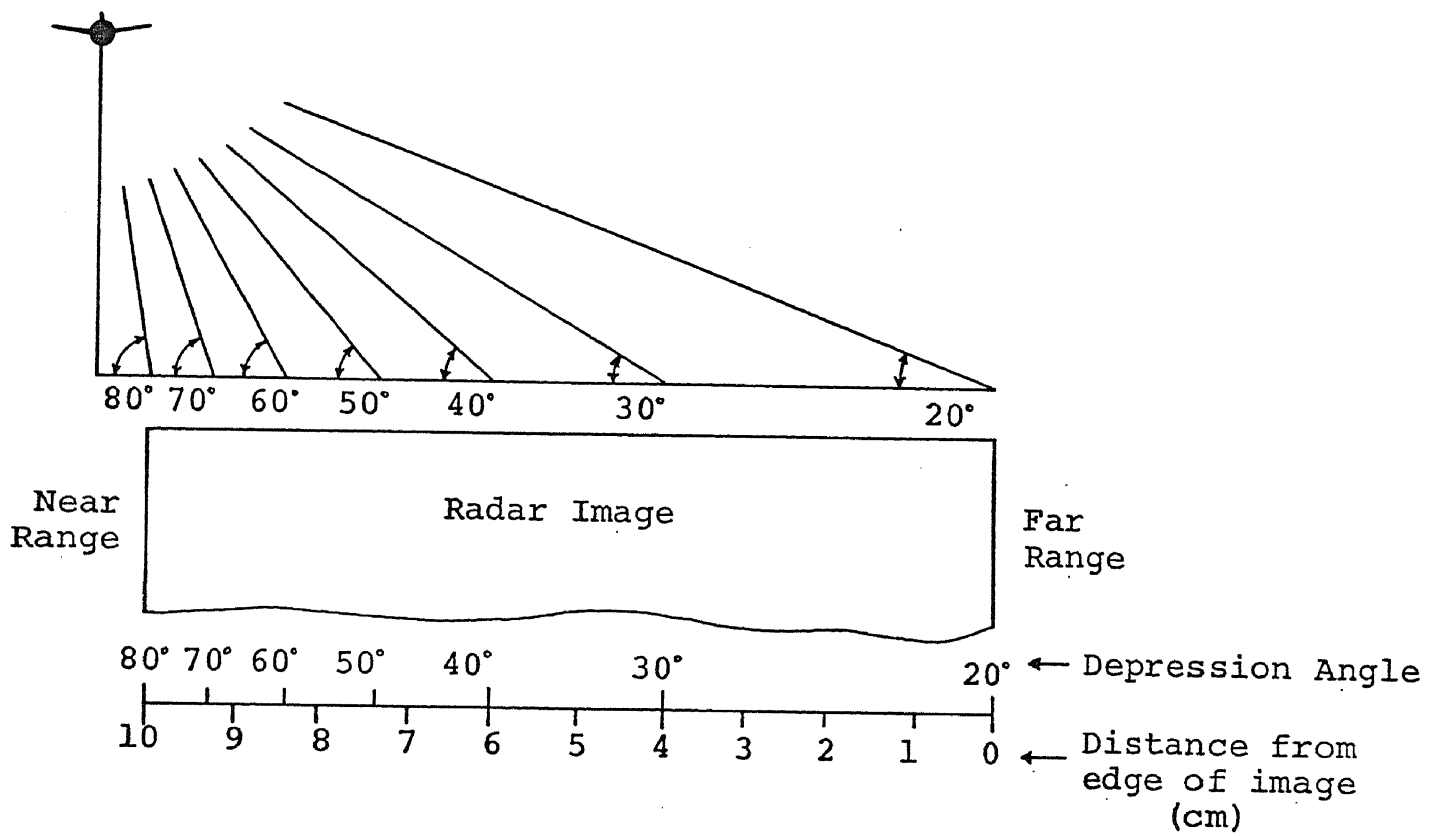


Figure 2.25 Relationship of the distance on the imagery between equal segments of depression angles with position in the range. (After McCoy, 1967)

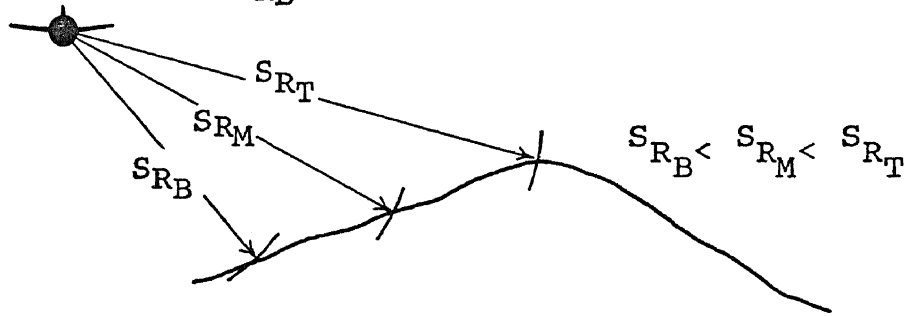
signal to travel from the radar transmitter in the aircraft to the top, middle, and base of the feature, and back to the radar receiver in the aircraft. Since the speed of the transmitted and received radar signal is a constant (the speed of light), the distance in slant range can replace time, and the type of terrain feature becomes a function of slant range distance to the top, middle, and base of the feature (Figure 2.26).

Type I is the normal elevated terrain feature in which the slant range distance (S_R) increases progressively from the bottom to the top of the feature, i.e., $S_{R_B} < S_{R_M} < S_{R_T}$ (Figure 2.26, Type I). Although the slope is foreshortened, the facets of the slope are displayed as a direct function of their elevation, the lowest point being first and the highest point being last. Type I is designated the "normal" since it is closely akin to the visual perception the observer has of the terrain feature.

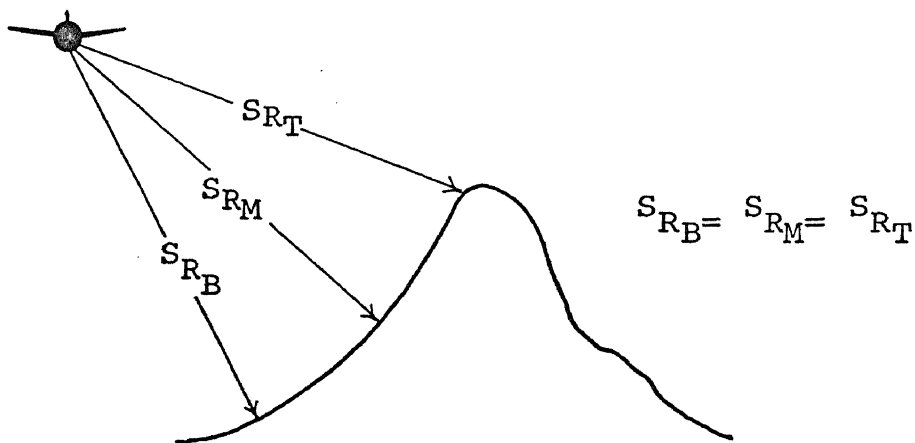
Type II is designated the "degenerate" elevated terrain feature (Levine, 1960, p. 146). The criteria for this type is that the slope facing the aircraft is concave upward and describes an arc of a circle whose center is located at the aircraft (Figure 2.26, Type II). When this condition is met, the slant range distances from base to top of the feature are equal, i.e., $S_{R_B} = S_{R_M} = S_{R_T}$ and the complete terrain slope is imaged as a point.¹ Type II is also an extreme case of multiple mapping, the radar returns from each slope facet along the entire length of the arc being recorded simultaneously and therefore being completely integrated with each other. Fortunately, the conditions for imaging an entire terrain slope of any magnitude as a point are not generally met. However, the imaging of individual slope facets as a single point is a more common occurrence.

¹The arc of the circle described by the propagating radar beam is constantly changing, therefore the position of the slope in respect to slant range is critical for imaging the slope as a point.

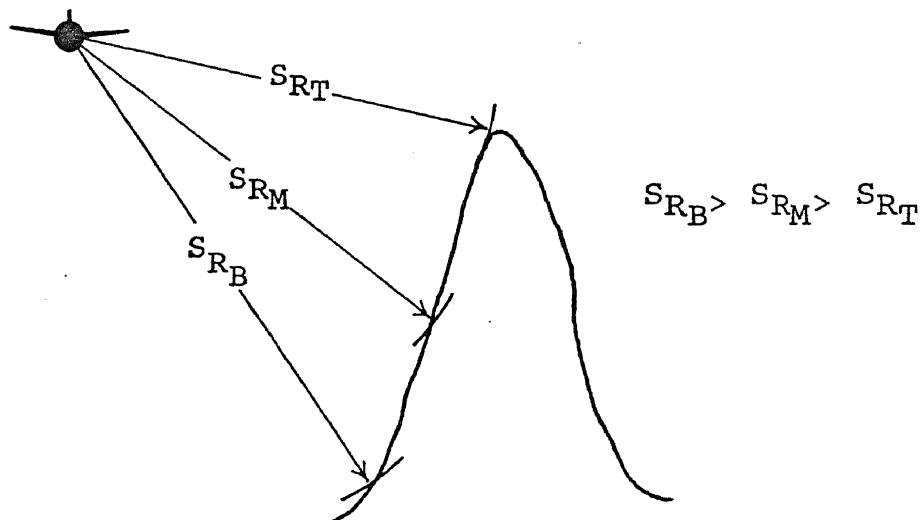
S_{RT} = Slant range distance to top
 S_{RM} = Slant range distance to middle
 S_{RB} = Slant range distance to bottom



TYPE I. Foreshortened slope



TYPE II. Slope imaged as point



TYPE III. Slope presented as inverted image

Figure 2.26 Simple Types of Elevated Terrain Features.
(Modified from Barr, 1968)

Type III of the simple terrain models is often referred to as the "flagpole" case (Levine, 1960, p. 146) and applies to any terrain feature where the slant range distance from the aircraft is greater at the base (S_{R_B}) than it is at the middle (S_{R_M}) or top (S_{R_T}) of the feature, i.e., $S_{R_B} > S_{R_M} > S_{R_T}$ (Figure 2.26, Type III). When this condition prevails, the top of the terrain feature is imaged and recorded first, followed by the middle and finally the base. In simple terms, the feature has been inverted, a phenomenon commonly known as radar layover and previously discussed in greater detail. It is sufficient to recall from the section on radar layover the criteria for its occurrence: steep slopes and/or high depression angle. As with Type II, the conditions for this phenomenon are not met in natural terrain except in extreme cases; for example, when an active cut bank of a river meander faces the imaging system, or locally when a slope facet faces the imaging system.

Although three simple models sufficiently describe the variations possible when a radar beam impinges on a portion of the terrain surface, a terrain feature can have sufficiently different slope facets so that any combination of two or three types can occur along a single terrain slope. The combination of slope types varies with the position of the terrain feature in the slant range.

The use of radar shadow to measure terrain elevation is restricted to the foreshortened slope of Type I imaged in the normal sequence and the "degenerated" slope of Type II that is imaged as a point. Elevation determinations from equations utilizing radar shadow lengths as the major parameter are based on the assumption that $S_{R_B} \leq S_{R_T}$. Regardless of the complexity of the terrain feature, if $S_{R_B} \leq S_{R_T}$, then the terrain slope has fulfilled one of the necessary assumptions required for the accurate determination of elevation with radar shadow. The other assumptions are that (1) the tip of the radar shadow falls on a horizontal surface that is on the same datum as the altitude to which the radar imaging system, actually the aircraft, is referenced, and (2) the elevation is also referenced to the same datum. McAnerney (1966) justifies these

assumptions on the basis that the aircraft altitude is usually very great compared with the magnitude of measured relief, and therefore any error from this assumption is generally within the limits of accuracy of the scaling of distance.

The elevation of Type III can also be found by utilizing the length of radar shadow plus the amount of radar layover, or as previously mentioned, by the amount of radar layover alone.

2.5.2 Relative Relief Determined from Radar Shadows

Perhaps the most practical method for measuring elevation or local relief is by means of radar shadow. The advantages of using radar shadow are the following:

- (1) radar shadow is usually easy to define and measure,
- (2) the method involves an easily solved mathematical relationship, and
- (3) only one imaging pass is required if the object produces shadow.

Assumptions that will be discussed later limit the use of this method to areas of high, natural features capable of producing significant radar shadows and areas where the shadows are cast on relatively level ground. Also, the order of accuracy is not generally good enough for precise work.

Basically, all of the equations for calculating relative relief from radar shadow are based on the principle that corresponding sides of similar triangles are proportional. Therefore, by taking two corresponding sides from triangles ABC and A'B'C' in Figure 2.27, one of the sides can be determined if the other three sides or an equivalent are known, provided the basic assumptions listed previously hold.

The simplest equality taken from Figure 2.27 is given in the following equation:

$$\frac{h}{H} = \frac{S_s}{S_R} \quad (2.29)$$

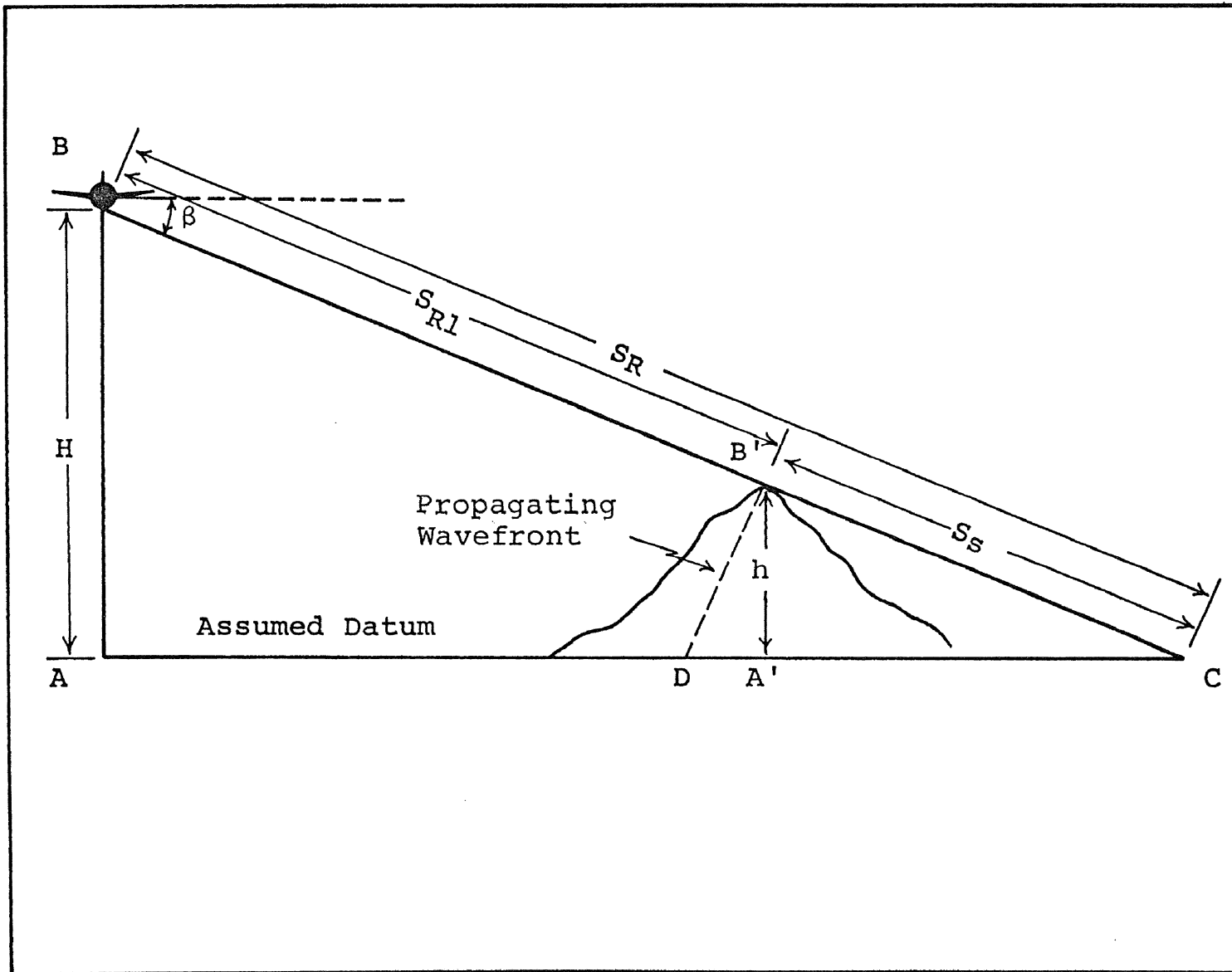


Figure 2.27 Radar Shadow Geometry. (Modified from Goodyear Aerospace Corp., 1966)

where

h = height of the feature

H = altitude of the aircraft

S_s = slant range length of the shadow

S_R = slant range distance from the aircraft to the end of the shadow.

Solving for h , the equation becomes

$$h = \frac{H(S_s)}{S_R} \quad (2.30)$$

and since

$$\frac{H}{S_R} = \sin \beta \quad (2.31)$$

where β is the depression angle measured at the edge of the shadow closest to the near range or nadir, it follows that h can be expressed in terms of β :

$$h = (S_s) \sin \beta \quad (2.32)$$

McAnerney (1966) devised a method for calculating elevation utilizing the slant range distance from the aircraft to the top of the shadow producing feature (S_{R1}) in place of the shadow length (S_s) (Figure 2.27). The equation is as follows:

$$h = H \left(1 - \frac{S_{R1}}{S_R} \right) \quad (2.33)$$

McAnerney's method is a simplification of a method by Levine (1960, p. 147). Levine's equation does not make the assumption that the base of the terrain

feature has the same reference datum as the aircraft. Without this assumption, an extra unknown, the elevation of the reference plane above the datum plane upon which the shadow is cast (h_s) (Figure 2.28), is added to the equation which is given by Levine as

$$h = H - (H-h_s) \frac{S_{R1}}{S_R} \quad (2.34)$$

This equation is of little value unless the assumption that $h_s = 0$ is made and the equation reduced to Equation 2.33 since Equation 2.34 requires the solving of two unknowns from a single equation.¹

A method using radar shadow and radar layover for spot elevation is given by LaPrade and Leonardo (1969) as:

$$h = \sqrt{L_R(L_R + S_s)} \quad (2.35)$$

where h , L_R , and S_s are defined in Figure 2.14 as the height of the object, radar layover in the slant range, and slant range length of the radar shadow, respectively. This method of using layover in combination with shadow has the same disadvantages as the method using layover alone to determine elevation and is more complex than the equation utilizing radar layover (Equations 2.20 and 2.21).

2.5.3 Slope Determination From Radar Shadows

2.5.3.1 Individual Slopes

Utilizing the conditions necessary for radar shadowing, i.e., $\alpha_b > \beta$ in conjunction with Figure 2.19, a semi-quantitative value can be

¹This equation can be solved by simultaneous equations if overlapping radar imagery is available.

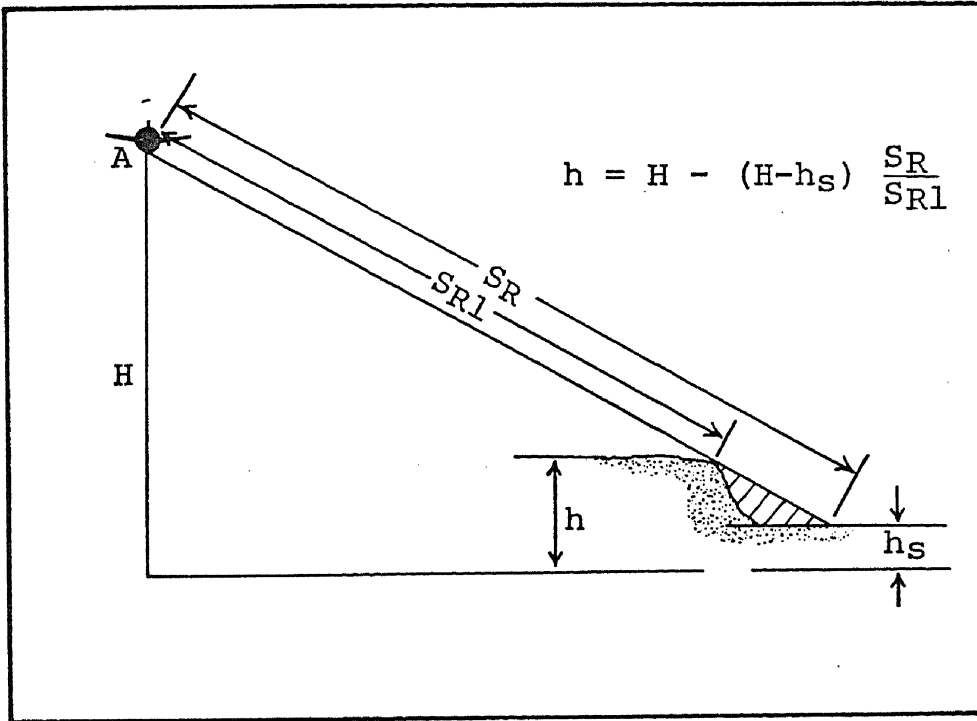



Figure 2.28 Radar Shadow Geometry for Levine's Method. (From McAnerney, 1966)

assigned to a given terrain slope on radar imagery. For example, if a terrain slope is located at a $\beta = 40^\circ$ and has a $\Theta = 40^\circ$ and exhibits radar shadowing, then the terrain slope (α_b) is greater than 47.5° . Therefore, Figure 2.19 an expression of $\alpha_b = f(\Theta)$, is also a nomogram that provides for rapid determination of the specific terrain slope angle (α_b), where α_b is greater than β if there is radar shadowing or less than β if there is no radar shadowing.

2.5.3.2 Regional Slope

Regional slope can be defined by sampling either as a single value such as the mean, median, or mode or as a range or distribution of values such as in a histogram or cumulative frequency curve. To date only the former type of regional slope information, i.e., a single value, has been abstracted from radar imagery. For example, McCoy (1967, p. 2) suggests that a population of 25 to 30 slope measurements determined from radar imagery using radar foreshortening — to be described later — is a sufficiently large sample set to provide an accurate expression of the mean slope value for a single region when compared to topographic map data. McCoy also alludes to another means of obtaining mean slope value for a given geomorphic region utilizing grazing, a characteristic of radar when the backslope angle of the terrain (α_b) is equal to the depression angle (β). By determining the depression angle where grazing occurs, the mean regional slope can be estimated provided that the landforms on both the near-range and far-range side of grazing, but within the region for which the mean slope value applies, are homogeneous.

The assumptions involved in using the grazing method when only one look-direction is available are that 1) the imaged terrain approaches a saw-tooth landform model, i.e., ; and 2) there is a random distribution of slope angles in the imaged area. As the number of look-directions increases, the importance of the assumptions is diminished since the bias of unidirectional sampling is progressively eliminated.

Several problems arise when the grazing method is employed, the most formidable of which are (1) the difficulty of delimiting areas of

grazing; and (2) the high probability that the area exhibiting grazing will be lost in radar shadow unless the angle of the terrain slopes above the point of grazing decreases so that shadowing does not occur, i.e., $\alpha_b \leq \beta$.

By utilizing the conditions for and the occurrence of radar shadows ($\alpha_b > \beta$) instead of grazing, some of the problems and limitations of the grazing method can be reduced. The difficulty of defining areas in grazing is eliminated by deciding whether the backslope along a crest-line does or does not produce radar shadowing. By changing to a yes-no decision, the decision-making is not only easier and more definitive but also increases both the utilization of radar-derived data across the complete range dimension of the imagery and the sampling area within the delimited landform region. The most natural manipulated data output from this method and the grazing method is a cumulative frequency curve of slope values of each defined region from which both a histogram of a slope value or the mean regional slope value can be derived.

The use of radar shadowing on a yes-no decision basis has several advantages over most methods used for determining regional slope values: (1) the increased speed of determining the regional slopes of large areas, (2) the discrimination of landform regions within large areas based on the plots of percent crestlines in shadow, (3) the ease with which the method lends itself to automatic methods of pattern recognition and measurement, and (4) the apparently high degree of accuracy, especially when one considers that the mean regional slope values and slope distribution curves are derived from sampling and are therefore only as good as the sampling techniques.

Since the assumptions involved in the shadow-frequency method are the same as those associated with the grazing method, the restrictions related to having a homogeneous area and a random distribution of slopes are relevant. It is up to the user of the method to satisfy the assumptions. This is accomplished by corroborative data of the area and a qualitative interpretation of the radar imagery that results in the (1) delineation of homogeneous landform regions, and (2) confirmation of random slope distribution.

For maximum data retrieval with the shadow frequency method, the landform region being studied should (1) extend across the entire range of the radar image, and (2) change from no shadowing in the near range to extensive shadowing in the far range. The first condition can be satisfied by pre-fixing the imaging specifications so the area in question is imaged from the near to the far range either completely on one imaging pass or in overlapping segments on multiple imaging passes. The second condition requires at least the existence of radar shadows in the far range; however, it is best met with the present imaging radar systems in areas with moderate to high slopes, i.e., $>20^\circ$. Since the approximate depression angle in the far range of most of the operational radar imaging systems is around 15° , no shadows will be formed in landform regions with terrain slopes less than 15° . This is a severe restriction when the large percentage of terrain slopes between the range of 0 and 15° is considered along with the critical nature that slope variation in this range has on land use, vehicular mobility, and other user requirements. The expansion of the far range all the way to 1° depression angle is a possible solution, especially with a synthetic aperture imaging radar system flown at a low altitude. Although such drastic modifications are not likely to take place, system modifications have lowered the far range depression angle several degrees ($\approx 5^\circ$).

The ubiquitous nature of radar shadowing plus the relatively straight forward relationships of radar shadowing to terrain slope and relative relief provides not only the geomorphologist but anyone engaged in terrain analysis with a potentially powerful tool for both functional and genetic landform analysis on both meso and macro scales.

2.6 Radar Foreshortening

Just as the slant range distance, measured as a function of time, determines the sequence in which targets are displayed, the period of time a slope is illuminated determines the length of the slope on radar imagery. This phenomenon, referred to as "radar foreshortening,"

results in the shortening of a terrain slope on radar imagery in all cases except when the incidence angle (ϕ) is equal to zero, at which time the terrain slope length (L) is equal to the slope length measured on the radar imagery (L_F), assuming that the scale factor between the imagery and the terrain (S_K) is taken into account (Figure 2.29).

The length of the terrain slope measured on slant radar imagery (L_F) is a function of incidence angle (ϕ) which in turn is a function of depression angle (β) and terrain slope (α), that is

$$L_F = f(\phi) = f(\beta, \alpha) \quad (2.36)$$

More accurately, L is mathematically defined in Equation 2.37 and illustrated in Figure 2.29.

$$L_F = L \sin \phi \quad (2.37)$$

Again the assumption is made that a scale factor (S_K) was applied to either L_F or L in order to express the slope length in terms of the radar imagery or the actual slope length on the ground. The relationship is simply defined as the following:

$$(k)L_F = L \quad (2.38)$$

The percent of radar foreshortening (F_P), also a function of ϕ , (Figure 2.29) is defined by Equation 2.41.

$$F_P = \left(\frac{L - L_F}{L} \right) \times 100 \quad (2.39)$$

$$F_P = \left(\frac{L - L \sin \phi}{L} \right) \times 100 \quad (2.40)$$

$$F_P = (1 - \sin \phi) \times 100 \quad (2.41)$$

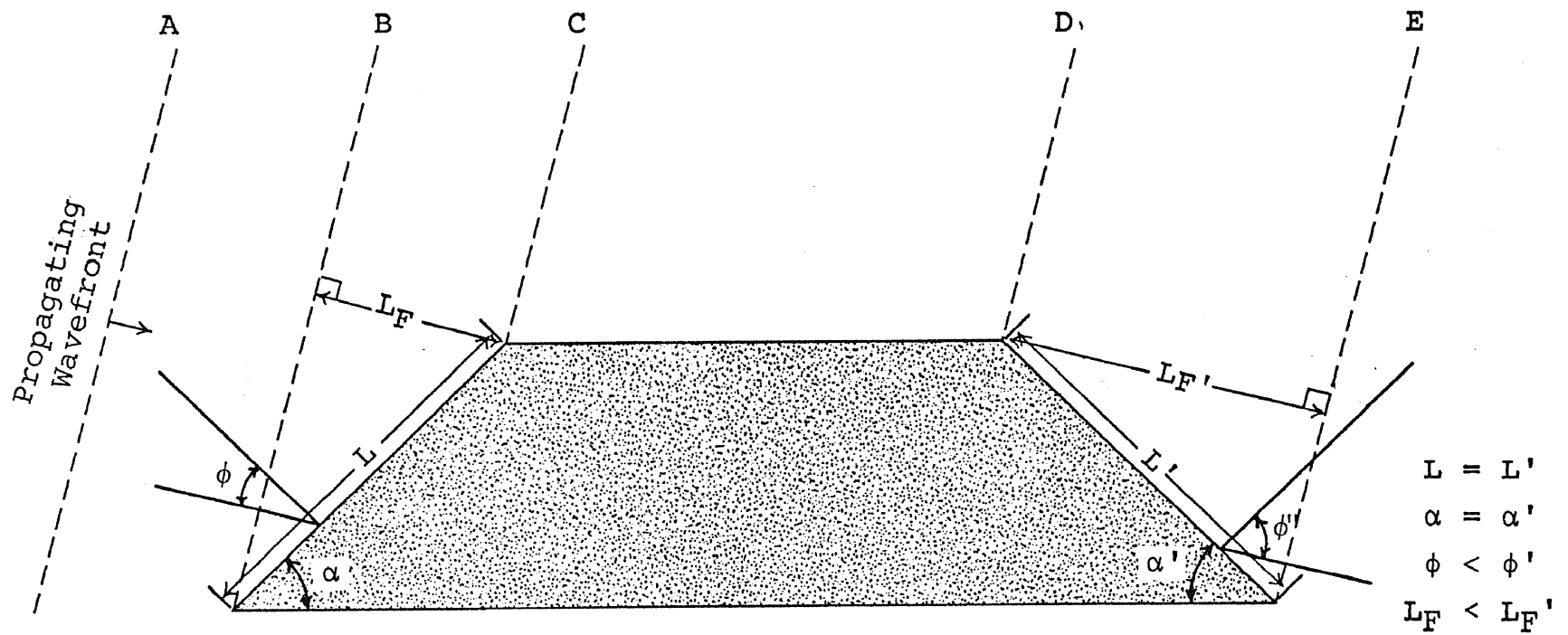


Figure 2.29 Relationship of Slope Foreshortening (L_f) with Incident angle (ϕ) on Slant Range Imagery.

This relationship is illustrated in Table 2.3.

TABLE 2.3
PERCENT RADAR FORESHORTENING (F_P) AS A
FUNCTION OF INCIDENT ANGLE (ϕ)

Incident Angle	Percent Radar Foreshortening
90	0.0
80	1.5
70	6.0
60	13.4
50	23.4
40	35.7
30	50.0
20	65.8
10	82.6
0	100.0

2.6.1 Slope Determination from Radar Foreshortening

A unique method for deriving terrain slope (α) from radar foreshortening was developed by Dalke and McCoy (1969). The Dalke-McCoy Method utilizes an inherent distortion in slant range imagery, radar foreshortening. As previously stated in Equations 2.36 and 2.37, the slant range length measurement of a slope facet (L_F) is a function of the depression angle (β) and the angle of the slope facet (α), $L = f(\beta, \alpha)$. In the case of level terrain, L_F is related to only the depression angle β , i.e., [$L = f(\beta)$ when terrain slope is zero (0)].

The Dalke-McCoy Method determines the angle of the slope facet (α) by using overlapping coverage of two radar images flown parallel to each other but not necessarily at the same look-direction. β and L are measured from each of the images for the same slope facet and the slope angle is a function of two depression angles (β and β') and two slant range measurements (L_F and L'_F) or

$$\alpha = f(\beta, \beta', L_F, L'_F) \tag{2.42}$$

Two conditions encountered in acquiring overlapping radar imagery are considered in this method:

- (1) flight lines are parallel but flight direction is opposite; therefore, the terrain is imaged in opposite directions (Figure 2.30)
- (2) flight lines are parallel and flight direction is the same; therefore, the terrain is imaged in the same direction (Figure 2.31).

In each case a separate equation is necessary for the calculation of terrain slope (α). For Case 1, where the data is collected from two images of opposite look-direction, the equation is

$$\alpha = \text{ARCTAN} \left[\frac{L_1 \cos \beta_2 - L_2 \cos \beta_1}{L_2 \sin \beta_1 + L_1 \sin \beta_2} \right] \quad (2.43)$$

Where the same look-direction is utilized for data collection, the equation becomes

$$\alpha = \text{ARCTAN} \left[\frac{L_1 \cos \beta_2 - L_2 \cos \beta_1}{L_2 \sin \beta_1 - L_1 \sin \beta_2} \right] \quad (2.44)$$

2.6.2 Relative Relief Determined from Radar Foreshortening

An obvious extension of the Dalke-McCoy Method for determining slope angle (α) is the calculation of relative relief (R_R). Once the terrain slope angle (α) is determined, the only other parameter needed to calculate relative relief (R_R) is the actual length of the slope facet on the ground (G_f), and this can be calculated from the slant range length measurement of the slope facet (L_f) which is already known.

$$\sin \alpha = \frac{R_R}{G_f} \quad (2.45)$$

$$R_R = G_f \sin \alpha \quad (2.46)$$

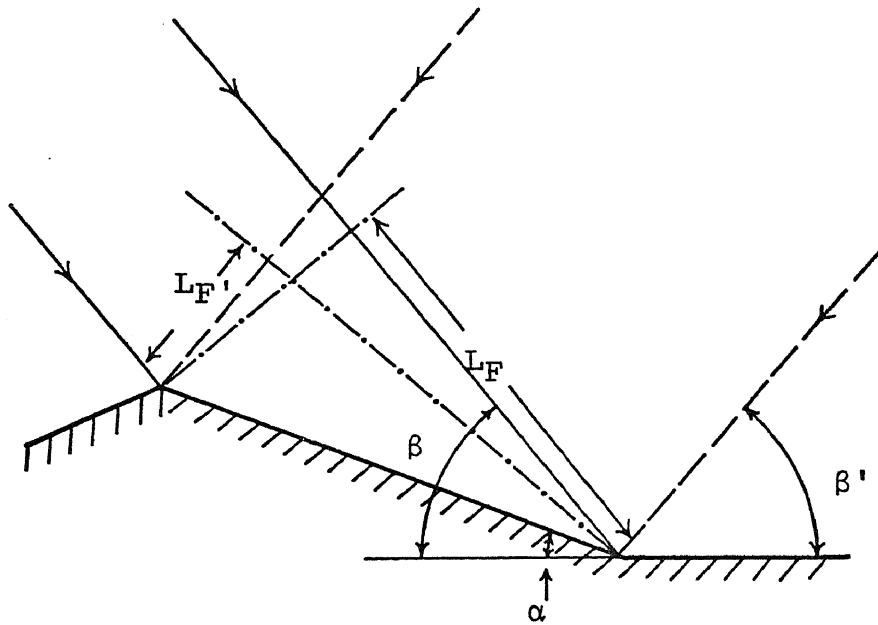


Figure 2.30 Radar Foreshortening Geometry when Using Two Images with the Same Look Direction. (From Dalke and McCoy, 1969)

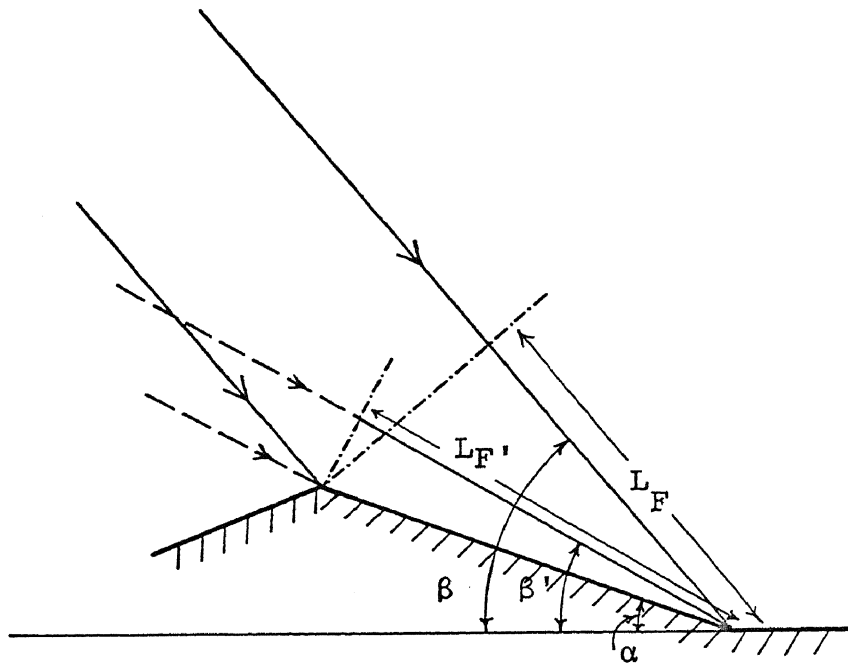


Figure 2.31 Radar Foreshortening Geometry when Using Two Look Directions. (From Dalke and McCoy, 1969)

Therefore, solving for R_R requires changing L_F to S_r and utilizing Equation 2.46. Changing L_F to S_r is a two step transformation, the order of which is not of great importance; however, since the imagery is a slant range presentation, the sequence presented is a little simpler than the reverse order.

Step (1). Correct the slope length measured on the image to the true slant range scale (S_r) on the ground, by determining the slant range scale factor between the imagery and the terrain (S_K) and then multiplying the scale factor by the slope length (L_F) measure on the image. S_K is found by solving the following equation and is visually presented in Figure 2.5.

$$S_K = \frac{H}{\sin\Psi_2} - \frac{H}{\sin\Psi_1} \cdot \frac{1}{X} \quad (2.47)$$

where

S_K = slant range scale/unit value

H = altitude of aircraft

Ψ_1 = aspect angle at which imaging starts

Ψ_2 = aspect angle at which imaging ends

X = measured width across the radar image

Then

$$S_r = S_K \times L_F \quad (2.48)$$

Step (2). Change slant range to ground range, as illustrated in Figure 2.6 and solved for in Equation 2.49.

$$G_r = \frac{S_r}{\cos\beta} \quad (2.49)$$

where β is a function of the terrain slope (α) and of the direction in which the slope is facing with respect to the sensor, i.e., either towards or away from the sensor.

When the slope is facing towards the sensor the terrain slope (α) must be added to β and by substituting Equation 2.49 into Equation 2.46, the final equation for calculating relative relief (R_R) becomes

$$R_R = \frac{S_r}{\cos(\beta + \alpha)} \cdot \sin \alpha \quad (2.50)$$

When the slope is facing away from the sensor α must be subtracted from β and the equation becomes

$$R_R = \frac{S_r}{\cos(\beta - \alpha)} \cdot \sin \alpha \quad (2.51)$$

The problems encountered with calculating terrain slope and relative relief from radar foreshortening along with the limitations of the method are dealt with in Chapters 4 and 5. It is sufficient to say that the use of radar foreshortening for morphometric data collection does have potential, especially as a supplement to morphometric data derived from radar shadows, with improved methods of measuring depression angle (β) and slope length (L_F) brought about by system calibration and more sophisticated measuring devices.

CHAPTER 3

QUALITATIVE EVALUATION OF RADAR-DERIVED GEOMORPHIC DATA

3.1 Introduction

When using most remote sensors which are concerned with any part of the electromagnetic spectrum other than visible light, the geoscientist is initially handicapped because he cannot normally utilize the interpretive techniques developed through experience. Instead, he must discover new "signatures" which may yield clues to identifying a particular terrain feature on the output array of the new remote sensing system. Aside from the inconvenience of limited stereoscopic vision, the basic interpretive techniques developed for photo-interpretation are quite applicable to the output array of SLAR systems, i.e., radar imagery. Most competent photo interpreters will find the transition from aerial photographs to radar imagery very similar to the transition required for changes from photography to infrared imagery. Thus for interpretation of radar imagery, the analyses of tone, texture, shape, and pattern become recognition elements which contribute to the interpretation of geomorphic, hydrologic, and geologic data on both a macro-scale (regional-sized geomorphic units) and a micro-scale (individual geomorphic features).

3.2 Regional Geomorphology

Geomorphologists interested in the delineation of landform units on a broad scale should be cognizant of the characteristics and potential of imaging radar systems. By obscuring minor and redundant detail, by imaging large areas, and by producing a two-dimensional output that closely resembles a pseudo three-dimensional map of the terrain, radar imagery provides patterns of information broadly conforming to grossly distinct areal differences, i.e., landform regions.

Although the defining and mapping of geomorphic regions appears to be a natural extension of the image output, its use as such a tool has been limited to very few studies. Schwarz and Mower (1969) found that their qualitative radar-derived landform units visually compared favorably with the well-established systematic-descriptive landform classification of Puerto Rico by Young (1953). Nunnally (1969), in a radar oriented study of the Asheville Basin in North Carolina, regionalized the area into "integrated landscape" units delimited by the combined association of physical and cultural phenomena. Nunnally (1969) concludes that the radar regions "do appear to correlate well with distinctive integrated landscape types...." Since there is a high inter-relationship between landform and land use units on the scale of Nunnally's study, his conclusions are also applicable to the regionalization of landforms with radar.

3.2.1 Route 17 Study Area

3.2.1.1 Background

To date no one has tested or demonstrated the quantitative congruency of a radar-derived and a map- and air photo-derived map of regional landform units. Route 17, a proposed route for a sea-level canal, was selected to test the usefulness of radar imagery for delineating landform units and to provide the quantitative congruency data primarily because good radar coverage was available and a map of the regional geomorphology, based on map-derived topographic and hydrologic data, had been completed. It should be mentioned that although the map of the regional geomorphology had been completed prior to the construction of the radar-derived geomorphic map, it was not available to the author until after the radar-derived map was finished.

3.2.1.2 Radar Geomorphic Regions - Criteria and Delineation

The delineation of the major geomorphic regions from radar imagery — plains, hills, and mountains (Figure 3.1) — was based on apparent relief and textural appearance directly related to radar shadowing and interpretable from the radar imagery. The extent of radar

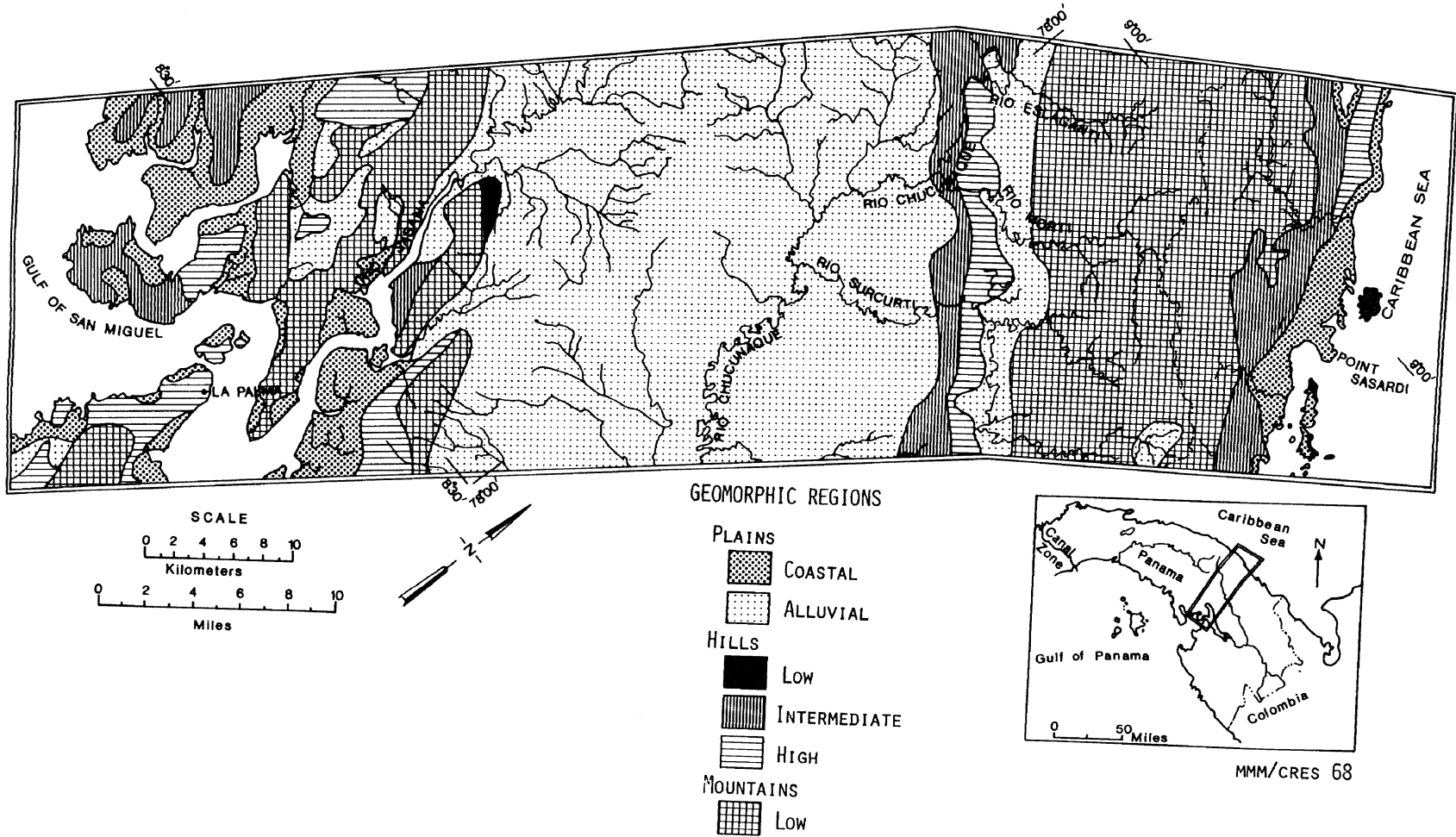


Figure 3.1 Geomorphic regions of Route 17 based on apparent relief and textural appearance interpreted directly from radar imagery

shadowing provided a basis for a qualitative measure of apparent relief even though it was realized, and taken into account, that the amount of shadowing within a given landform region varies with depression angle (Figure 2.17). When compared with areas of known relief, categories of apparent relief were established and extended by inference. Arrangement of radar shadows provided the macro-texture and acted as a discriminant on a general scale. Image texture, a function of the degree, orientation, and rate of change of slope was used (as well as vegetation cover) to further subdivide plains into coastal and alluvial categories and hills into low, intermediate, and high categories (MacDonald and Lewis, 1969 a and b).

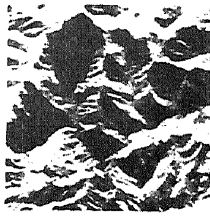
The criteria for the categories established in the Route 17 study are given in Table 3.1.

On a macro-scale the regions defined as plains exhibit a uniform tonal signature; however on a micro-scale the tonal values over short distances display a salt-pepper appearance (Figure 3.2). The tonal value for plains covered by rainforest is lower than that for mangrove covered plains providing a means of discrimination. In all cases, there was no radar shadowing in the plains category.

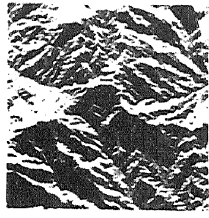
TABLE 3.1
RADAR-DERIVED GEOMORPHIC REGIONS FOR ROUTE 17

PLAINS — apparent relief 0 - 50 meters
COASTAL — predominately mangrove - high return
ALLUVIAL — predominately rain forest - moderate return
HILLS — apparent relief 50 - 350 meters
LOW — low relief, little dissection, smooth convex surface
INTERMEDIATE — moderate relief, moderately to highly dissected, hummocky plateau-like surface
HIGH — large relief, highly dissected, prominent ridge crests
MOUNTAINS — apparent relief greater than 350 meters; other features similar to High Hills, but characteristics are more pronounced

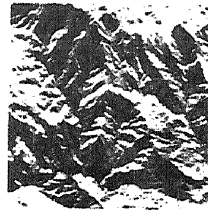
MOUNTAINS



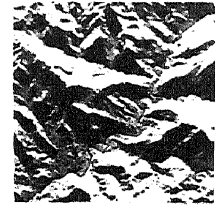
a



b

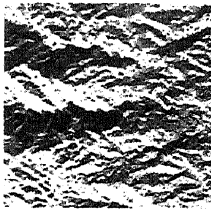


c

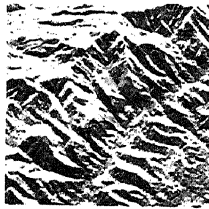


d

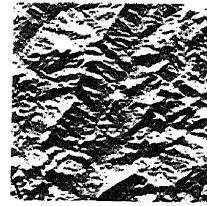
HIGH HILLS



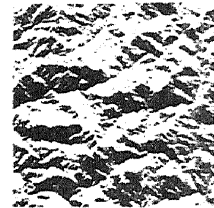
e



f

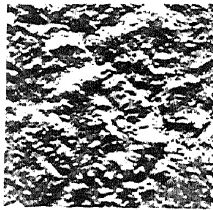


g

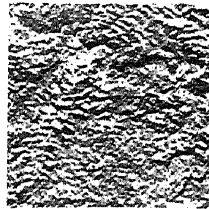


h

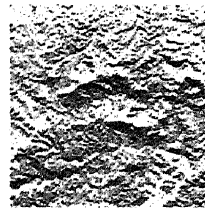
LOW HILLS



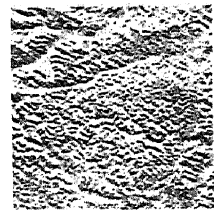
i



j



k

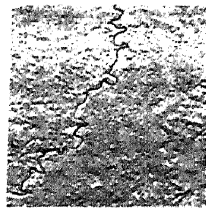


l

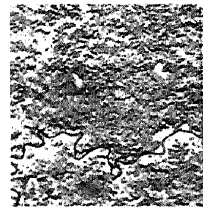
PLAINS



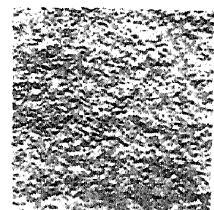
m



n



o



p

Figure 3.2 Radar chips from the four major landform regions in Darien Province, Panama: plains, low hills, high hills, and mountains

Radar shadowing indicated that the region was either hills or mountains (Figure 3.2). Further subdivision was based on the percentage of the radar image in shadow produced by landforms. For example, the mountainous areas exhibited radar shadowing over better than one-half of the range; whereas, hills had shadowing over less than one-half of the range. The gross tonal changes from very light to very dark areas, really macro-texture, found associated with steep topography aided discrimination between hills and mountains. Bright and dark areas, the illuminated and shadowed slope respectively, are also allied with hills; however, the size or length in the range direction of the bright and dark areas is less than that demonstrated in the mountainous regions indicating less or lower relative relief (Figure 3.2). In the regionalization of landforms in Route 17, hills were subdivided further into: (1) low hills if the tonal change from the front to the back terrain slope was gradual indicating smooth ill-defined crests; (2) intermediate hills if the tonal changes were abrupt but bright-dark areas were relatively small; and (3) high hills if tonal changes were abrupt and the illuminated-shadowed slopes were of moderate to large size. The distinction between high hills and mountains was based primarily on the percentage of the image in the range direction that exhibited extensive radar shadowing.

3.2.1.3 Map-Derived Geomorphic Map

The geomorphic map based on data derived from topographic maps (Dudley, 1966) used maximum slope angle and channel depth as criteria for delimiting the basic geomorphic zones that Dudley refers to as "physiographic divisions" (Table 3.2). Drainage pattern and density were used to subdivide the basic physiographic divisions into sub-regions.

3.2.1.4 Comparison of Radar and Map-Derived Geomorphic Maps

Since Route 17 is a rather nebulously defined area, as would be expected, the size and shape of the author's and Dudley's study area were not exactly congruent. The author's study area encompassed approximately 894 square miles; whereas, Dudley's study area was approximately 352 square miles. Since the central axis of Dudley's study area corresponded with that of the author's, 100 per cent overlapping coverage was obtainable for comparison.

TABLE 3.2

DUDLEY'S PHYSIOGRAPHIC DIVISIONS OF ROUTE 17

1.	Caribbean Coast
2.	Serrania del Darien ("Continental Divide" or San Blas Cordillera)
3.	Surcurti Depression
4.	Morti Ridge
5.	Chucunaque Basin
6.	Pidiaque Hills
7.	Nuno Range and Sante Fe Region
8.	Corredo Hills
9.	Punta Sabana
10.	Upper Cucunati Basin, Cucunati Hills, and adjacent rolling lowlands

Before correlating the two maps it was necessary to evaluate Dudley's physiographic divisions (Table 3.2) in context of the geomorphic regions used by the author. For example, it was found that Dudley's physiographic region actually consisted of: (1) flat depositional terrain; and (2) dissected erosional terrain. Since these subdivisions of the Caribbean Coast were more parallel to the author's plains and hills categories, respectively, the modification was made prior to comparing the two maps. Maximum slope angle was used primarily to reconstitute the rest of Dudley's regional units with the author's. The criteria were as follows:

- (1) If the maximum slope angle was less than 15° the region was reclassified as plains. This included part of divisions 1, 6, and 7 and all of divisions 3 and 5 in Table 3.2.
- (2) If the maximum slope angle was greater than 15° but less than 30° the region was reclassified as hills. This included part of divisions 1, 6, and 7 and all of division 4 in Table 3.2.
- (3) If the maximum slope angle was greater than 30° the region was reclassified as mountains. This included parts of 6 and 7 and all of divisions 2, 8, and 9 given in Table 3.2.

Division 10, the area approximately six miles northwest of La Palma on Figure 3.1, was not used in this comparative study because Dudley effectively classified all three of the author's landform regions into one unit which he chose not to subdivide because of the "small scale of the terrain elements." It is interesting to note that the scale factor which prohibited further subdivision by Dudley did not prevent detailed delineation of landform units on radar imagery (Figure 3.1).

The maps were correlated by first, reconstituting the maps to the same scale; second, overlaying a transparent grid divided into one quarter of a mile square (0.25 square miles); and third, totaling the units of agreement and disagreement of the author's three main landform regions, plains, hills, and mountains. The results, tabulated in Table 3.3, unquestionably demonstrate the similarity between the geomorphic map of the author and the map-derived landform map of Dudley (1966).

TABLE 3.3
 PERCENTAGE OF AREAL AGREEMENT BETWEEN RADAR- AND
 MAP-DERIVED LANDFORM MAPS OF ROUTE 17

Landform Regions	Total Number of Areal Units ¹ on Radar Derived Landform Map	Number of Areal Units on Radar Map in Agreement with Dudley's Landform Categories	Percentage of Agreement
Plains	483	463	95.9
Hills	83	75	90.4
Mountains	239	236	98.7

¹One areal unit is equivalent to 0.25 square miles

I did not determine the percentage of agreement between the subdivisions of the major landform regions on the two maps since it was felt that reconstituting Dudley's sub-regions to fit the author's would be an insurmountable task because of the discrepancy in the criteria used by Dudley, landscape characteristics, and those used by the author, image characteristics, for the subdivision of the major landform regions.¹ Because of this discrepancy, the agreement on the subdivision level would not be as high as with the major landform regions. It should be noted that in some cases the criteria used by Dudley enabled a finer landform subdivision than the criteria used by the author. However, in just as many situations this was reversed, i.e., radar landform subdivisions were finer than the subdivisions from topographic maps.

3.2.2 Geomorphic Map of Darien Province

After completion of the geomorphic map of Route 17 and its favorable comparison with a geomorphic map from topographic map data, the method

¹The landscape characteristics used by Dudley were drainage pattern and drainage density; whereas, the image characteristics used by the author were the rate of tonal change across the crest for the subdivision of hills and the relative tonal value for the subdivision of plains.

evaluated above was utilized to produce a map of the regional geomorphology of the entire Darien Province of Panama and part of Northwestern Colombia. Two of the geomorphic categories used in Route 17 (Table 3.1) were modified for the map. The changes were: (1) eliminating the subdivisions for plains; and (2) combining intermediate hills with low hills.

The regions were defined on the original strips of radar imagery of the Darien Province and then transferred to a base map. Regional boundary definition was not always made with the same level of confidence. The boundaries delimiting plains from the other categories were made with the highest level of confidence, whereas the boundaries between high hills and mountains would rank second in degree of confidence, while the boundary between low and high hills would be third. The varying degrees of confidence levels is basically due to the uniqueness of the topographic expression available from SLAR imagery for each geomorphic category. It is felt that the final product (Plate I) represents the most detailed, accurate, up-to-date map of the regional geomorphology of the Darien Province of Panama. This is in large part due to the inaccessibility of the area for field data collection and the inability to obtain complete photographic coverage of the area because of the near perpetual existence of cloud cover. The radar imagery as such provides the first regional look and source of regional data of the study area.

3.3 Individual Geomorphic Features

Although the synoptic presentation of radar imagery is of prime interest to the geomorphologist, the identification of geomorphic patterns and features on a local-scale generally provides information relating to the genesis, process, and lithology of the region and credibility to the delineated landform regions. The examples in the rest of this chapter illustrate several of the geomorphic features interpretable on radar imagery and the types of information that can be gleaned from such interpretations.

3.3.1 Coastal Features Within the Study Area

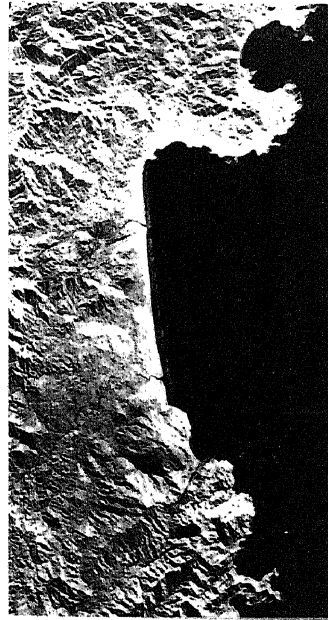
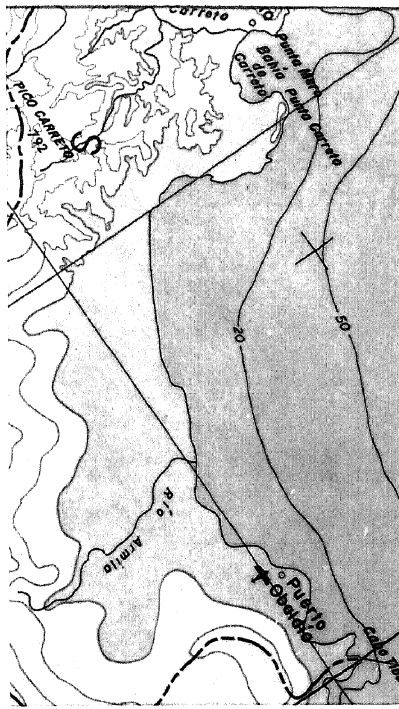
3.3.1.1 Shoreline-Coastal Configuration

Depending on the relative surface roughness¹ of the terrain, the signal return from vegetation, rock, soil, etc. is generally higher than the signal return from water. Therefore when water bodies (such as lakes and rivers) are imaged, they normally appear "smooth," and as such act as specular reflectors directing the transmitted energy away from the receiver. Terrain features, especially those covered by vegetation, appear "rough" to imaging radar systems and as such not as strongly dependent on angle of incidence. When imaging the land-water interface with SLAR systems, a relatively high signal return is recorded from the land whereas no return is recorded from the water. The large ratio of return between land and water produces a striking interface which is extremely advantageous in the delineation and mapping of the coastline configuration. Figures 3.3A and 3.3B illustrate this useful characteristic of radar imagery by revealing obvious discrepancies along the Caribbean Coast of the Darien Province, Panama between the most recent map and radar imagery of the coastline. These illustrations also provide evidence that sequential mapping by radar and ultimately the production of ortho-maps from imagery would result in a practical and rapid method of updating coastal maps (MacDonald, Lewis, and Wing, 1971).

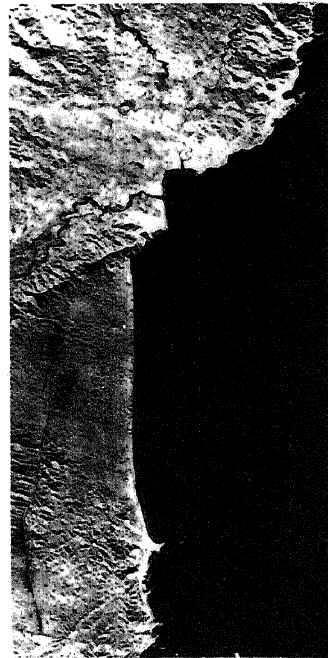
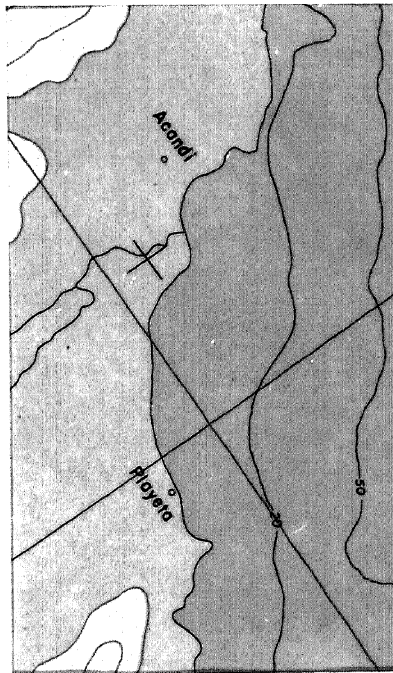
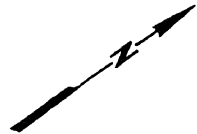
3.3.1.2 Tidal Flats

Tidal flats usually exhibit striking patterns on air photos. On radar imagery the pattern is also unique because of its offshore location, herring bone drainage-texture, high tonal contrasts with the adjacent water, and marked textural contrast with the land. The tidal flats on the Pacific coast of east-central Panama (Figure 3.4) are generally nonorganic, fluvio-marine accumulations occurring in shoal areas, and like most coastal areas where such features are found, they are protected from strong wind and current action. Tidal flats, such as those indicated by arrows

¹Surface roughness is not an absolute roughness, but the relative roughness expressed in wavelength units. For a surface roughness much less than the wavelength ($\lambda/10$) the surface appears "smooth" to the imaging radar, while for a surface roughness on the order of a wavelength or more, the surface appears "rough."



0 5 10 15 Km



Caribbean Coast - Eastern Panama

Map Data 1966

Radar Imagery 1967

Figure 3.3 Comparison of Radar imagery and topographic maps, Instituto Cartografico Tommy Guardia, Sheet # 11, La Palma, Panama, 1:250,000, 1966 Contour Interval - 30 meters

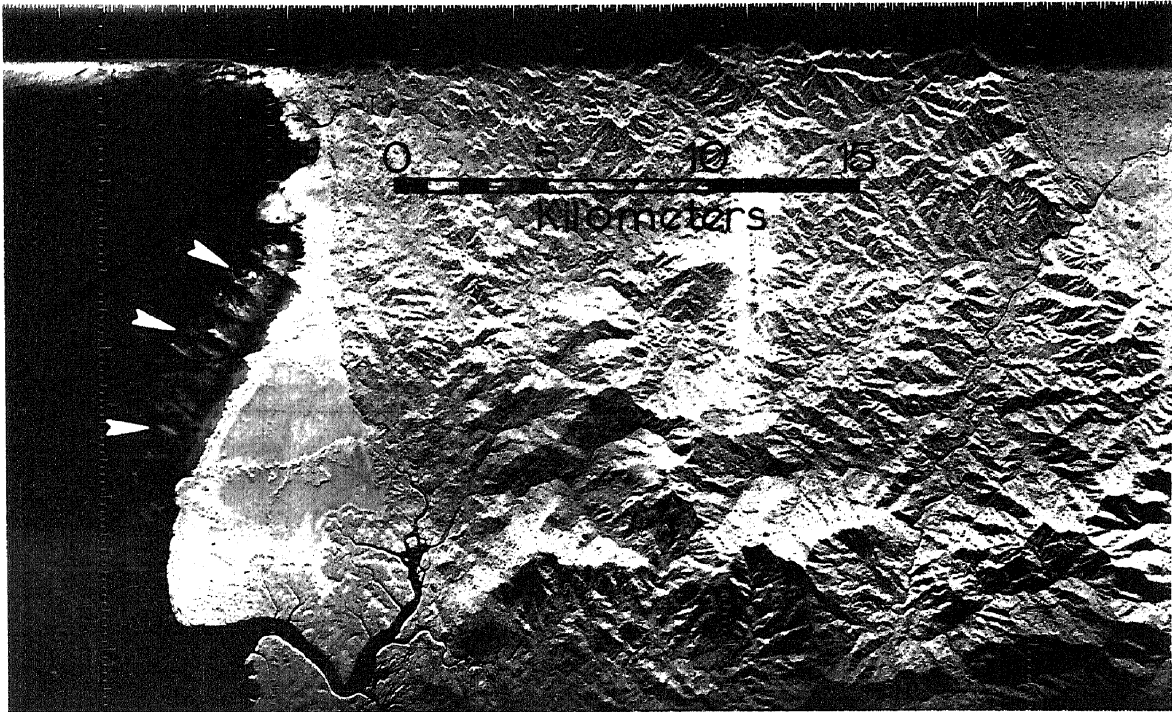


Figure 3.4 Radar imagery, tidal flats along Pacific Coast east-central Panama, mouth of Rio La Meastra lower left of imagery.

on Figure 3.4, are believed to be the first stage in the formation of mangrove swamps and exhibit a slightly undulating surface devoid of vegetation. In this particular location, extensive mangrove swamps can be delineated shoreward of the tidal flats.

3.3.1.3 Mangrove Coasts

Mangrove swamps, which abound on tropical shores throughout the world, are a readily recognizable vegetation type unmistakably identifiable on radar imagery. On Figure 3.7, the number two (2) identifies the boundary between mangrove vegetation to the north and jungle vegetation to the south. Proximity to coastal waters combined with bright return and a fine textural pattern aid in delineation of the mangrove swamp limits.

3.3.1.4 Beach Ridges and Wave Refraction

Beach ridges provide evidence (Figure 3.5) of progradation along the Pacific coast between the Rio Bayano Estuary and the Panama Canal. Back-swamp drainage is well defined north of the beach ridges, while to the east the outline of a mangrove swamp is equally apparent. A wave refraction pattern can be delineated (black arrows) along the upper margin of the imagery.

3.3.1.5 Barrier Reefs and Surf Zone

Off the Atlantic coast are the San Blas Islands (Figure 3.6) which consist of coral sand that have collected on the leeward slopes of barrier reefs. The outline of the windward part of the reef is delineated by the surf zone (arrows - Figure 3.6). Landward from the San Blas Islands, coral flats fringe the coast, but this cannot be determined from imagery interpretation; however, the occurrence of these dense clusters of dead corals at the present sea level was noted in a study by Tuan (1960, p. 24).

3.3.1.6 Shell Reefs

"Shell reefs" as used in this study refer to narrow linear accumulations of shells and shell fragments oriented perpendicular or at a high angle to the shoreline and situated on, but above, tidal mudflats off the mangrove coast east of Garachine in the Gulf of San Miguel. The reefs are exposed only during low tide, and although most of the reefs are

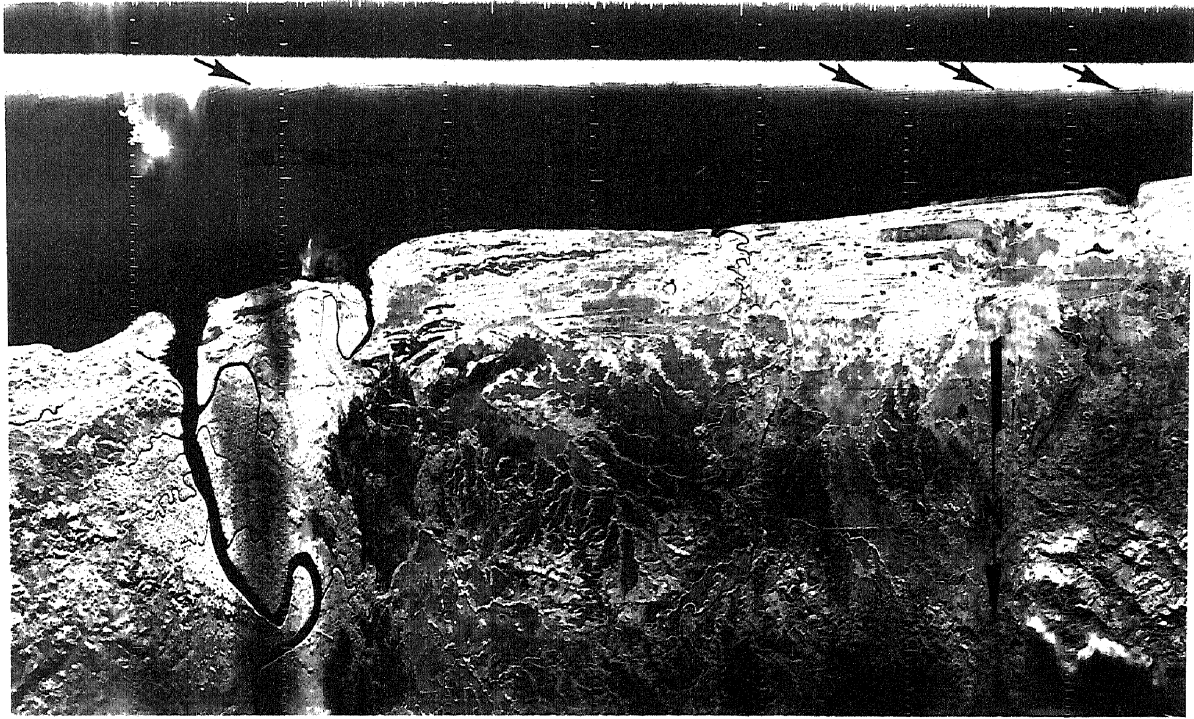


Figure 3.5 Radar imagery, beach ridges along Pacific Coast east-central Panama, mouth of Rio Bayano left center of imagery.

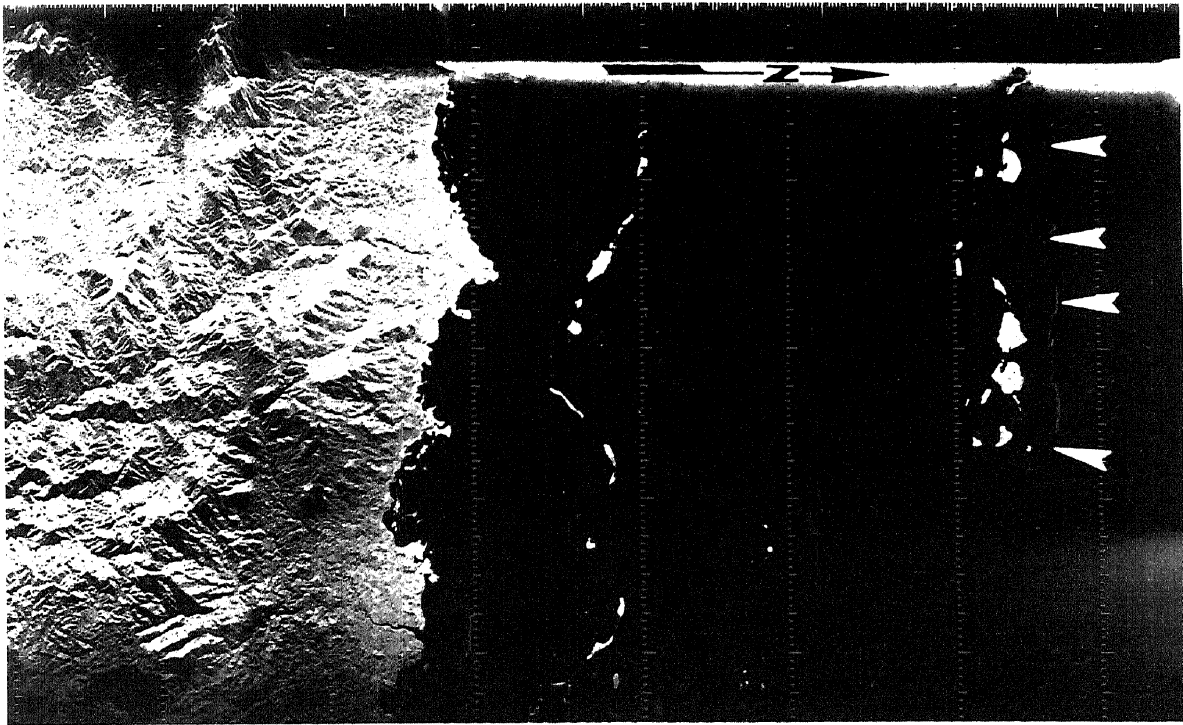


Figure 3.6 Coral sand islands on leeward slope of barrier reef, surf zone (arrows) outline windward part of reef.

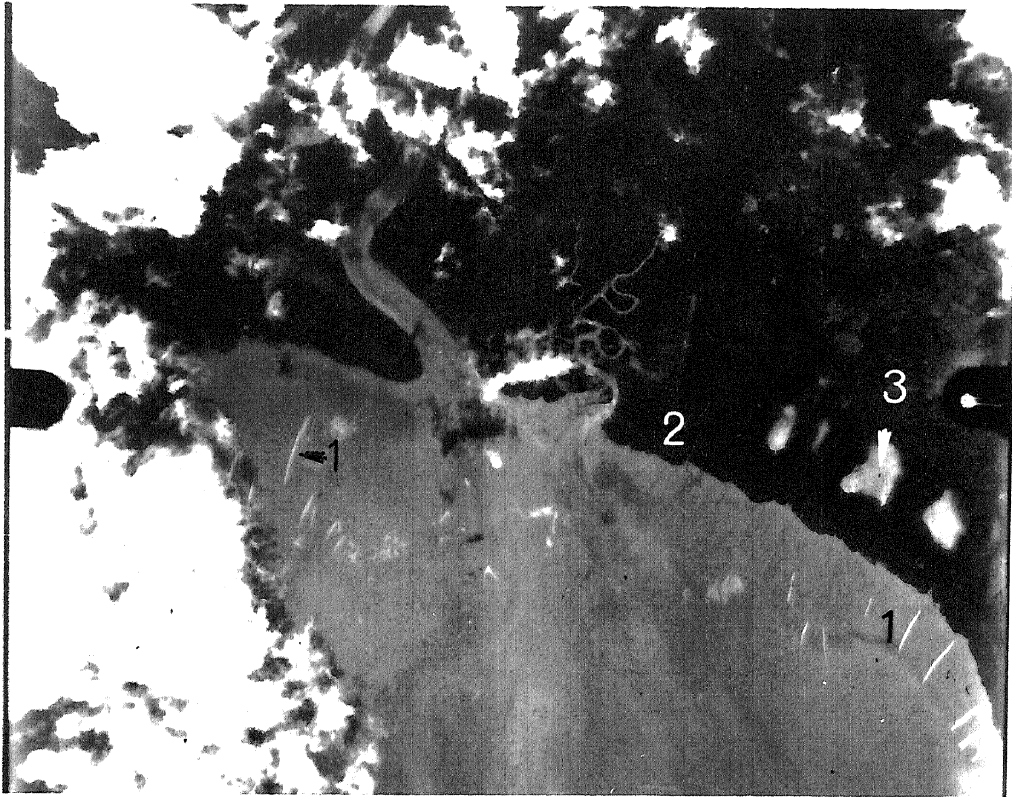
detached from the coast, several extended back into the mangrove for a considerable distance. The average width of the shell reef is approximately 100 meters, the length approximately one kilometer.

The shells that make up the reefs in San Miguel Bay are mostly those of small clams (Anomalocardia subragosa and Protothaca grata) commonly found on mudflats in shallow water along the Pacific Coast from lower California to Southern Peru (Keen, 1958). Although no living pelecypods were found on the exposed surface, living clams were observed approximately six inches below the surface at the top of the water table for low tide. Unattached gastropods and other macro-fauna were found on the surface of the reef several hundred meters back of the coastline and under the mangrove canopy.

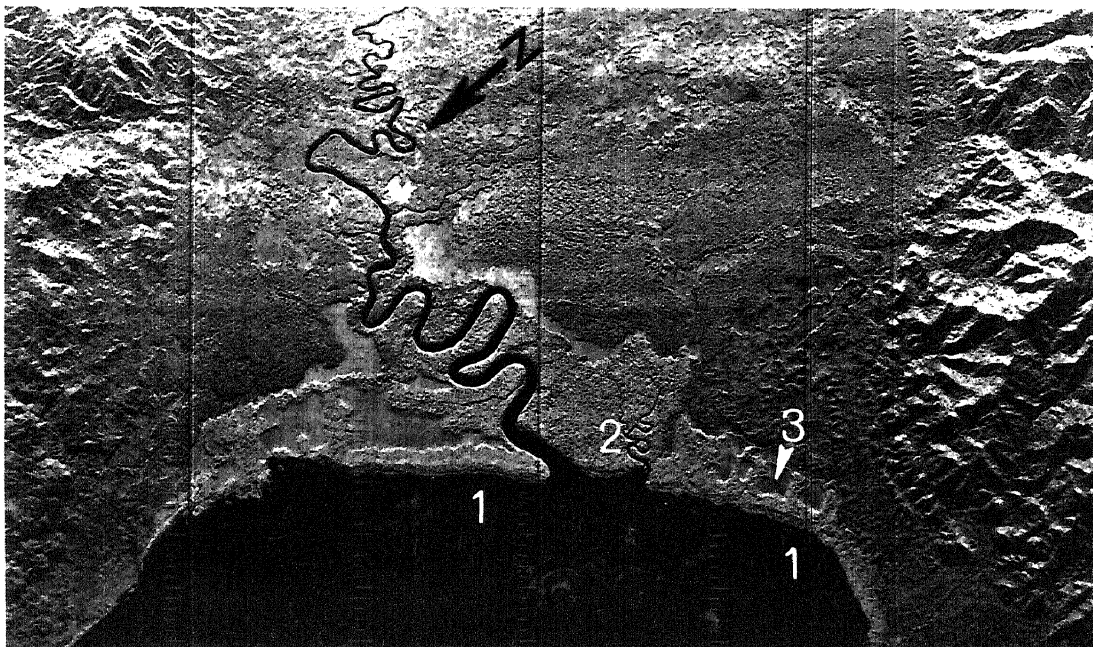
Figure 3.7 illustrates the shell reefs as they appear on both radar imagery and aerial photography. On both the radar imagery and aerial photography, the shell reefs are detectable because of their light tonal value. Geometric shape and coastal situation also aid in identification.

A geomorphic feature similar to these shell reefs are "oyster reefs," first described by Grave (1905) in North Carolina. Oyster reefs have since been described in many of the bays, marsh lakes, and tidal channels of Louisiana (Tompson, 1956; Kolb and Van Lopik, 1958; and Coleman, 1966) and Texas (Norris, 1953; and Shepard and Moore, 1956). They have also been observed in Australia in Upstart Bay in the Burdekin River Delta (James Coleman, personal communication).

Studies by Grave (1905) and Parker (1960) have shown that the alignment of the oyster reefs is directly related to the circulation or current direction, i.e. the growth is always at right angles to the direction of flow. This is in response to the supply of nutrients. The growth of an oyster reef is illustrated in Figure 3.8. After the initial stage (A), the reef grows perpendicular to the nearshore current reaching the current channel (B) where continued growth causes a deflection of the current and re-establishment of the current channel further offshore (C). As the deflection increases two conditions become apparent, (1) the current no longer flows past the reef at a right angle, therefore new



Aerial Photography



Radar Imagery

Figure 3.7 Radar imagery and aerial photograph of shell reefs (1), mangrove (2), and non-vegetated areas associated with semi-dry mangrove coasts (3) east of Garachine in San Miguel Bay

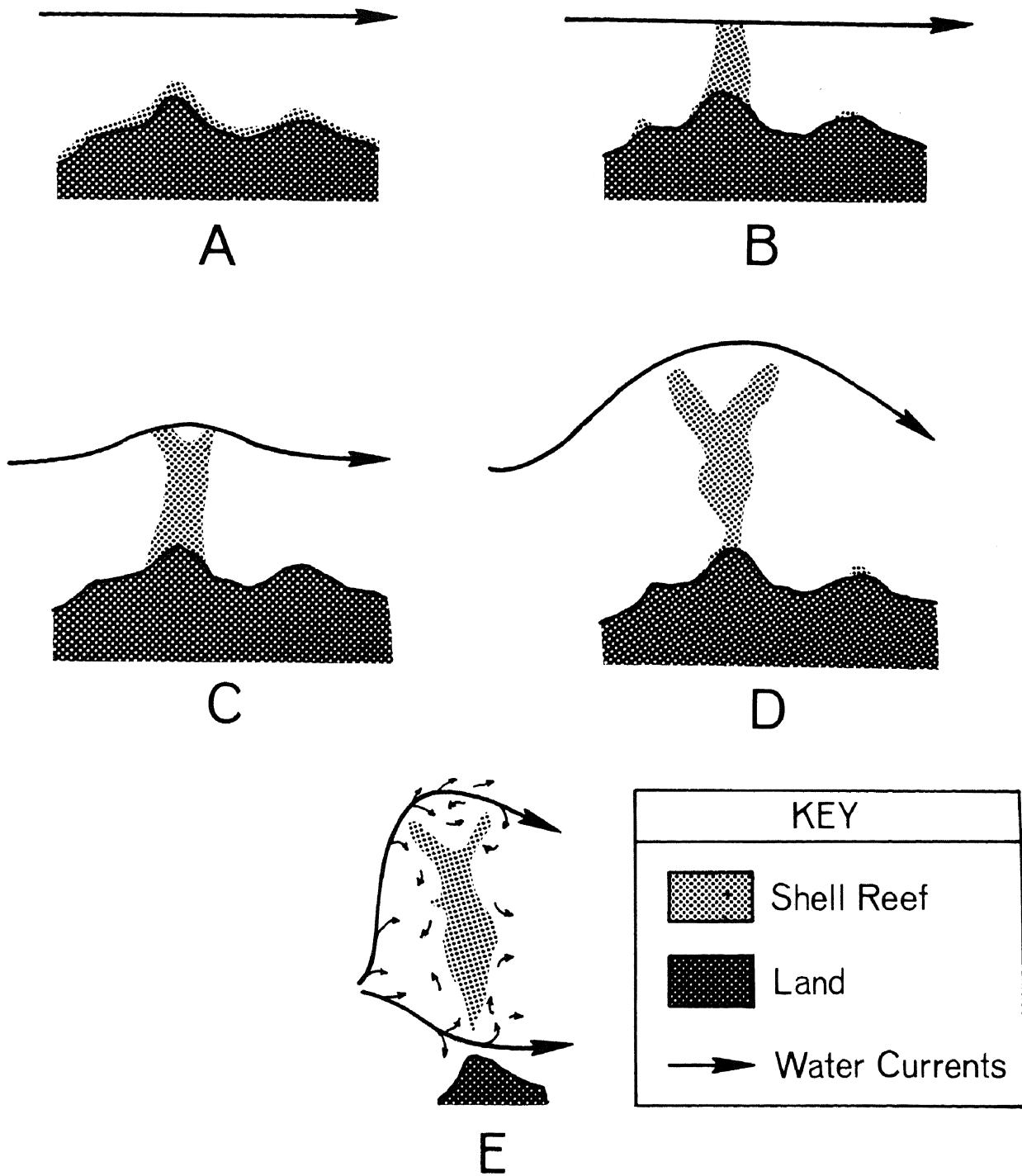


Figure 3.8 Conditions near a shell reef and the steps by which a reef may be formed. Stippled pattern represents shell reefs. Arrows indicate the direction of water currents. Irregular line represents shore line (after Grave, 1905).

conditions for growth occur and the reef responds by bifurcating (D) and (2) the supply of nutrients along the coast is depleted, the reef dies and the width is gradually reduced until it is finally breached by the near-shore current and the reef is separated from the land (E) (Graves, 1905).

A firm substratum at the base of the oyster reefs was also found to be prevalent (Parker, 1960), which Coleman (1966) correlated with ancient distributaries in marshy areas and concluded that the abandoned distributary trends were one of the main controlling factors in controlling the distribution of oyster reefs in Louisiana.

Although the species involved in the reef formation are not the same as those reported above, it is believed that the processes involved in the formation of the reefs in Panama are the same, that their growth pattern is a reflection of the nearshore circulation pattern, and their location is related to old or even existing small tributaries flowing into the Gulf of San Miguel.

3.3.1.7 Non-Vegetated Areas Behind Mangrove Coasts

The flat, vegetation-free zones (Figure 3.7), either within the mangrove swamps or between the mangroves and higher ground, indicate that the coast in each area has (1) a very large tidal range, and (2) a dry, or seasonally dry, climate (Fosberg, 1961, p. D-217). Fosberg reported this phenomena along many tropical coasts and suggested that these flat, bare areas are inundated only a short period of the month by high spring tides and then dried out, resulting in high salt concentrations. The combination of high salt concentrations with extreme dryness during the dry season probably exceeds the tolerance level of both halophytes and xerophytes, leaving the area void of vegetation.

The identification of such features along the northwest coastal portion of the Darien Province substantiates the presence of a large tidal range indicated by the occurrence of estuarine meanders. It also suggests a strong seasonal wet and dry rainfall regime, a condition verified in the field by sclerophytic and xerophytic plants along the coast in San Miguel Bay between Punta Garachine and Punta Alegre.

3.3.1.8 Estuarine Meanders

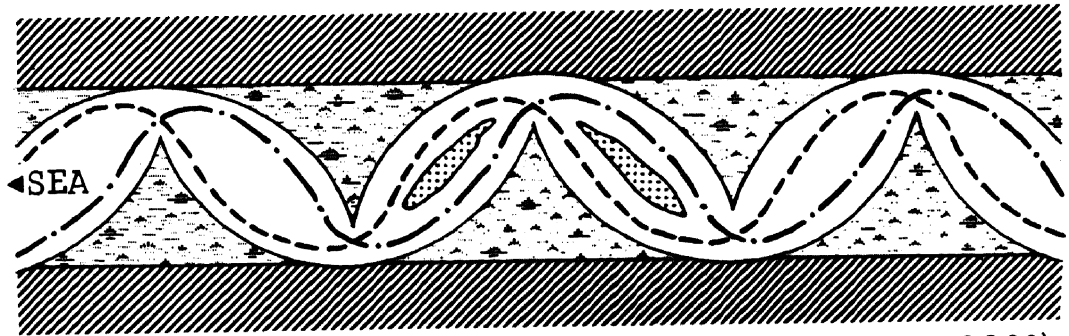
The identification of estuarine meanders is based primarily on a planimetric shape (Figure 3.9) first described by Ahnert (1960) as a "succession of oblong pools connected by narrow channels at the bends." Gravel bars, exposed during low flow, are found oriented parallel to the major axes of some of the oblong pools. The constriction at the bend is characteristically covered by recent material deposited during the slack period of high tide and shaped by flood and ebb currents hugging the outside bend of the meander, as shown in Figure 3.9.

Estuarine meanders differ from river and tidal meanders by their position in the fluvial-marine scheme of a hydrologic system and by their relationship to a specific family of curves. Whereas river meanders form where the fluvial regime is paramount and tidal meanders develop under tidal conditions where the marine regime is paramount, estuarine meanders form where fluvial and marine influences are nearly equal. Estuarine meanders, therefore, are coincident with the transitional zone between marine and fluvial processes and can be considered a marriage of the two processes.

River meanders closely approximate a sine-generated curve, presumably to eliminate concentrations of energy loss and to reduce total energy loss to a minimum rate (Langbein and Leopold, 1966). The similarity in shape of river and tidal meanders permits the extension to tidal meanders of the minimum-variance theory for energy distribution in river meanders. Estuarine meanders, however, differ markedly from the sine-generated curve since their planimetric form approximates two cycloid curves originating on opposite sides of the thalweg. The curves are shifted one-half period from each other and are separated by a distance approximately equal to the channel width.

The large variation in radar return from water versus land, as mentioned previously, combined with their unique shape provides easy delineation of estuarine meanders on radar imagery. Figures 3.10A and 3.10B are examples of two of the eight regions in which estuarine

SCHMATIC DIAGRAM OF ESTUARINE MEANDERS



(modified from Ahnert, 1960)

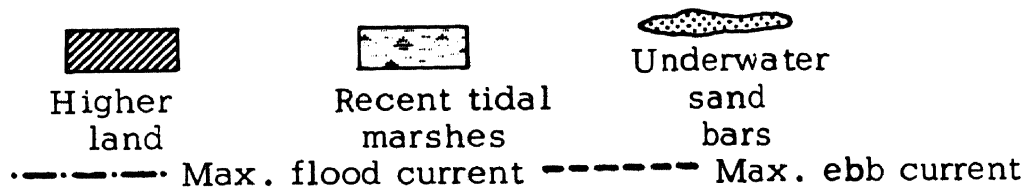


Figure 3.9 Schematic Diagram of Estuarine Meanders

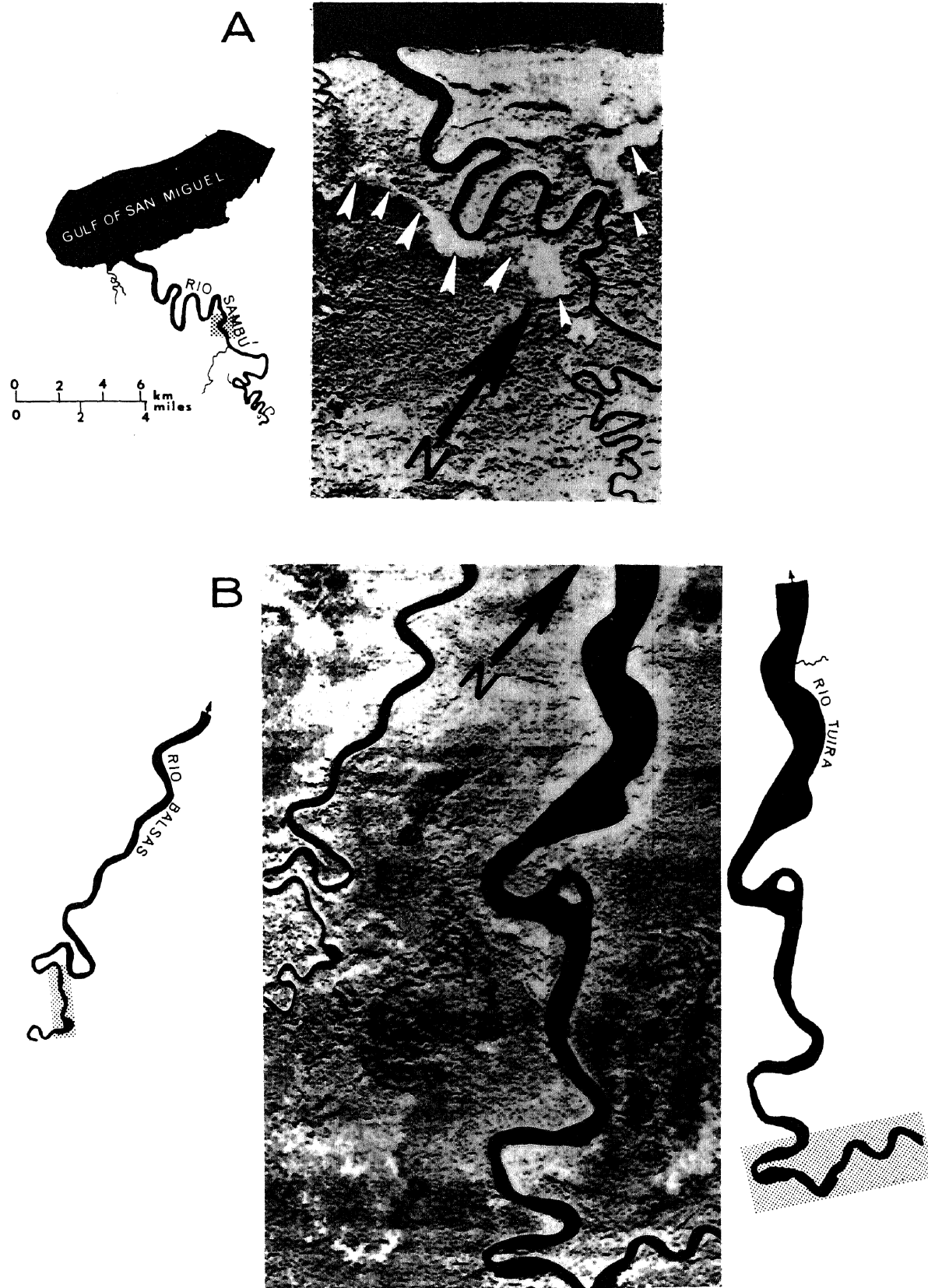


Figure 3.10 Radar imagery and silhouette diagrams, zones of estuarine meanders within stippled areas

meanders were found on radar imagery of eastern Panama (Figure 3.11).¹ The obvious dearth of estuarine meanders on the Caribbean side of eastern Panama and northwestern Colombia is probably related to (1) relatively small drainage basins, (2) low rate of sedimentation in the coastal zone, (3) small tidal range, (4) narrow coastal plain, and (5) relatively low energy environment found on the Caribbean side as compared to the Pacific side, especially in the Bay of Panama (Lewis and MacDonald, 1970).

The occurrence of estuarine meanders provides insight into the environmental conditions of the coastal area. Based on the necessary, or at least the optimum conditions, under which these meanders develop, inference can be carried to areas where field data collection is not practical.

Upon identifying the morphometric form of the estuarine meander one can conclude, with some qualification, that the following statements are applicable for the area concerned:

- (1) The coast has remained relatively stable during the recent past.
- (2) The coast is a low-to moderate-energy environment.
- (3) There is a relatively large source of available sediment.
- (4) The channel flow is bi-directional.
- (5) Within the estuarine meander belt, the marine influence of the tide is comparable to the fluvial influence of the river.
- (6) The maximum current velocity for both the ebb and flood tide occurs at mean water level within the estuarine meander belt.
- (7) The effect of rhythmic tidal movement extends upstream from the estuarine meander belt (Ahnert, 1963).

The occurrence of estuarine meanders also provides insight into the type of coast. Ahnert (1963), using Valentin's coastal classification scheme, states that estuarine meanders are strongly associated with lagoonal, mangrove, and coastal plain coasts and suggests that in each case the estuarine meander represents the evolution of a constructional

¹Location 6 on Figure 3.1 corresponds to the estuarine meander zone on Figure 3.10A, whereas Location 7 on Figure 3.11 corresponds to Figure 3.10B.

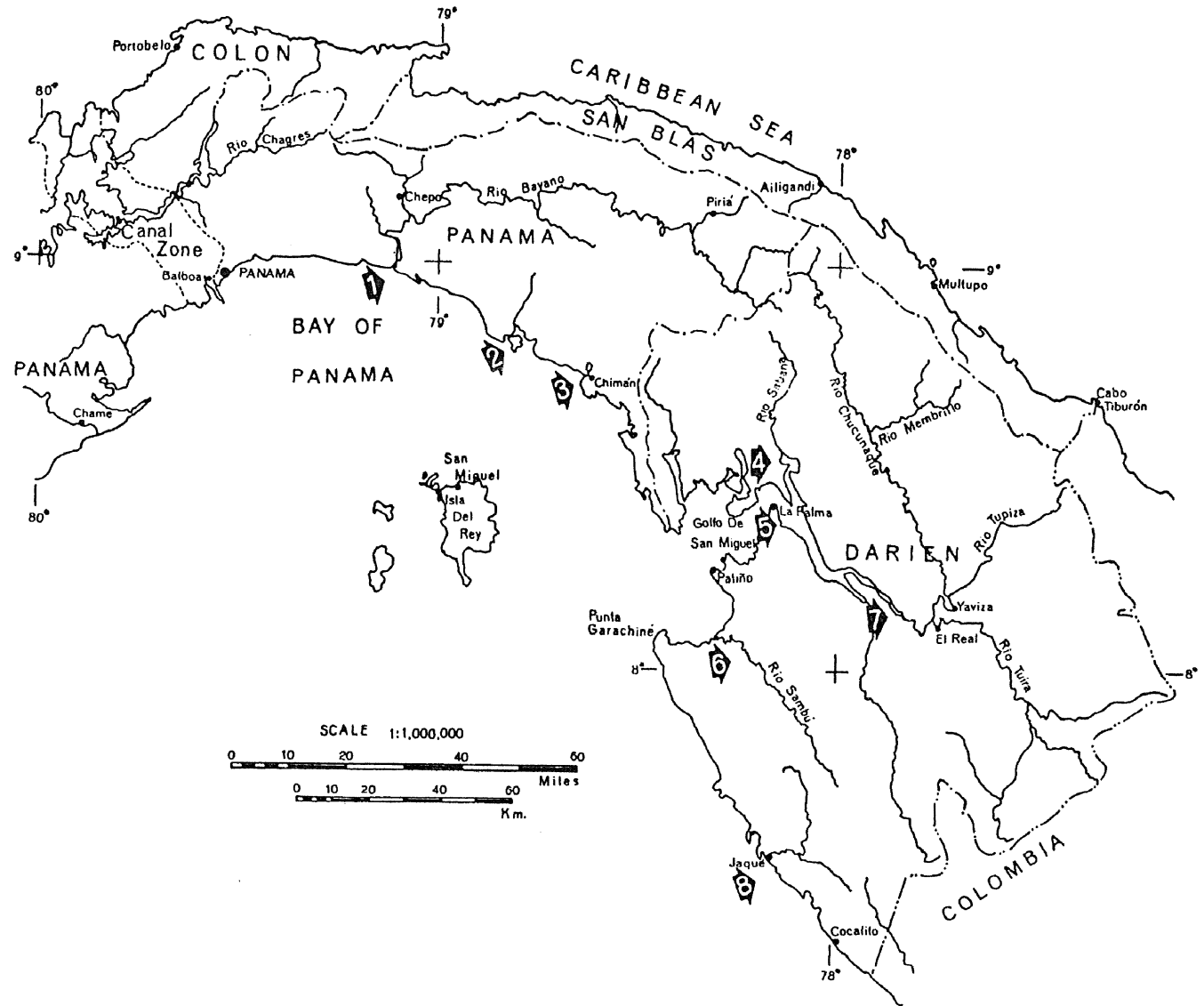


Figure 3.11 Location map of zones of estuarine meanders in eastern Panama.

coast. The position of the meander belt reflects a phase of estuary filling, since estuarine meanders are believed to be dynamic: they are initially formed at the head of the tide, and subsequently migrate downstream to the mouth of the river. Eventually the estuary becomes completely filled with sediment. Examples of both the intermediate and final stage of estuarine meander migration are evident in the study area.

The above examples of estuarine meanders interpreted from radar imagery have been related to constructional processes where fluvial conditions are encroaching upon marine conditions. However, these features have also been identified where marine influences are overcoming fluvial influences, and in such instances estuarine meanders are considered as evidence of destructional processes. Estuarine meanders found in abandoned distributaries of deltas are destructional features. Here they represent a change from the river meander, developed under conditions of strong uni-directional flow, to the estuarine meander, developed where tidal currents recently became the major agent of erosion and transportation. Eventually, the estuarine meander will be destroyed and a tidal meander will be formed under the increasing influence of tide. Although Ahnert found no strong relationship between estuarine meanders and tidal range, it seems reasonable that with all other conditions being equal, a large tidal range would offer a greater chance for the development of estuarine meanders than would a small tidal range.

The significance of delineating this coastal form in relatively unmapped areas is the increased knowledge of the balance between marine and fluvial processes, availability of fine sediment, type of coast, and relative stability of sea level.

3.3.1.9 Delta Features - Atrato Delta

The delta of the Atrato River is located on the southwestern side of the Gulf of Uraba in northwestern Colombia. The delta forms a coastal lowland belt bounded on three sides by mountains, thus the Atrato receives large quantities of water from the mountain run-off. Vann (1959) has shown that the Atrato Delta exhibits physical features which permit recognition of recent changes by analyzing landform and vegetation. Landforms in the delta consist of mudflats, natural levees, backswamp

basins, and round lakes. Figure 3.12 is a summary of Vann's investigation of the Atrato Delta. Figure 3.13 is a comparison between the 1954 coastal conditions, constructed by Vann in the field and from aerial photographs, and the coastal configuration as recorded by radar imagery some 13 years later. Since 1954, the northern spit (Figure 3.13, Area 1) has been either eliminated by wave action or it has been breached, then later connected from the south by a spit-like tombolo (2). Encroaching vegetation from the natural levee (3) in the main channel reflects a reduction in stream flow. The largest lake in the region (4) is now being reduced in area because of sedimentation, and appears to reflect the initial stages in the formation of an inland swamp. Contrasting Vann's study with that of the radar imagery suggests that Vann's projection of coastal retreat was correct.

Vann (1959) also studied the major vegetation types in the delta and their usefulness in geomorphic interpretations. Figure 3.14 provides a comparison of Vann's vegetation map with radar imagery of the Atrato Delta. As can be seen, the two compare quite favorably, in fact four of the five vegetation types can be discriminated on the radar imagery. Mangrove and the pángana community¹ are especially easy to delimit, as is the palm community, if it is bounded by mangrove and the pángana community. However, distinguishing the palm community when juxtaposed with the grass and sedge community is difficult because the ratio of radar return between the two plant communities is not sufficient to describe a sharp boundary. Aquatic herbs are only barely distinguishable on the imagery.

The importance of being able to identify the vegetation types is the high correlation of vegetation type with topographic and hydrologic conditions. The mangrove zone is found only along the coastline within the tidal range; the pángana community on the well-drained natural levees; the palm community in the transition zone between the natural

¹See Vann (1959) for a more complete description of the vegetation species and their characteristics that make up the five plant communities in the Atrato Delta.

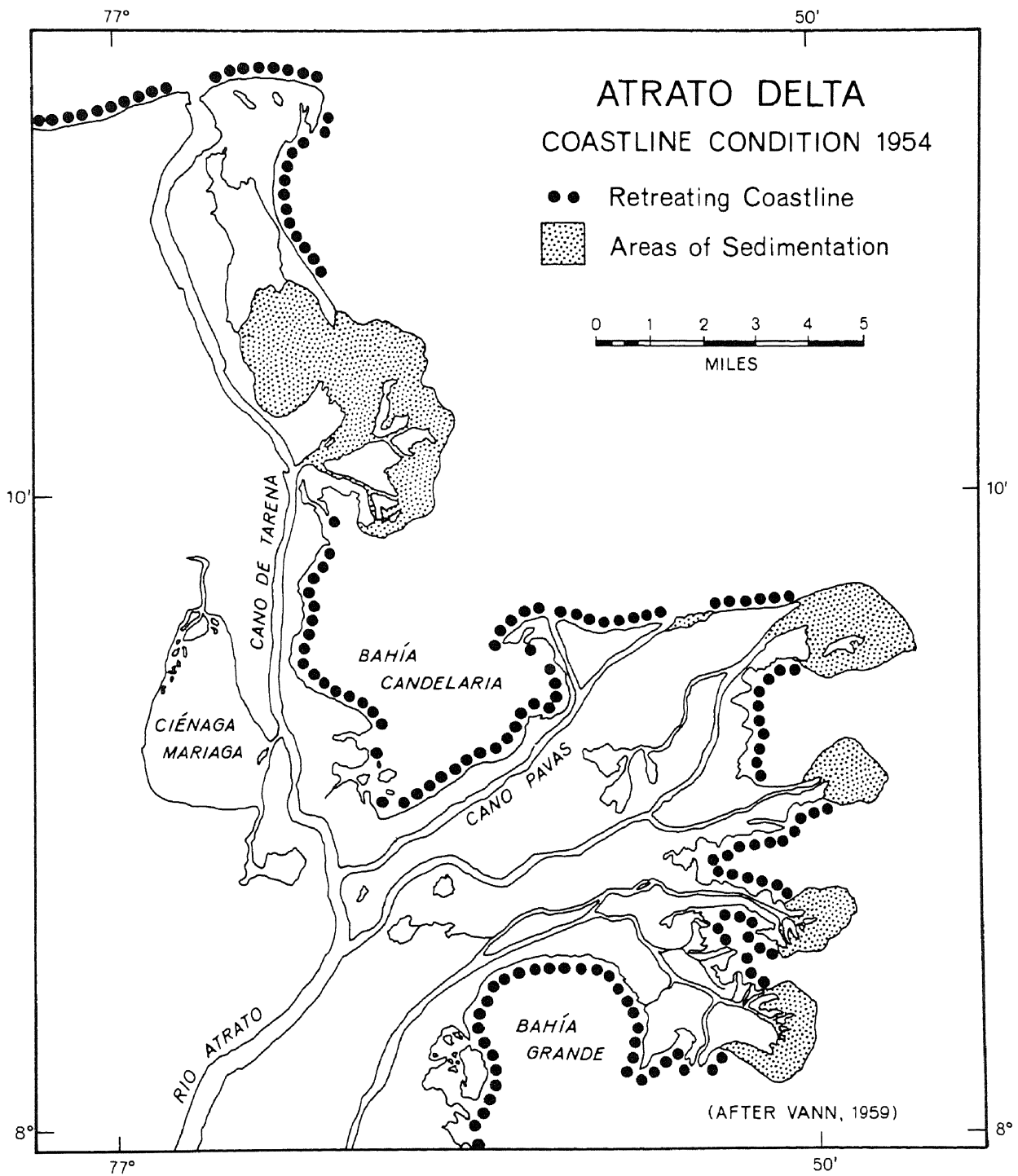


Figure 3.12 Atrato Delta Coastline Conditions, 1954

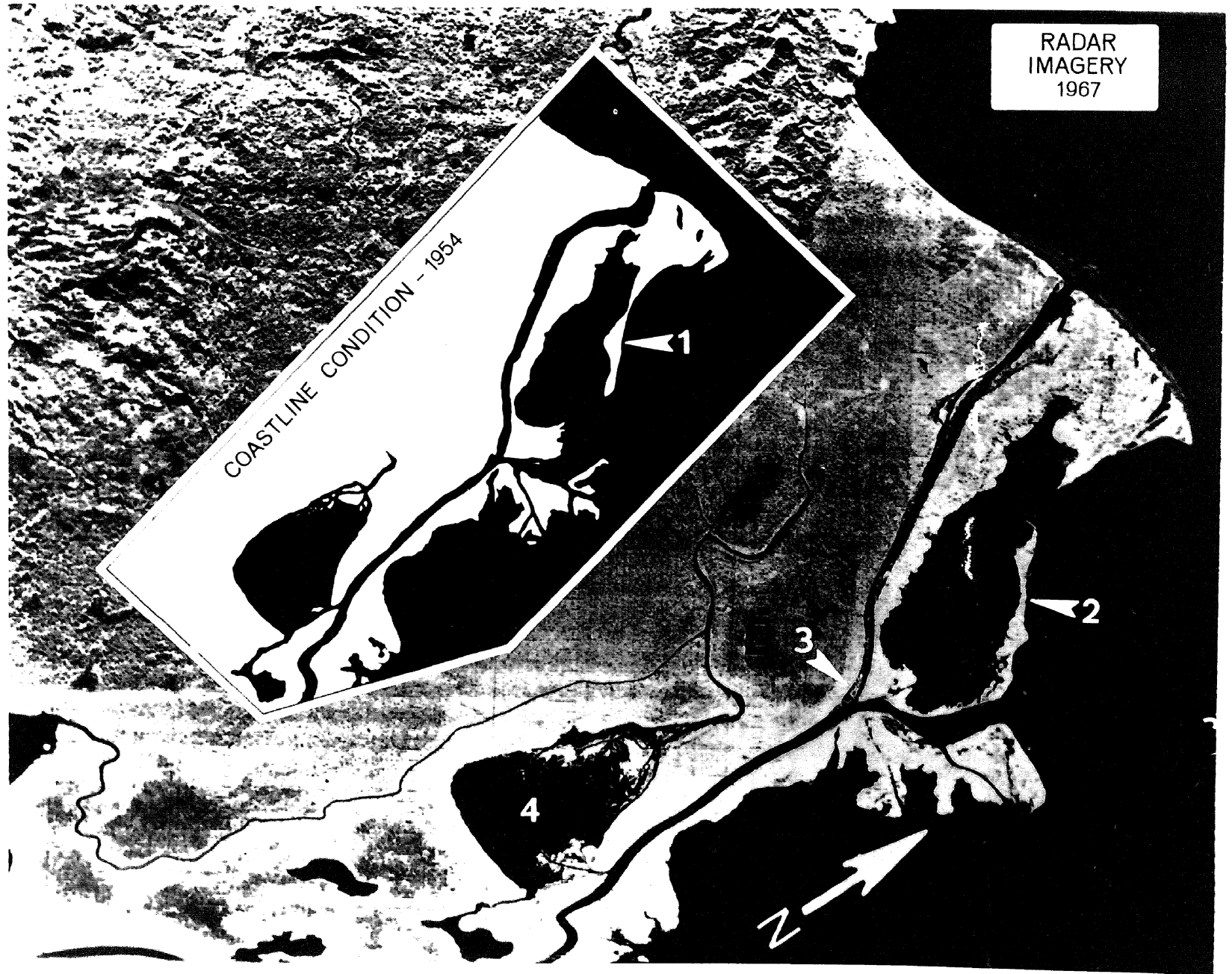


Figure 3.13 Comparison between radar imagery (1967) and coastline conditions of 1954

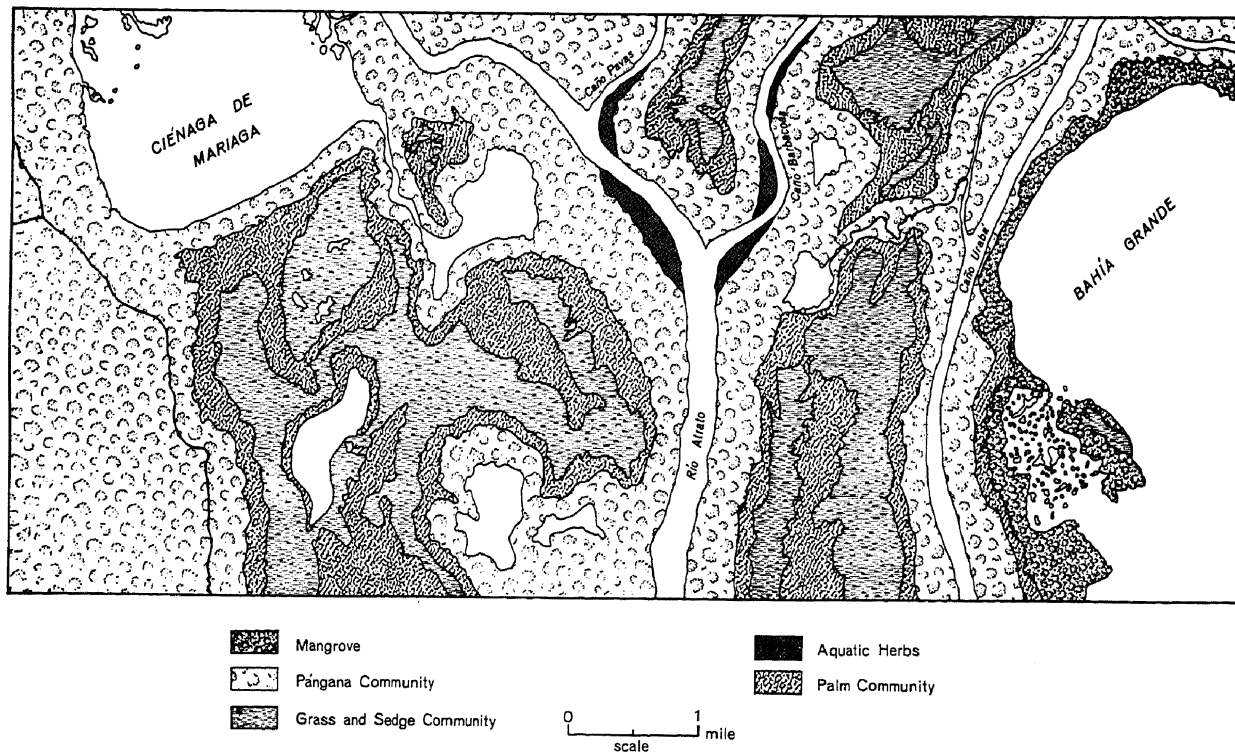
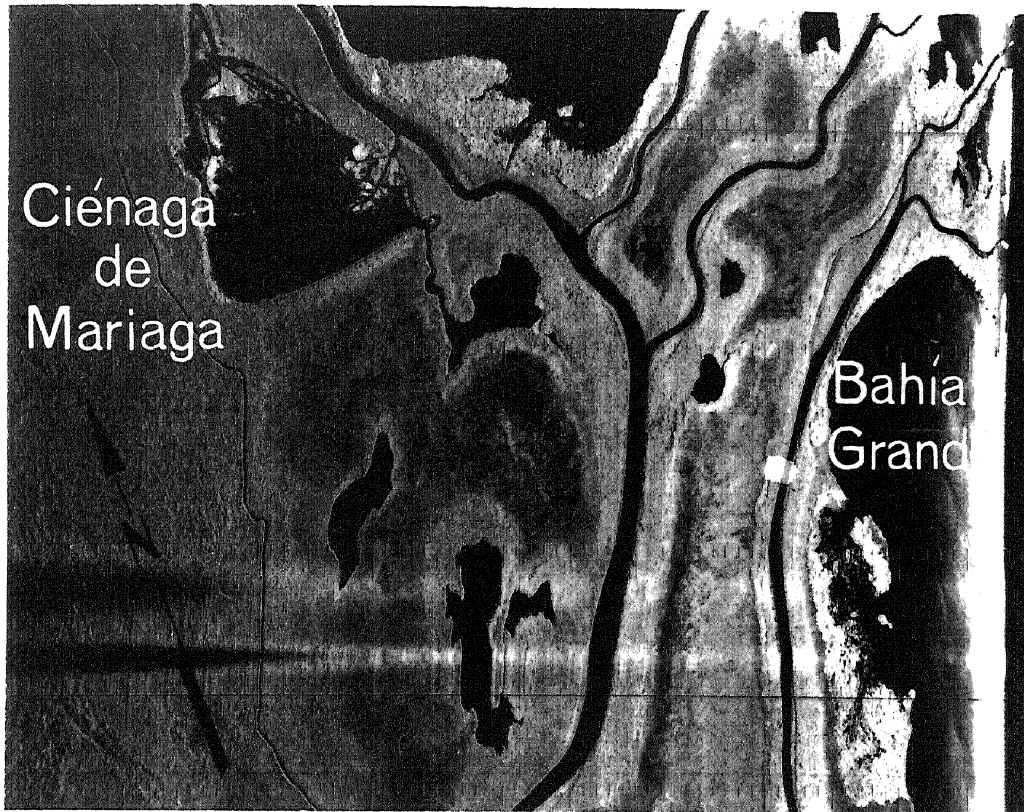


Figure 3.14 Vegetation patterns in the Atrato Delta on radar imagery and as mapped by Vann (1959).

levee and the back swamp basin (i.e., the lower back slopes of the levee and the margin of the basin); the grass and sedge community in the poorly drained back swamp basin; and, of less importance than the previous, the aquatic herbs on inactive point bars of abandoned or near-abandoned distributary channels.

"The chief significance of the vegetation of the Atrato Delta to the alluvial morphologist is its value as an indicator of terrain types. Everywhere mangrove occupies the mud flats of the tidal zone, the pangana community clothes the levees, the point bar assemblage marks areas of stagnant or weakly circulating fresh water and the grass and sedge and palm communities occur in the back swamps." (Vann, 1959, p. 358).

Isolated patches of the pangana community in the back swamps are indicators of stranded levees marking the course of former distributaries; whereas, interruptions of this community at right angles to the long axis of the levee indicates crevassing.

Another interesting feature on the Atrato Delta are the round lakes called "cienagas," which according to Vann (1959, p. 348) are responsible for the disproportionately low sediment load being carried by the Atrato River. Since nearly all of the upland tributaries must flow through these "cienagas" before reaching the Atrato, they in effect act as settling basins and reduce the sediment load of the Atrato. The deposition of this sediment has resulted in the formation of two small deltas in Cienaga de Mariaga (Figures 3.14 and 3.15), one at the normal inlet of the lake and the other at the natural outlet of the lake into the Atrato River. The outlet at the lower end of the cienaga is functional as an outlet only during the times that the river stage is lower than the lake level. When the river stage is higher than the lake level, such as at flood stage, the passageway becomes an inlet for the flooding waters which drop their sediment load upon entering the still water body forming a delta on the "wrong" side of the natural lake outlet. As the stage of the river drops, the water flows back into the Atrato River by way of this outlet; however, the velocity of the water as it flows over the delta is not high enough to rework the sediments and destroy the

delta. The result is the formation of a rather unique feature — a delta at the head of a lake outlet.

The detection of the position of the offshore river bar is also of importance to the alluvial morphologist since the relative distance of the bar from the mouth of the river provides information related directly to the relative velocity of each distributary and therefore the relative rate of sedimentation and importance of each distributary. As can be seen on Figure 3.15 of the Atrato Delta, the distance of the bar from the mouth of the corresponding distributary is greatest at Boca el Roto, followed by Boca de Barbacoas and Boca de Pavas, and finally at Boca de Tarena where the bar is almost even with the shoreline. This fits exactly with Vann's interpretation of the relative importance of these tributaries, that is, El Roto is the main distributary and Cano de Tarena is essentially an abandoned distributary slowly being invaded by the sea.

3.3.2 Coastal Features Outside of Panama

Other features, predominately coastal, observed by the author on radar imagery other than of Panama, are reported in MacDonald, Lewis, and Wing (1971). Some of these features include:

- (1) kelp beds and relative sea state offshore of San Diego, California;
- (2) beach ridges and vegetated foredune in the vicinity of Seaside, Oregon;
- (3) vegetated remnants of Pleistocene terraces, deflation basins between oblique sand dunes, and open, free moving sand north of the Umpqua River along the coast of Oregon;¹ and
- (4) chenier and an old meander scar along the Texas Gulf Coast.

3.3.3 Miscellaneous Features

Karst topography (Figure 3.16) is easily delimited on radar by its textural pattern exhibited on the imagery. Wing (1970) detected and mapped such geomorphic features as volcanic cones or plugs, calderas, dikes, and horsts and grabens in Eastern Panama from radar imagery.

¹Reported in Moore and Simonett (1967).

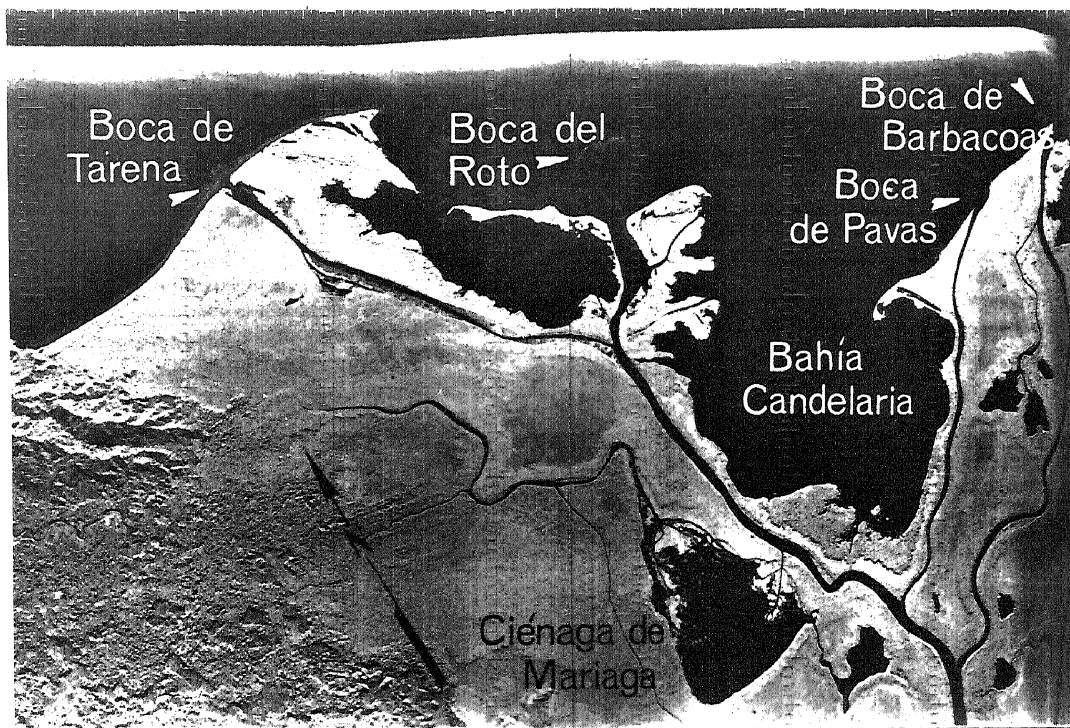


Figure 3.15 Radar imagery of Atrato Delta illustrating the detection of offshore river mouth bars.

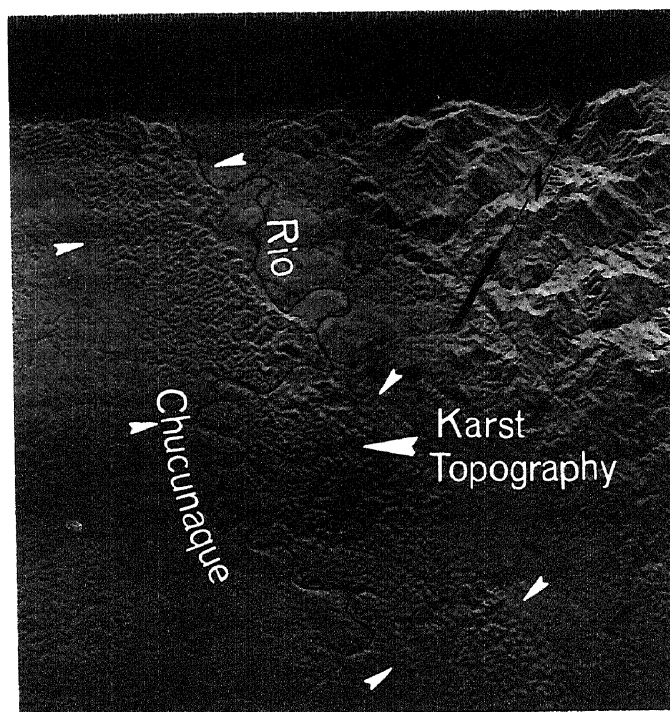


Figure 3.16 Radar imagery depicting Karst topography in Route 17.

Other features of interest to the alluvial geomorphologist that are detectable on radar imagery are meander scars, ox-bow lakes, and exposed point-bar deposits.

3.3.4 Drainage Basin Analysis

Detailed drainage nets are directly interpretable from radar imagery especially when four orthogonal look-directions are available for interpretation. As evidenced in Figure 3.17, the drainage net of the Rio Surcurti basin, compiled from five radar images of different overflights, compares favorably with the drainage net of the same area taken from maps of an approximate scale of 1:50,000 and a contour interval of 20 meters. Although most of the first-order streams and some of the second-order streams from the topographic map were not detectable on radar imagery, nearly all of the higher order streams were identically identified by both means. Direct comparison is not possible due to the inherent distortion in SLAR imagery. Many of the low-order streams not originally indicated on the topographic map, but inferred by the bending of contours up-valley, were not detectable on the radar imagery (MacDonald and Lewis, 1969 a and b).

Discrimination of streams, especially those of low-order, traversing flat, lowland areas such as mature flood plains and swamps or marshes, could at best be inferred. Using magnification of two to fifteen times, meander pattern segments are recognizable in the lowland areas. It should be mentioned that these low-order stream channels had little or no topographic expression, and the majority were shrouded under a canopy of vegetation.

In areas of karst topography or tuffaceous volcanics, the detectable drainage pattern is sparse and often sporadic. Drainage nets in regions of high relief are relatively easy to trace from radar imagery. Alternating high and low return from slopes oriented towards and away from the imaging system provides a feeling of depth and enhances topographic expression and discrimination of drainage nets. Caution should be used, however, if multiple look-direction imagery is not available and interpretations must be based solely on one look-direction. Past

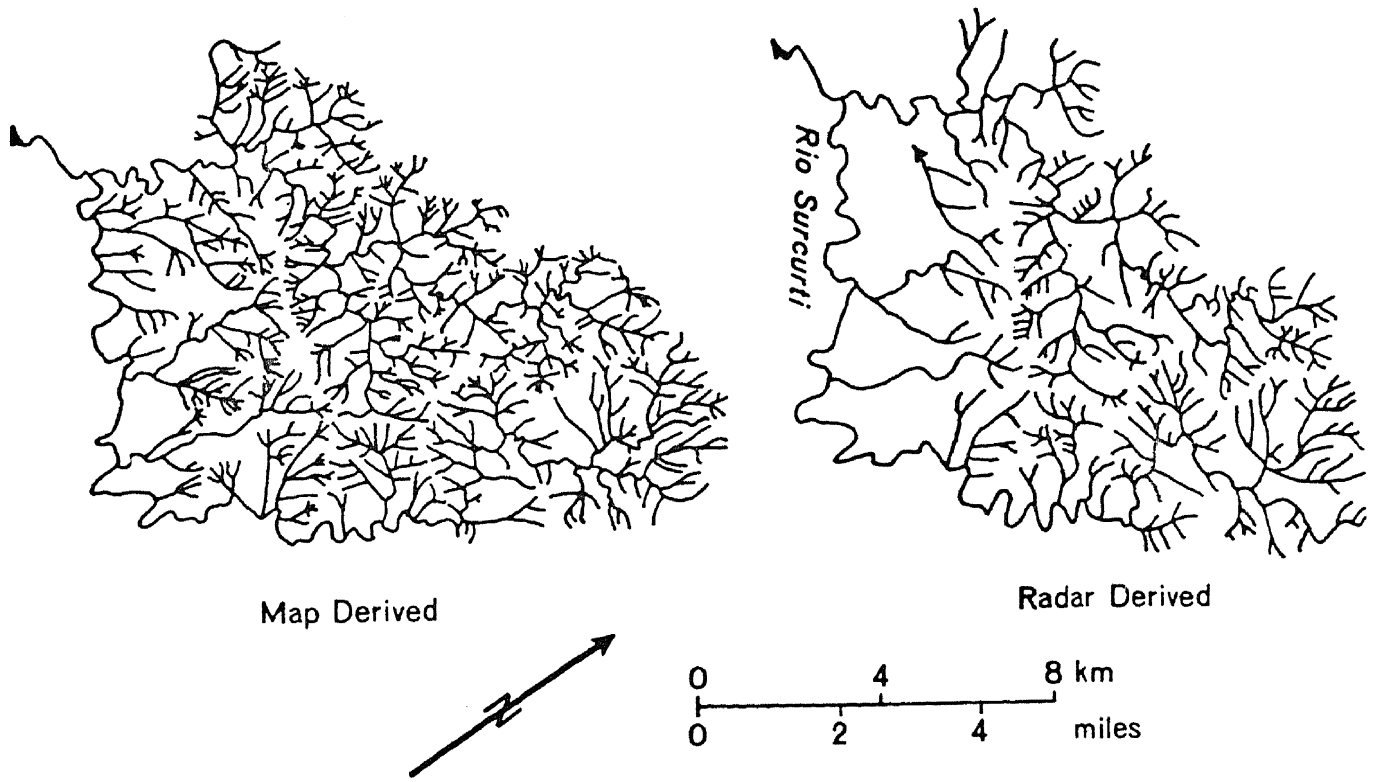


Figure 3.17 Map and radar derived drainage pattern of Rio Surcurti Basin in Route 17.

experience with mapping drainage from four orthogonal look-directions over the same area and comparing the results of each interpretation clearly indicates that the interpretations are not always congruous. The planimetric shape of the channel, the direction of flow, and the position of drainage divides can be misinterpreted on side-looking radar imagery if only a single pass is available for analysis.

The advantage of multiple passes is twofold: (1) to help delineate stream patterns and drainage divides more sharply where topographic expression is subdued and; (2) to provide a more complete drainage net where, due to high terrain relief and to the oblique imaging angles, the slope facing away from the sensor is obliterated by radar shadow.

Aside from outlining the drainage net, other commonly used parameters in drainage basin analysis are interpretable from radar with the same degree of confidence as those derived from topographic maps of a 1:24,000 scale. These parameters are drainage basin area, bifurcation ratio, average length ratio, circularity ratio, and basin perimeter (McCoy, 1967). With the above data available on radar imagery, detailed drainage basin analysis is feasible in cloud-shrouded, vegetal-covered tropical terrain where aerial photographic coverage is a monumental task and field work is time consuming and extremely difficult. Coupled with meteorological and climatological data, accurate flood forecasting could be possible.

Anomalous stream patterns, such as offset and deflection around a large subsurface dome, have been reported by MacDonald (1970), and stream piracy by Wing (1970) and Peterson (1968).

3.4 Summary

In summary, the type of geomorphic information available on radar imagery encompasses quite a broad spectrum ranging from the identification of individual features to regional data; from structural and tectonic information to hydrologic data; and from quantitative data to qualitative interpretations.

Large hard-to-map areas, such as the Darien Province, are especially suited for radar-oriented geomorphic studies, however, even in comparatively well areas radar imagery can provide geomorphic data as rapidly and reliable as topographic maps and aerial photographs.

CHAPTER 4

EVALUATION OF RADAR-DERIVED SLOPE DATA

4.1 Radar Foreshortening

4.1.1 Background

Dalke and McCoy (1969) were the first to derive a method utilizing radar foreshortening to calculate terrain slope (α). The method was then tested in a small area in southwestern Oregon for which overlapping imagery was available — a condition that must be satisfied before the method can be used. Thirty-five slope readings were taken from the radar imagery and compared to corresponding map data by running a simple linear correlation analysis on the two data sets. The range of terrain slopes tested was 10° to 35° , and all of the radar data was taken from overlapping radar imagery flown in opposite directions. The results revealed a very high correlation coefficient, $r = 0.99$, between the map- and radar-derived slope data.

The possibility of testing this method in a different type of environment (tropical), for a wider range of terrain slopes (0 to 35 degrees), and for a larger geographic area (over 3,000 square miles) with a larger number of observations (324 data points) became possible with the acquisition of radar imagery of the Darien Province including Route 17, a proposed inter-oceanic sea-level canal (Figure 1.1). Multiple imaging passes were also made allowing for the testing of both the equation that utilizes overlapping radar imagery with the same look direction (Equation 2.44) and the one for overlapping imagery taken from opposite look-directions (Equation 2.43). Because of the interest in this area as a possible site for a sea-level canal, topographic maps (Class B) had been prepared and were available at a scale of 1:50,000 and with a contour interval of 20 meters.

4.1.2 Methodology

The 324 data set used in this evaluation were selected from 24 different imaging passes available over the Route 17 area. For each data set two parameters, depression angle and slope length, had to be measured on each of two images flown in opposite- or same-look directions.

After identifying identical slopes on two radar images and the topographic map, the slope lengths were marked and labeled on frosted acetate. Depression angles were measured at the mid-point of the slope with a sliding scale constructed from interferometer data obtained from Westinghouse for the imaging system. Slope lengths were measured with a standard 60 units to an inch engineers rule. The data was recorded by sets and the look-direction indicated so that the proper equation could be used.

The nomograms provided by Dalke and McCoy (1969) were not used in lieu of the equations from which the nomograms were constructed, as this seemed to be the most accurate, rapid, unbiased method of calculating terrain slope angle for the 324 data set. After the terrain slope angles were calculated from radar-derived data, they were compared with map-derived slope angles by running a simple correlation and regression analysis on the two differently derived data sets. Prior to running the correlation-regression analysis, the data sets were divided according to look-direction in an attempt to determine which, if any, of the equations were more operational. After running the entire opposite and same look-direction data sets separately, each look-dependent set of data was subdivided into 5 classes according to the map-derived terrain slope values. Natural breaks in the frequency distribution of the data were used to establish the five classes in Table 4.1.

After running a linear correlation and regression analysis on the subdivided data sets, the classes in Table 4.1 were consolidated into only two groups, $0^\circ \leq \alpha < 9^\circ$ and $9^\circ \leq \alpha < 32^\circ$, in an attempt to increase the sample size and to provide more within-class variation in terrain slope angle (α), especially for Class I ($0^\circ \leq \alpha < 1^\circ$). This additional method of data manipulation provided more information for evaluating the radar foreshortening equation.

TABLE 4.1
 CLASSES USED TO SUBDIVIDE RADAR DERIVED SLOPE DATA
 FOR CORRELATION-REGRESSION ANALYSIS

Class	Terrain Slope Angle
I	$0^\circ < \alpha < 1^\circ$
II	$1^\circ \leq \alpha < 9^\circ$
III	$9^\circ \leq \alpha < 14^\circ$
IV	$14^\circ \leq \alpha < 18^\circ$
V	$18^\circ \leq \alpha < 32^\circ$

4.1.3 Results

Linear correlation and regression methods were employed (1) to analyze and describe the association between map-derived and radar-derived slope data; (2) to determine whether the equation that utilizes data from opposite-look or same-look imagery is more functional; (3) to determine at what range of terrain slope angles, if any, the foreshortening method is most reliable; and (4) to evaluate the accuracy of the foreshortening method for obtaining individual and regional slope values.

The results of the linear correlation and regression analysis indicated the following:

- (1) The opposite-look equation is more functional for determining terrain slope values (α) than is the same-look equation.
- (2) There is no definite range or class of terrain slope values (α) where the foreshortening method is more accurate for measuring α , although the radar- and map-derived α 's are more closely correlated where the map-derived α is $\geq 0^\circ$ but $\leq 9^\circ$.
- (3) The radar foreshortening method, as employed in this study, is not operational for determining individual slope values (α).
- (4) The mean regional slope and range of slope values (standard deviation) can be determined from radar foreshortening with a moderate degree of confidence providing a large enough sample is used.

The results of the statistical analysis are tabulated in Tables 4.2 to 4.7.

TABLE 4.2
CORRELATION AND REGRESSION ANALYSIS OF MAP-AND RADAR-DERIVED
TERRAIN SLOPE (α) DATA - OPPOSITE LOOK CONFIGURATION

Range of Terrain Slope from Maps	Number of Observations	Mean (Map Data)	Mean (Radar Data)	Standard Deviation (Maps)	Standard Deviation (Radar)	Correlation Coefficient (r)	Level of Significance	Standard Estimate of Error	Coefficient of Regression	Y-Intercept	Degrees of Freedom		F-Ratio	Level of Significance (F)
											Within	Between		
$0^\circ \leq \alpha < 32^\circ$	180	6.91		6.72		0.635	>.01	4.96	$0.605 \pm .05$	2.80 ± 5.12	1	178	120.13	>.001
			6.98		6.40									
$0^\circ \leq \alpha < 1^\circ$	74	0.014		0.049		0.091	<.1	2.56	-4.79 ± 6.16	2.71 ± 0.81	1	72	0.60	<.05
			2.64		2.55									
$1^\circ \leq \alpha < 9^\circ$	31	6.46		2.05		0.136	<.1	4.47	0.293 ± 0.40	5.06 ± 14.13	1	29	0.54	<.05
			6.95		4.44									
$9^\circ \leq \alpha < 14^\circ$	37	11.26		1.42		0.026	<.1	5.96	0.107 ± 0.70	8.67 ± 47.34	1	35	0.023	<.05
			9.87		5.88									
$14^\circ \leq \alpha < 18^\circ$	31	15.59		0.95		0.185	<.1	6.70	1.31 ± 1.29	-8.74 ± 110.27	1	29	1.03	<.05
			11.72		6.70									
$18^\circ \leq \alpha < 32^\circ$	7	20.46		1.43		0.834	>.02	6.10	-5.91 ± 1.75	137.58 ± 87.47	1	5	11.46	>.05
			16.74		10.10									

TABLE 4.3
 CORRELATION AND REGRESSION ANALYSIS OF MAP-AND RADAR-DERIVED
 TERRAIN SLOPE (α) DATA — OPPOSITE LOOK CONFIGURATION

Range of Terrain Slope from Maps	Number of Observations	Mean (Map Data)	Mean (Radar Data)	Standard Deviation (Maps)	Standard Deviation (Radar)	Correlation Coefficient (r)	Level of Significance	Standard Estimate of Error	Coefficient of Regression	Y-Intercept	Degrees of Freedom		F-Ratio	Level of Significance (F)
											Within	Between		
$0^\circ \leq \alpha < 9^\circ$	105	1.92	3.91	3.15	3.76	0.522	>.01	3.22	$0.622 \pm$ 0.10	$2.72 \pm$ 1.99	1	103	38.53	>.001
$9^\circ \leq \alpha < 32^\circ$	75	13.90	11.28	3.02	6.87	0.230	>.05	6.72	$0.503 \pm$ 0.24	$4.28 \pm$ 2.98	1	73	4.25	<.05

TABLE 4.4
CORRELATION AND REGRESSION ANALYSIS OF MAP-AND RADAR-DERIVED
TERRAIN SLOPE (α) DATA - SAME LOOK,
SLOPE FACING TOWARDS SENSOR CONFIGURATION

Range of Terrain Slope from Maps	Number of Observations	Mean (Map Data)	Mean (Radar Data)	Standard Deviation (Maps)	Standard Deviation (Radar)	Correlation Coefficient (r)	Level of Significance	Standard Estimate of Error	Coefficient of Regression	Y-intercept	Degrees of Freedom		F-Ratio	Level of Significance (F)
											Within	Between		
$0^\circ \leq \alpha < 32^\circ$	144	6.76	17.26	7.87	17.29	0.247	>.02	16.81	0.54 ± 0.18	13.60 ± 14.52	1	142	9.19	>.01
$0^\circ \leq \alpha < 1^\circ$	73	0.022	13.02	0.08	17.33	0.061	<.1	17.42	-13.64 ± 26.66	13.32 ± 5.31	1	71	0.26	<.05
$1^\circ \leq \alpha < 9^\circ$	14	6.30	21.43	2.33	7.29	0.330	<.1	7.15	1.03 ± 0.85	14.92 ± 19.47	1	12	1.77	<.05
$9^\circ \leq \alpha < 14^\circ$	26	11.78	20.07	1.37	16.58	0.064	<.1	16.89	0.77 ± 2.47	10.92 ± 145.50	1	24	0.10	<.05
$14^\circ \leq \alpha < 18^\circ$	17	15.97	21.03	1.04	20.81	0.049	<.1	21.47	0.99 ± 5.18	5.28 ± 330.61	1	15	0.04	<.05
$18^\circ \leq \alpha < 32^\circ$	14	21.89	25.37	2.77	16.86	0.092	<.1	17.47	-0.56 ± 1.75	35.58 ± 138.04	1	12	0.10	<.05

TABLE 4.5
CORRELATION AND REGRESSION ANALYSIS OF MAP-AND RADAR-DERIVED
TERRAIN SLOPE (α) DATA — SAME LOOK,
SLOPE FACING TOWARDS SENSOR CONFIGURATION

Range of Terrain Slope from Maps	Number of Observations	Mean (Map Data)	Mean (Radar Data)	Standard Deviation (Maps)	Standard Deviation (Radar)	Correlation Coefficient (r)	Level of Significance	Standard Estimate of Error	Coefficient of Regression	Y-Intercept	Degrees of Freedom		F-Ratio	Level of Significance (F)
											Within	Between		
0° < α < 9°	87	1.03		2.49		0.195	< .1	16.19	1.29+ 0.70-	13.05+ 6.93-	1	85	3.73	< .05
			14.38		16.41									
9° < α < 32°	57	15.51		4.43		0.108	< .1	17.87	0.44+ 0.54-	14.90+ 62.62-	1	55	0.65	< .05
			21.66		17.81									

TABLE 4.6

CORRELATION AND REGRESSION ANALYSIS OF MAP-AND RADAR-DERIVED
TERRAIN SLOPE (α) DATA - SAME LOOK,
SLOPE FACING AWAY FROM SENSOR CONFIGURATION

Range of Terrain Slope from Maps	Number of Observations	Mean (Map Data)	Mean (Radar Data)	Standard Deviation (Maps)	Standard Deviation (Radar)	Correlation Coefficient (r)	Level of Significance	Standard Estimate of Error	Coefficient of Regression	Y-Intercept	Degrees of Freedom		F-Ratio	Level of Significance (F)
											Within	Between		
$0^\circ < \alpha < 32^\circ$	51	12.52	24.07	4.46	19.81	0.346	>.02	18.78	1.54 ± 0.60	4.83 ± 52.73	1	49	6.67	>.05
$0^\circ < \alpha < 1^\circ$	0	Included in Same Look-Slope Towards since slopes <1° have no preferred orientation												
$1^\circ < \alpha < 9^\circ$	13	6.74	19.12	1.67	19.77	0.544	>.1	17.33	6.45 ± 3.00	-24.34 ± 70.29	1	11	4.61	<.05
$9^\circ < \alpha < 14^\circ$	16	11.57	12.22	1.44	9.00	0.283	<.1	8.93	1.77 ± 1.60	-8.23 ± 71.75	1	14	1.22	<.05
$14^\circ < \alpha < 18^\circ$	15	15.18	40.87	0.615	21.67	0.135	<.1	22.28	4.75 ± 9.68	-31.28 ± 549.9	1	13	0.241	<.05
$18^\circ < \alpha < 32^\circ$	7	19.75	24.33	0.963	7.70	0.008	<.1	F-Level Insufficient for further computation						

A combination of low correlation coefficients (r), high standard estimates of error, and low levels of significance strongly suggest that the radar-derived data is not highly or even moderately correlated with the map-derived data except for a few cases (Tables 4.2 to 4.7). The three most prominent exceptions are all related to the calculation of α with the opposite-look equation (Tables 4.2 and 4.3). The highest correlation coefficient (r) for the opposite-look data was for terrain slopes of $18^\circ \leq \alpha < 32^\circ$, where $r = 0.834$. Although the sample size was small ($N = 7$), the r was high enough to be significant at the .02 level. The next largest correlation coefficient was for the total opposite-look direction data set where $r = 0.635$. The highest level of significance was also experienced with this data set. The r was significant at 0.01 and the F-ratio at 0.001. Low to moderate standard estimates of error as well as close agreement between map-derived and radar-derived means and standard deviations for the entire data sets (Table 4.2) also lend support to the statistical significance of the data. This close agreement of the means and standard deviations for the map and radar slope data illustrates the usefulness of the method for obtaining both the mean slope values and the range of slope values on a regional basis.

The third highest correlation coefficient ($r = 0.522$) for a data set with a statistically significant F-ratio was where $0^\circ \leq \alpha < 9^\circ$ (Table 4.3). This data set is the result of combining the two lowest classes in Table 4.2. It is interesting to note the effect that this consolidation had on the statistical results, especially the correlation coefficients (Tables 4.2 and 4.3).¹ The large increase in r is in part explained by the direct relationship of r with the number of observations and the inverse relationship of r with the standard deviation of the data set, plus the possible occurrence that the data sets are homoscedastic, i.e., have equal standard deviations.

¹ Prior to combining the two classes $r = 0.091$ and 0.136 for slope classes $0^\circ \leq \alpha < 1^\circ$ and $1^\circ \leq \alpha < 9^\circ$, respectively; whereas, after combining the two classes to one, $0^\circ \leq \alpha < 9^\circ$, $r = 0.522$.

The total data sets for both the same look, slope towards and same look, slope away had correlation coefficients that were statistically significant; however, the practical significance is doubtful because of the large standard deviation and standard estimate of error around the regression equation for the data sets (Tables 4.4 and 4.6). The only other statistically significant correlation coefficient and F-ratio was for the same look, slope away, $9^\circ \leq \alpha < 32^\circ$ where $r = 0.348$; however, both the standard deviation and the standard estimate of error were nearly as large as the mean regional slope value (Table 4.7). Although the correlation coefficient was statistically significant ($r = 0.544$) for $1^\circ \leq \alpha < 9^\circ$, the F-ratio was too small to have statistical significance ($p < .05$) (Table 4.7).

4.1.4 Explanation and Limitations of Results

The discrepancy between Dalke and McCoy's results and the results of this study is analogous to the variation one usually encounters in results from a highly controlled experimental test of a small data set with those from a semi-controlled operational test of a large data set. Dalke and McCoy (1969) tested the method for (1) a relatively small area in Oregon, (2) only two strips of radar imagery from opposite-look directions, (3) only a relatively small range in map-derived slope values ($10^\circ \leq \alpha < 35^\circ$), and (4) only a relatively small sample set ($N = 35$); whereas, this study (1) tested a much larger area (Route 17); (2) utilized imagery with opposite-look and same-look configuration, and subdivided the same-look imagery into two possible classes: slope facing towards the sensor, and slope facing away from the sensor; (3) tested a larger range of slope values ($0^\circ \leq \alpha < 32^\circ$); and (4) employed a large sample set ($N > 300$).

Other sources of variation between the two studies and reasons for the low r values experienced in this study are (1) the large number of different imaging passes used for data collection (12), (2) the inaccuracy of the existing topographic maps of Route 17, (3) the difficulty in selecting identical points on two different images, especially when they are from opposite look directions, and (4) the difficulty in accurately measuring slope length (L_F) and depression angle (β).

The large number of imaging passes used to collect data in this study added variance to the results by introducing minor and major system malfunctions, especially for flights made several days to a week apart. For example, positioning of the radar image on the film strip varied over one-quarter of an inch between flights.¹

The topographic maps from which the map data was collected have a scale of 1:50,000 and a contour interval of 20 meters (66 feet). They were also Class B maps and therefore subject to error. Dalke and McCoy used more accurate maps with a larger scale (1:24,000) and smaller contour interval (40 feet).

MacDonald (1969), in trying to use radar foreshortening for measuring dip slopes, found identifying the base of the dip slope, as well as identifying identical points on the imagery to be exceedingly difficult, and after several inaccurate dip slope measurements he abandoned the method.

The difficulty in identifying identical points on two slopes and accurately measuring slope length and depression angle was realized by Dalke and McCoy (1969); however, they were unaware of the magnitude of the effect that slope length and depression angle have on the determination of terrain slope (α) under certain conditions. The effect is especially noticeable with the same-look equation.

Two examples of the effect of slope length and depression angle (β) on the calculation of α are given below:

Case 1

A. $L_1 = 0.083$ inches	Same-Look	Opposite-Look
$\beta_1 = 33.83^\circ$	Equation	Equation
$L_2 = 0.0913$ inches	Terrain Slope(α) 6.20°	0.99
$\beta_2 = 26.42^\circ$		

¹This is a function of the sweep-delay and radar altitude, and unless the two are synchronized the image will be mis-positioned on the film output. Since barometric pressure is used to determine altitude, errors can easily be experienced where atmospheric data is not available to allow for accurate corrections due to barometric pressure changes, such as in many parts of the tropics.

then vary L_1 by 0.017 inches

B. $L_1 = 0.10$ inches	Same-Look	Opposite-Look
$\beta_1 = 33.83^\circ$	Equation	Equation
$L_1 = 0.091$ inches	Terrain Slope(α)	
$\beta_1 = 26.42$	64.00°	7.99°

The variation in L_1 by only 0.017 inches changed the value for terrain slope over 57° for the same-look equation and 7° for the opposite-look equation. For both equations the variation in terrain slope was greater than a factor of 8.

Case 2

A. $L_1 = 0.058$ inches	Same-Look	Opposite-Look
$\beta_1 = 27.70^\circ$	Equation	Equation
$L_2 = 0.05$ inches	Terrain Slope(α)	
$\beta_2 = 29.00^\circ$	29.34°	1.66°

and then vary β_2 by 2°

B. $L_1 = 0.058$ inches	Same-Look	Opposite-Look
$\beta_1 = 27.70^\circ$	Equation	Equation
$L_2 = 0.05$ inches	Terrain Slope(α)	
$\beta_2 = 31.00^\circ$	53.09°	7.45°

In this case, by varying the depression angle by only two degrees, the terrain slope varied over 23° for the same-look equation and 5° for the opposite-look equation.

4.1.5 Recommendations

In order to make the radar foreshortening equation more operational and less volatile, more accurate methods of determining depression angle (β) and slope length (L) must be initiated. For more consistent depression angle (β) measurements from flight to flight, the exact position of the innermost depression angle (β) is needed to correct for positioning of the film on the CRT. Since the depression angle (β) measurement is in

essence the average depression angle measured at the mid-point of the slope, shorter slope lengths (L) will provide a more accurate determination of depression angle (β).

A more accurate and consistent method of measuring slope length is recommended based on the large variation in calculated terrain slope (α) that was encountered with a small change in slope length. This could be accomplished by implementing the use of a photo interpreter's 10 x magnifier with a .0005' reticle for the measuring of slope lengths directly from the radar imagery.

4.2 Radar Shadow Frequency

4.2.1 Background

In order to test the utilization of radar shadow frequency as a tool for producing cumulative frequency curves of a given landform region, several areas in the United States, where there is both topographic coverage and radar imagery, were selected. Table 4.8 lists the test areas and the scale, data, and contour interval of the topographic maps used. Most of the areas selected were mountainous regions with high terrain slopes since they were the most logical areas where the method would be used.

4.2.2 Methodology

Since the use of radar shadow frequency for producing a cumulative frequency slope curve had not been described or tested previously, a large amount of consideration had to be given to methodology. Since map-derived and radar-derived slope data were to be compared, two separate methods of data collection, from which cumulative frequency slope curves were the product, had to be established.

The method used for collecting map-derived slope data was a standard method described by Strahler (1956) whereby a regularly divided rectangular grid overlay was placed on the topographic map of the test

TABLE 4.8
 TEST AREAS FOR RADAR SHADOW FREQUENCY METHOD FOR
 DETERMINING CUMULATIVE FREQUENCY SLOPE CURVES

AREA	SCALE OF MAP (Date)	CONTOUR INTERVAL
Annamoriah, West Virginia	1:24,000 (1966)	20 ft.
Humbolt Range I, Nevada	1:62,500 (1956)	40 ft.
Humbolt Range II, Nevada	1:62,500 (1956)	40 ft.
Stansbury Mts., Utah	1:62,500 (1957)	20 ft - 40 ft
Chrome Ridge-Onion Mt., Oregon	1:62,500 (1961)	50 ft.
Seven Mile Peak, Oregon	1:62,500 (1960)	80 ft.

area and 100 samples were selected using a random numbers table to determine the x and y coordinates of the sample slopes. The slope angles were then computed by determining the elevation change from the contours (vertical distance) for a given horizontal distance orthogonal to the contours passing through the randomly selected sample point and with approximately equal distances falling upslope and downslope from the point. Although the horizontal distance was dependant upon the nature of the sampled slope, for example if the slope was very small or the selected sample point was close to the crestline, the "standard" horizontal distance used was 250 feet on either side of the sample point or a total of 500 horizontal feet.¹ On occasion, however, a 100 foot horizontal distance on either side of the sample was used.

Since there was no standard procedure for collecting cumulative frequency slope data from radar, the methodology evolved as the study progressed and different problems were encountered. The first problem encountered was the sampling procedure. Although a larger number of sampling zones across the image would increase the number of points for plotting the cumulative frequency curve; a smaller data sample for each point would result, and it was therefore decided that the best trade-off between a continuous source of data for plotting and a large enough sample to be significant was the division of the imagery into 8 areas of equal ground range. The use of zones of equal ground range was important as it provided zones of "potentially" equal sample size. The 8 zones were defined in terms of slant range depression angles² and an overlay prepared to help distinguish the zones and make the collection of radar data more practical.

¹The selection of the "standard" horizontal scale used was based on testing horizontal scales of different sizes (2640 ft., 1000 ft., and 500 ft.) in the Humbolt Mt. and the Chrome Ridge-Onion Mt. areas and it was found that the larger the horizontal scale size the greater the bias towards lower slope values due to averaging.

²The near range depression angle (β) boundary of each of the eight zones were 19°, 22°, 25°, 29°, 36°, 46°, 59°, and 78°, progressing from far to near range. These depression angles were determined mathematically.

The radar image was then enlarged photographically by a factor of two in order to reduce the percent error in measuring the length of the crestlines and shadows. The data were collected for each zone and categorized according to the orientation of the crestline and then, on the basis of the angle described by the orientation of the crestline with the flight line, the proper correction factor applied to the data.

The proper correction factor applied was determined by (1) the depression angle width of the zone, and (2) the magnitude of the error in degrees that is introduced by crestline orientation. In the four zones in the far range only two corrections were considered: (1) if the orientation of the crestline with the flight path (Θ) described an angle greater than 50° , the data was not used; and (2) if Θ was less than 50° , the data was used without correction. This decision was based on the 10° depression angle width of these four zones and an absolute error of around 10° when Θ is 50° (Figure 2.20). Three corrections were considered in the four zones in the near range: (1) if Θ was greater than 50° , the magnitude and change in error was too great and the data not used; (2) if Θ was between 30° and 50° , the sample was placed and tabulated with the data in the next zone closer to the near range; (This effectively added 3° to 5° to the back-slope angle of the sample which is in correspondence with the magnitude of the error involved.) (3) where Θ was less than 30° , the effect of Θ on the back-slope angle was less than the width (depression angle) of the sampling zone, therefore no correction factor was applied.

After the correction for crestline orientation was taken into account, the percentage of crestline length in shadow was calculated for each of the eight zones. Since the percentage of crestline length in shadow corresponds to the percentage of terrain back-slopes greater than the highest depression angle of the zone (Figure 2.17), the value was subtracted from 100 per cent to find the percentage of terrain back-slopes less than the highest depression angle of the zone. A smoothed cumulative frequency curve was then plotted on the basis of data from each of the eight zones across the radar imagery.¹

¹The map derived slope data was also plotted using the same eight zones used on the radar plot.

4.2.3 Results

A visual comparison of the map-and radar-derived cumulative frequency curves of terrain slope (α) indicates that in five of the six areas tested the cumulative frequency curves from radar shadow are representative of terrain slope distribution from topographic maps (Figures 4.1 to 4.6). It also appears that the correlation between map and radar derived cumulative frequency curves increases as the map detail increases, i.e., scale becomes larger and the contour interval smaller. This might be expected since the radar shadow frequency method favors the sampling of higher terrain slope angles more than the map method,¹ a phenomenon also encountered in map-derived data when (1) the map scale is increased, (2) the contour interval is decreased, or (3) the horizontal dimension of the slope length sampled is decreased.

Therefore, the sampling bias may, in fact, be in the map rather than radar-derived data. This seems to be apparent in Figure 4.4 where the radar-derived cumulative frequency curve appears more realistic (representative of the area) than the map-derived curve.² The curves in Figures 4.2, 4.3, and 4.5 also show that a greater proportion of the high slope angles ($> 25^\circ$) are sampled from radar imagery than from topographic maps. The reliability of the radar data in detecting the high slope angles is substantiated by radar geometry that prescribes that if the terrain back-slope angle is greater than the depression angle at which it is imaged radar shadow has to result. Therefore, a slope exhibiting radar shadowing at 60° depression angle must have a backslope greater than 60° . The sampling of this high angle slope is favored because the shadowed slope is more than likely part of a well-defined crest and as such a prime sampling source.

¹Especially evident in the terrain slope (depression) angles above 25° to 30° .

²By selecting and sampling, the individual slopes that were producing shadows in the near range, it was documented on the topographic maps that slope angles in excess of 50° are found in the region but were not sampled by using 100 random sample points.

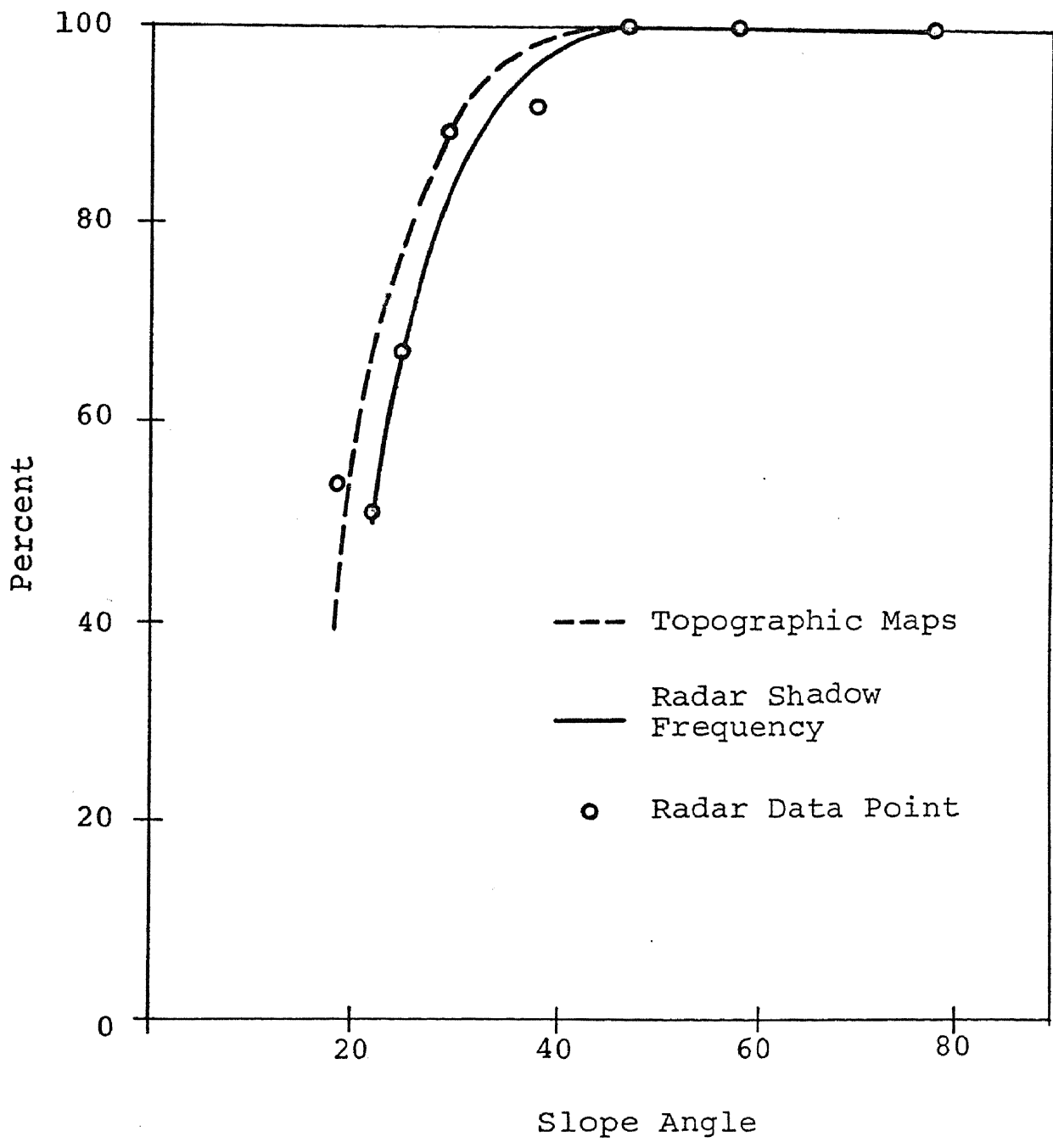


Figure 4.1 Cumulative Frequency Curves of Map-and Radar-Derived Terrain Slope (α) Data — Annamoriah, West Virginia

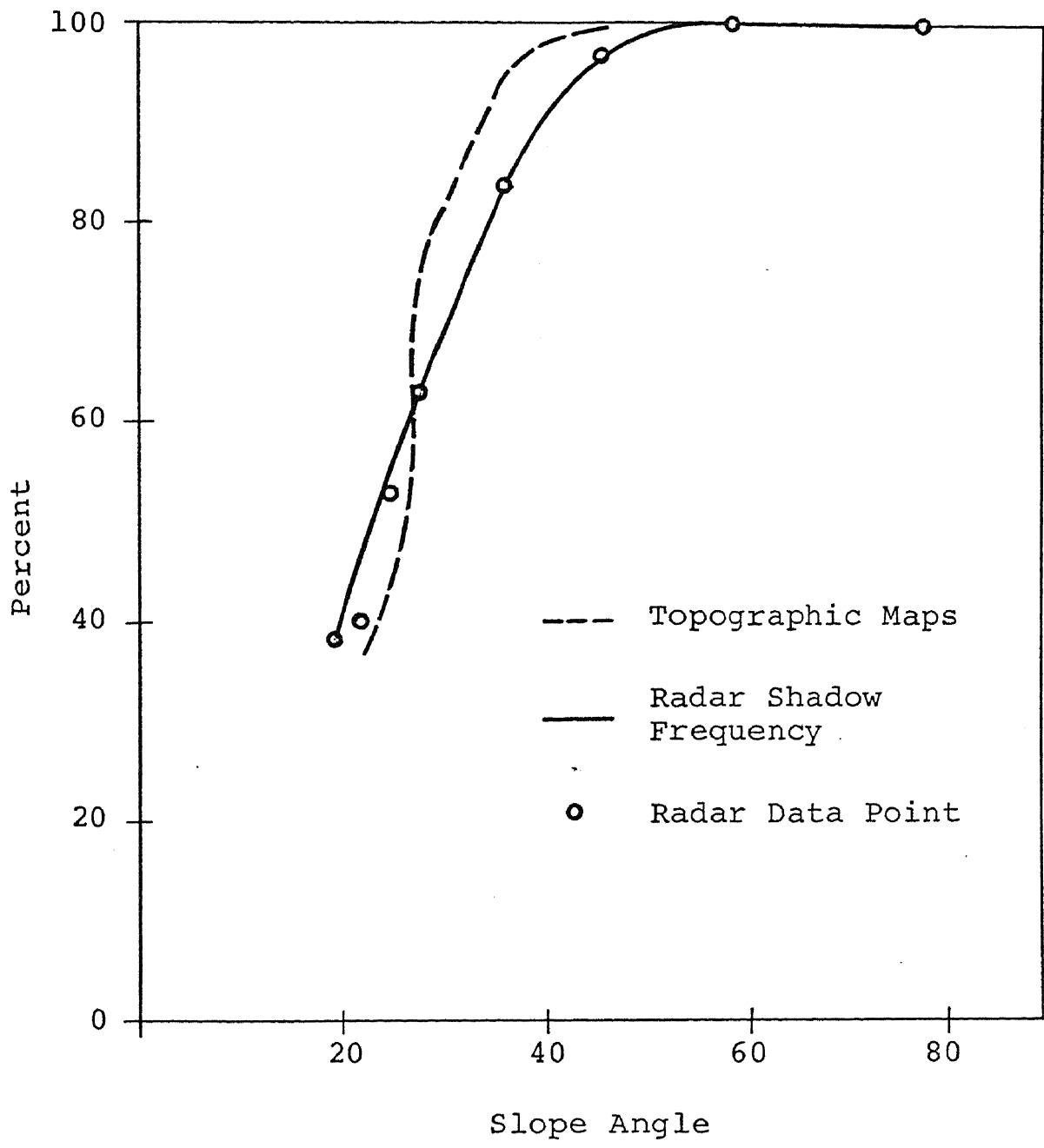


Figure 4.2 Cumulative Frequency Curves of Map-and Radar-Derived Terrain Slope (α) Data — Humbolt Range I, Nevada

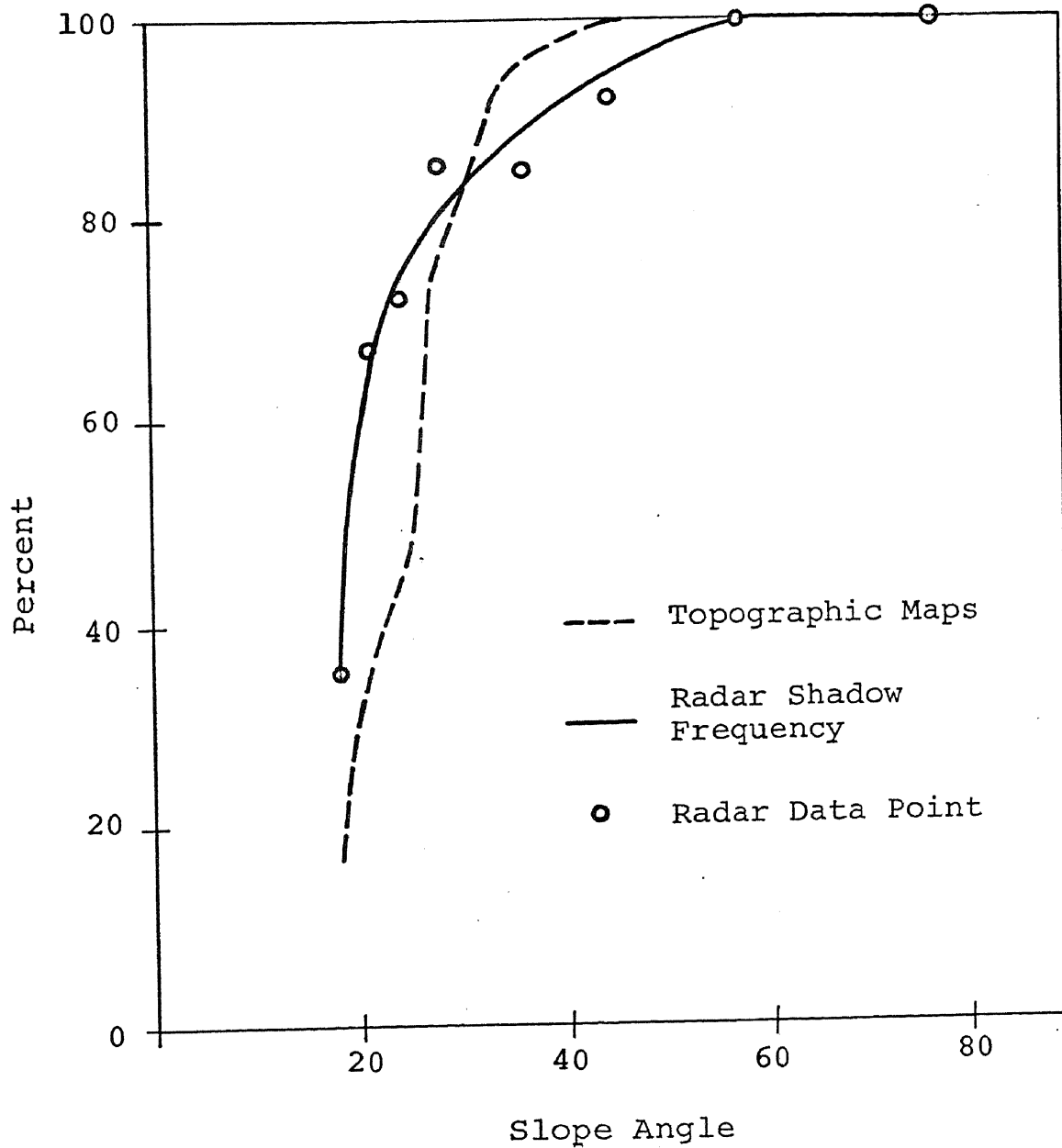


Figure 4.3 Cumulative Frequency Curves of Map-and Radar-Derived Terrain Slope (α) Data — Humbolt Range II, Nevada

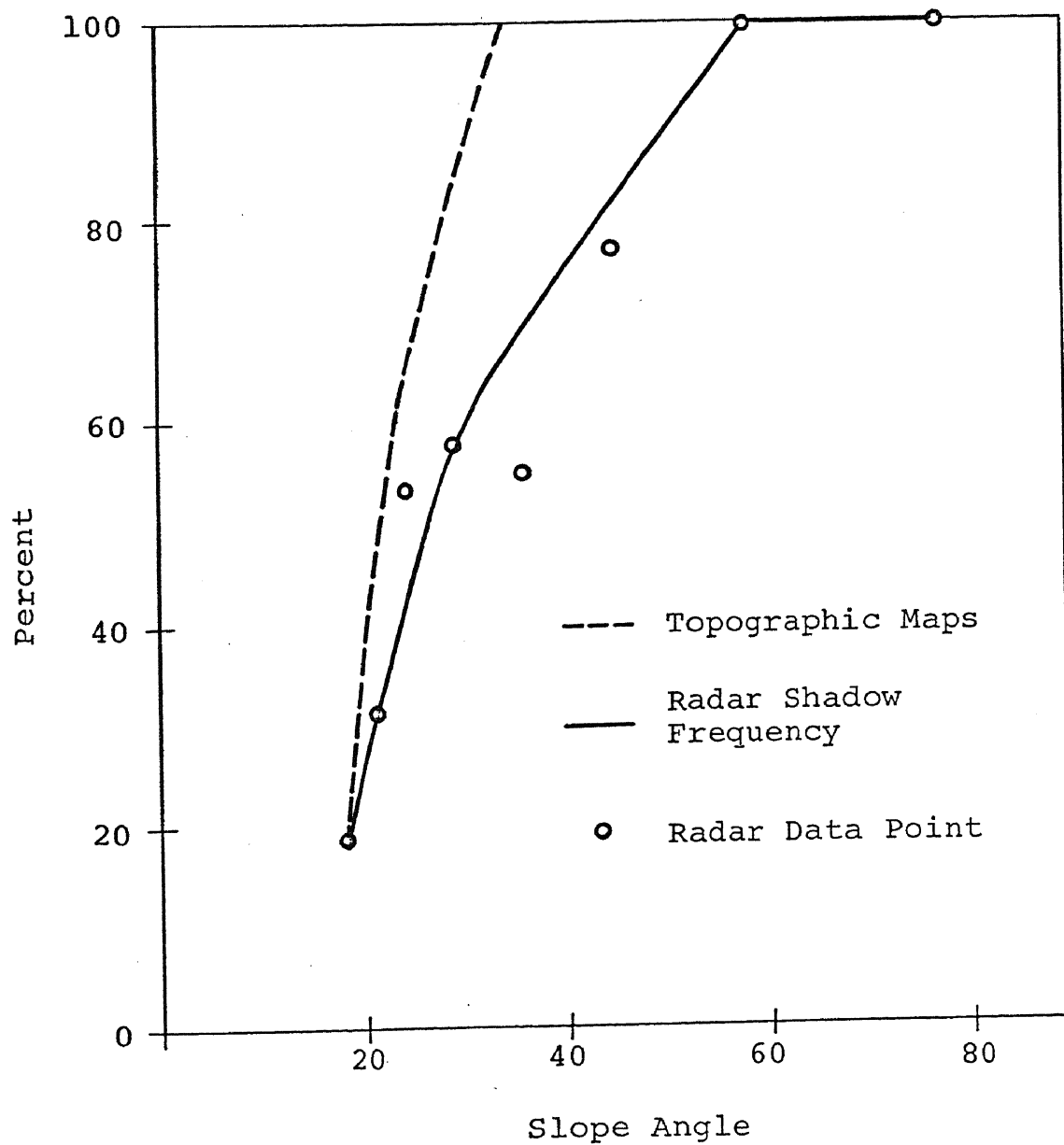


Figure 4.4 Cumulative Frequency Curves of Map-and Radar-Derived Terrain Slope (α) Data — Stansbury Mts., Utah

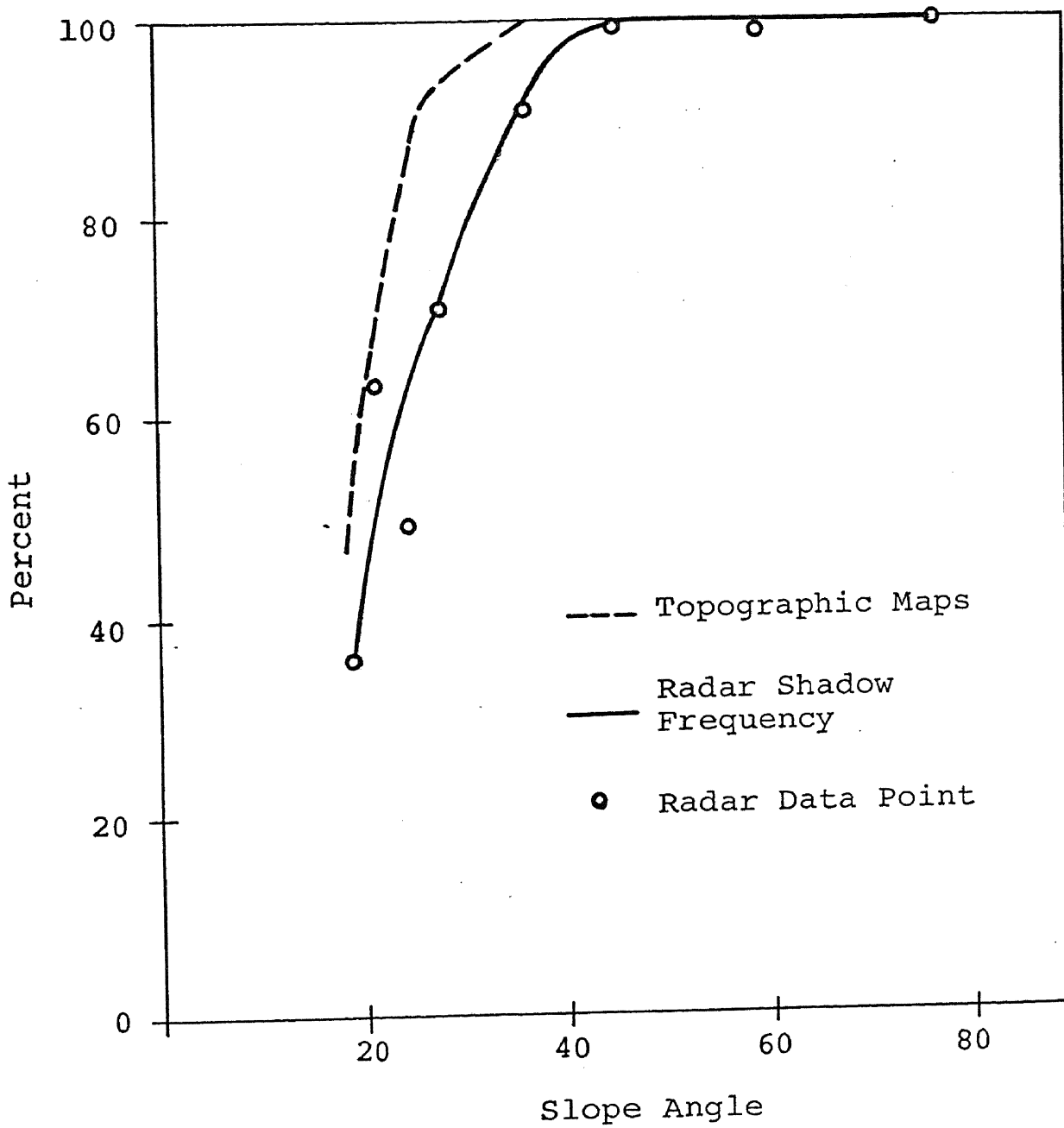


Figure 4.5 Cumulative Frequency Curves of Map-and Radar-Derived Terrain Slope (α) Data — Chrome Ridge-Onion Mtn., Oregon

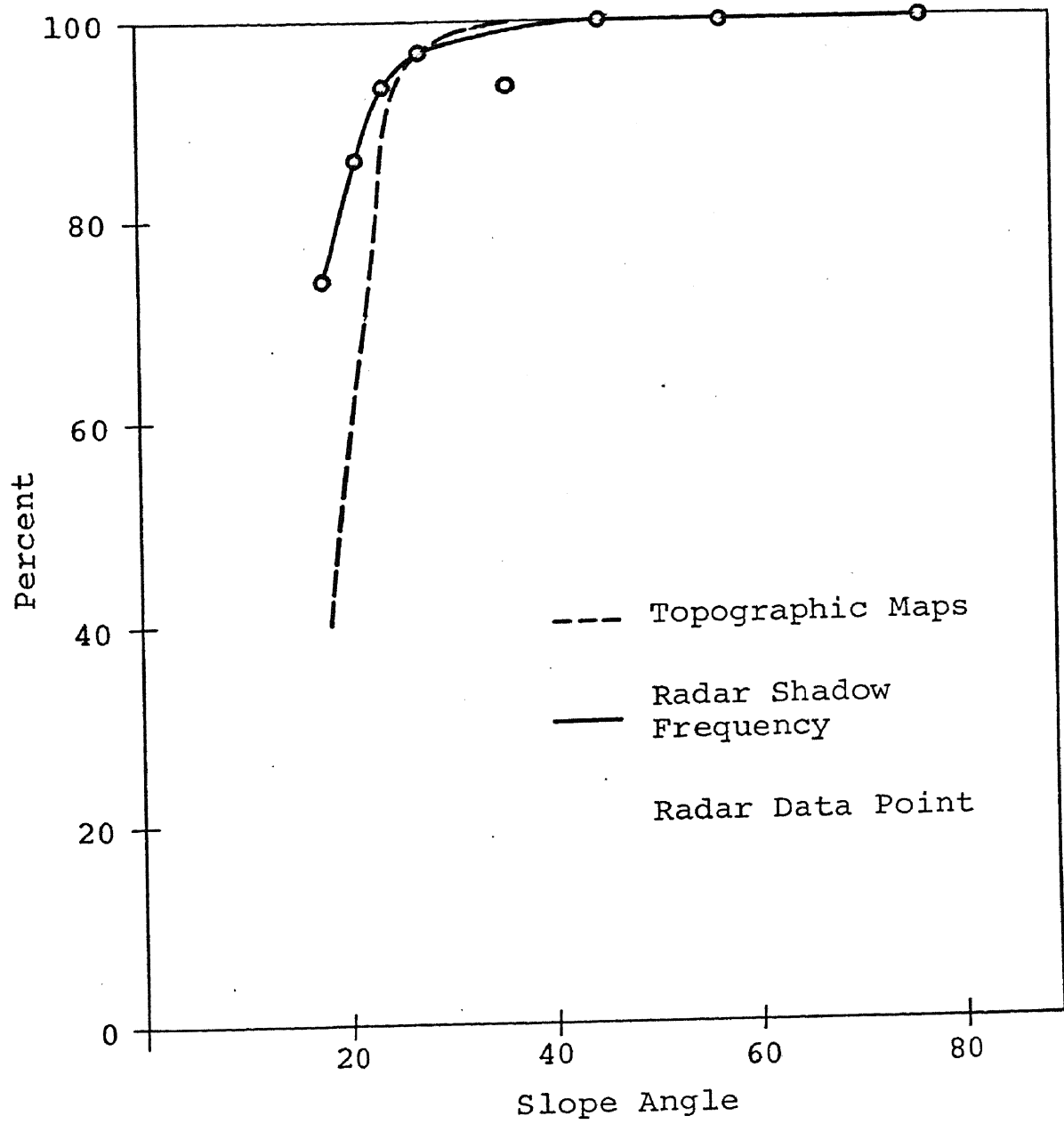
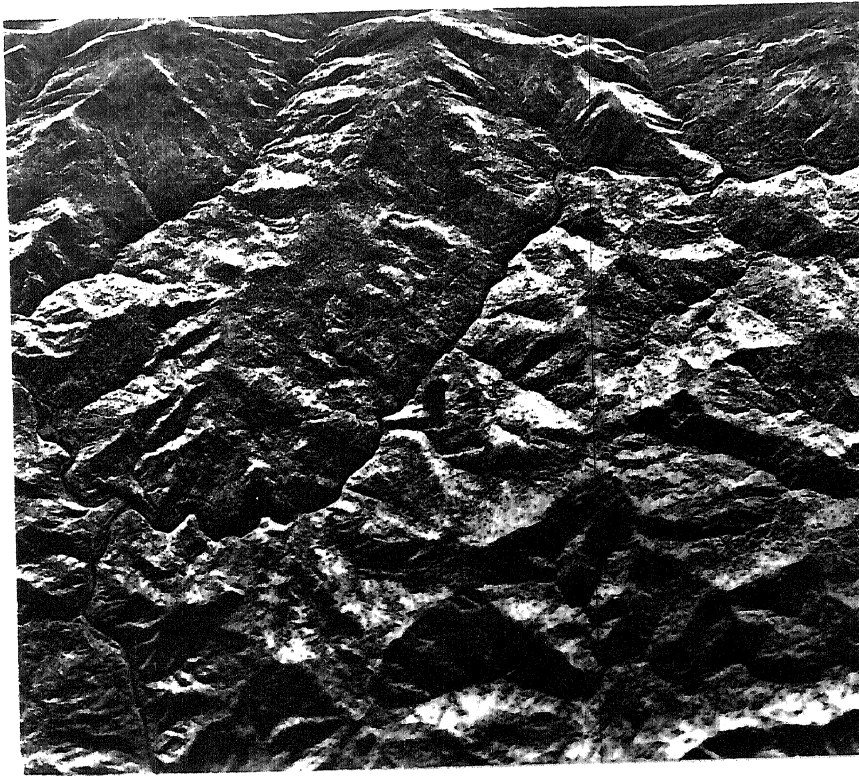
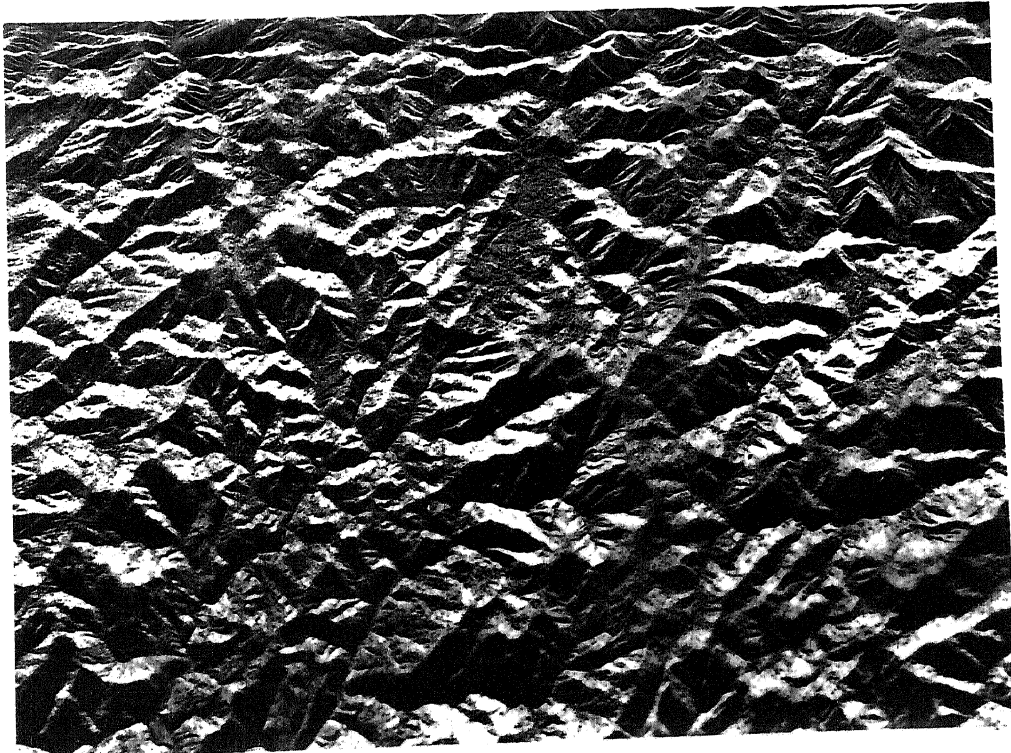


Figure 4.6 Cumulative Frequency Curves of Map-and Radar-Derived Terrain Slope (α) Data — Seven Mile Peak, Oregon



Seven Mile Peak, Ore.



Chrome Ridge-Onion Mt. Ore.

Figure 4.7 Radar Imagery of Seven Mile Peak and Chrome Ridge-Onion Mtn., Oregon. Seven Mile Peak area exhibits rounded, difficult to define crests; whereas the crests in the Chrome Ridge-Onion Mtn. area are knife-like, easy to define crests similar to the type of crests found in the other test areas.

regions, cumulative frequency curves of slope were prepared for each landform region on the two strips traversing the study area, and they are presented in Plates II and III.

Where the landform region did not extend completely across the image, two separate imaging flights were selected so that the area could be sampled across the entire range of the film. A comparison of the cumulative frequency curves based on the total sample set indicates, quite markedly, the variation of the distribution of slopes for each of the four landform classifications (Figures 4.8 through 4.11). The variation in the curves also lends confidence to the original qualitative delineation of landform regions. It is significant to point out that even the two regions that were delineated with the least confidence (High Hills and Mountains) resulted in landform regions that produced quite different cumulative frequency curves (Figures 4.10 and 4.11) where the curve for High Hills shows that 100 per cent of the slopes in the region were less than 45° ; whereas for Mountains, the curve indicated that slopes greater than 45° are found.

4.2.5 Advantages and Limitations of Radar Shadow Frequency Method

There are several advantages of using this method for producing cumulative frequency curves, and they are:

- (1) The method provides a more realistic cumulative frequency curve of slopes for areas of moderate to high slopes than topographic maps of a 1:62,500 scale.
- (2) Large areas can be sampled and a cumulative frequency curve plotted in less time and with more accuracy than with topographic maps utilizing standard sampling techniques.
- (3) The method works best in a mountainous type of terrain for which there is the poorest topographic coverage, and as such the radar-derived data provides a valuable complement to topographic maps.

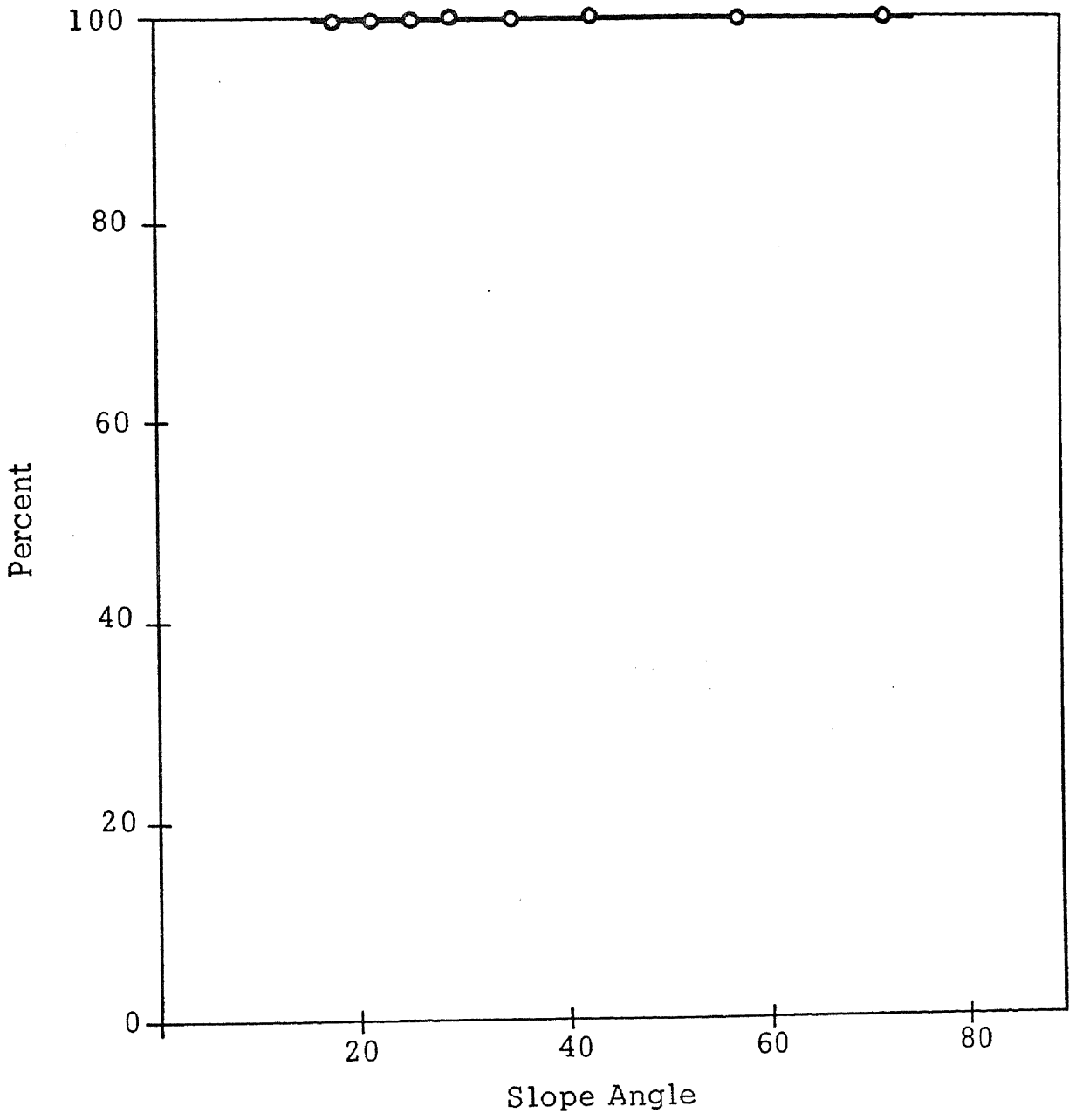


Figure 4.8 Cumulative Frequency Curves of Radar-Derived Terrain Slope (α) Data for Darien Province, Panama — Plains

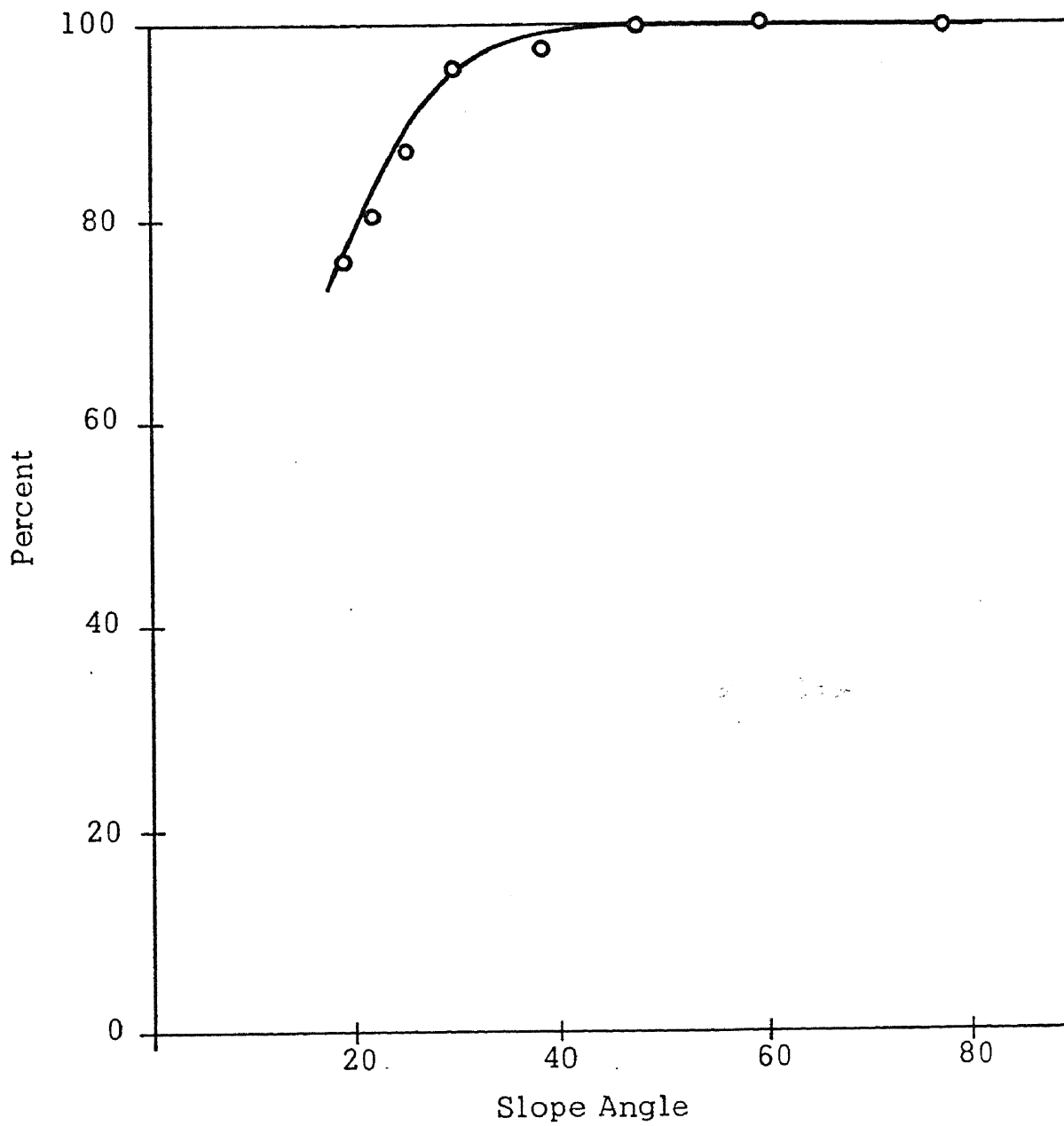


Figure 4.9 Cumulative Frequency Curves of Radar-Derived Terrain Slope (α) Data for Darien Province, Panama — Low Hills

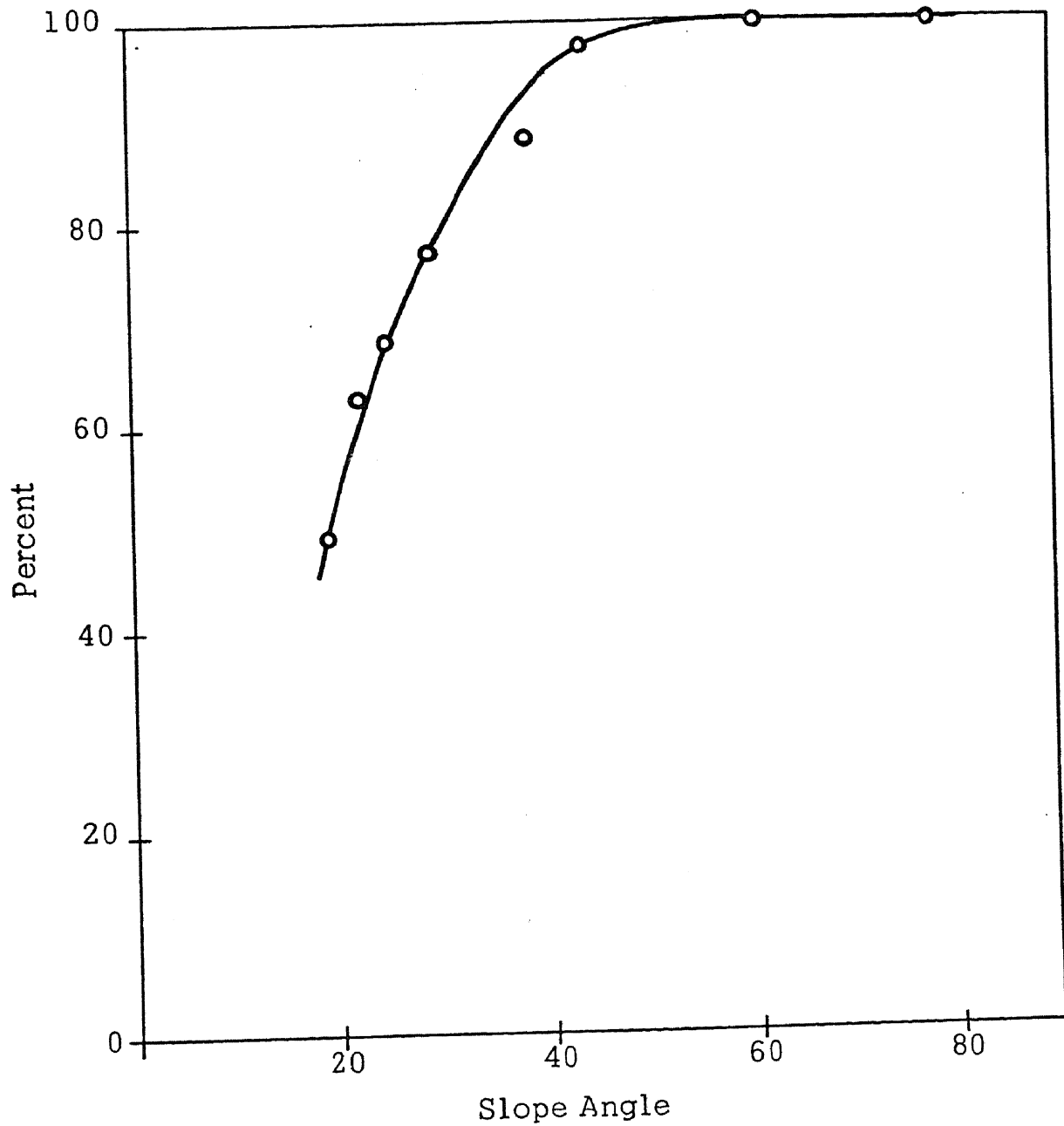


Figure 4.10 Cumulative Frequency Curves of Radar-Derived Terrain Slope (α) Data for Darien Province, Panama — High Hills

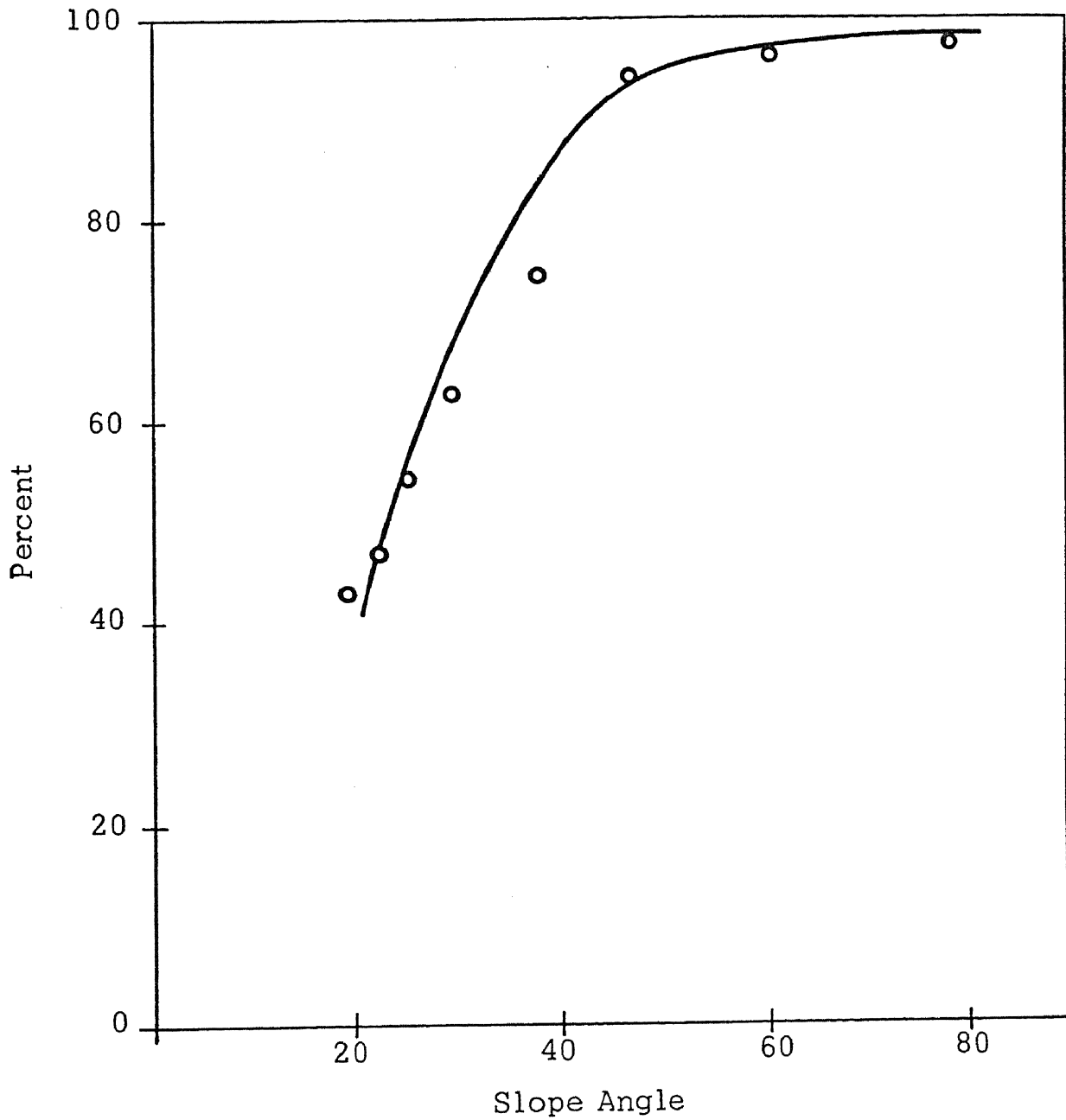


Figure 4.11 Cumulative Frequency Curves of Radar-Derived Terrain Slope (α) Data for Darien Province, Panama — Mountains

The limitations involved in using the method are:

- (1) For maximum data retrieval, the landform region must extend completely across the range of the image, or there must be enough multiple coverage of the region to provide a good sample. This means regions approximately 50 to 100 square miles in area.
- (2) The region must be homogeneous across the range and also have no preferred orientation of slope values. The assumption must be made, as previously mentioned, that the landforms are saw-toothed and the crestlines well defined.
- (3) The lowest slope value that can be discriminated is dependent on the far range depression angle of the radar imaging system, a value in the range of 15° . This means there is no discrimination of slope angles below approximately 15° . Since most of the critical slope angles for land use, terrain mobility, etc., are within the range of 0° to 15° , this is a serious limitation to the use of radar shadow frequency. This is a limitation of the imaging system rather than the method however, and could be corrected in part with system modification.

4.3 Radar Power Return

4.3.1 Background

The direct relationship between radar power return (P_r) and terrain slope (α) has been expressed previously in Equation 2.23. It follows from Equation 2.23 that $P_r = f(\alpha)$ when depression angle (β) is constant. And as mentioned in Section 2.4.1, P_r is directly related to the transmissivity (T) of the radar image, i.e., $T = f(P_r)$ and therefore $f = f(\alpha)$.

4.3.2 Methodology

Route 17 was used as the area to test the relationship between T and α . Fifty sites were selected from three separate imaging passes of Route 17 making sure that the slopes studied were perpendicular to the

flight path so apparent slope would not have to be considered. In order to make depression angle (β) a constant all of the sites selected were within a narrow band in the range, i.e., $22^\circ < \beta < 25^\circ$. Densitometer readings corresponding to transmissivity (T) were calculated from optical density values recorded on the densitometer. In order to assure good readings of 1 mm spot size was used and the final recorded reading was always the average of three or more readings depending on the dimensions of the slope on the radar imagery. Terrain slope angles were then calculated for the corresponding sites on the topographic map available for Route 17. A simple correlation program was then utilized to test the correlation between transmissivity (T) and terrain slope (α). The entire data set (N = 50) was tested for correlation and then the data set subdivided according to the individual imaging flight. This subdivision was done in an attempt to eliminate the variables encountered between different radar images, such as, power gain setting, and photographic and developing processes and to ascertain the effect, if any, on the correlation between T and α .

4.3.3 Results

The results are tabulated in Table 4.9.

TABLE 4.9
CORRELATION ANALYSIS OF RADAR POWER RETURN (P_r)
AND TOPOGRAPHIC-DERIVED TERRAIN SLOPE (α) OF ROUTE 17

Categories	Number of Observations	Correlation Coefficient (r)	Level of Significance (r)
Total Set ¹	50	0.365	>.01
Individual Sets ²	15	0.364	<.1
	19	0.538	>.02
	16	0.337	<.1

¹Combined data from three separate flights

²Separated data from three different flights

Although the correlation coefficient for the total set is high enough to be statistically significant at the 0.01 level, the correlation is too small ($r = 0.365$) for the geomorphologist concerned with relating transmissivity (T) to terrain slope to terrain slope (α). However, the results are encouraging and with further testing the correlation should increase.

The effect of the sample size (N) on the level of significance is readily seen in Table 4.9. For example, where $N = 50$ and $r = 0.365$ the r value is statistically significant at the 0.01 level; whereas, where $N = 15$ and $r = 0.364$, the r value is not statistically significant at the 0.1 level.

4.3.4 Explanation and Limitations of the Results

Although the results suggest that there is little correlation between terrain slope (α) and power return (P_r) in terms of transmissivity (T), they must be viewed in the context of the statistical analysis used, a simple (or linear) correlation program. It is quite plausible that:

- (1) if the densitometry data is rectified so that it more closely relates to radar power return; and
- (2) if a higher order polynomial equation is used instead of a linear equation the results of a correlation analysis would be more promising to the geomorphologist.

CHAPTER 5

EVALUATION OF RADAR-DERIVED RELATIVE RELIEF DATA

5.1 Radar Foreshortening

5.1.1 Background

Since using radar foreshortening to determine relative relief is an extension of the Dalke-McCoy method, the background and methodology presented in sections 4.1.1 and 4.1.2 concerning the collection of data and the calculation of α are relevant. Section 4.1.4 on the explanation and limitations of the results of calculating α using radar foreshortening is also pertinent and must be used as a background in the interpretation of the relative relief data from radar foreshortening.

5.1.2 Methodology

Even though the methodology for determining relative relief from radar foreshortening following the calculation of terrain slope (α) has been presented previously in section 2.6.2, a brief account is in order here. Although all of the data necessary to calculate relative relief from radar foreshortening were required and collected for the Dalke-McCoy method, the slant range length of the terrain slope (L_P) must be converted to the true length of the terrain slope on the ground (L).¹ Then utilizing equation 2.50 or 2.51, depending on whether the slope is facing towards or away from the sensor, relative relief was calculated and compared statistically to map-derived relative relief for association.

¹Determination of the necessary conversion factor is given in section 2.6.2.

The statistical method, a simple correlation and regression analysis, as well as the categories of image look direction configurations, slope orientations, and terrain slope were the same as those used in the evaluation of α calculated from radar foreshortening.

5.1.3 Results

The results from the correlation and regression analysis of the radar-derived relative relief data did not vary greatly from the statistical results of the radar-derived slope data. However, this was to be expected since relative relief is a function of terrain slope and in this case was calculated from terrain slope (α) derived from radar.

Small correlation coefficients, large standard estimates of error, and low levels of significance (Tables 5.1 to 5.8) combine to suggest that under the operational conditions used in this study, determining relative relief from radar foreshortening does not produce acceptable results. The major exceptions to the above are where the imaging configuration was either opposite look, slope towards; opposite look, slope away; or same look, slope away and the terrain slope category was $\alpha \geq 9^\circ$ (Tables 5.1 to 5.6). Even in several of these cases, even though all of the correlation coefficients and the F-ratios were large enough to be statistically significant, the data could not always be accepted without question, especially where high correlation coefficients ($r \geq .9$) and extremely high standard estimates of error were experienced with a small data set (<10 observations) (Tables 5.1, 5.3, and 5.5; $18^\circ \leq \alpha < 32^\circ$).

The main value, based on the statistical results, of measuring relative relief from radar foreshortening appears to be in measuring the mean and standard deviation of the regional relative relief where a large data set is available ($N \geq 100$) and the average relative relief is moderately high ($RR > 300$ feet). In these cases, statistically significant correlation coefficients along with standard estimates of error that are in line with the standard deviations from the map-derived relative relief data suggest that descriptive regional relative relief statistics from radar foreshortening can be used with confidence. This is especially true of the opposite

TABLE 5.1
CORRELATION AND REGRESSION ANALYSIS OF MAP-AND RADAR-DERIVED RELIEF DATA —
OPPOSITE LOOK, SLOPE FACING SENSOR CONFIGURATION

Range of Terrain Slope from Maps	Number of Observations	Mean (Map Data)	Mean (Radar Data)	Standard Deviation (Maps)	Standard Deviation (Radar)	Correlation Coefficient (r)	Level of Significance	Standard Estimate of Error	Coefficient of Regression	Y-Intercept	Degrees of Freedom		F-Ratio	Level of Significance (F)
											Within	Between		
$0^\circ < \alpha < 32^\circ$	180	331.21		333.78		0.356	>.01	368.52	$0.419 \pm .08$	255.33 ± 366.71	1	178	25.81	>.001
			394.18		393.23									
$0^\circ < \alpha < 1^\circ$	74	2.66		9.01		0.020	<.1	441.66	0.990 ± 5.73	299.663 ± 140.18	1	72	.030	<.05
			302.30		438.71									
$1^\circ < \alpha < 9^\circ$	31	416.88		174.41		0.148	<.1	254.93	$0.215 \pm .27$	332.99 ± 611.11	1	29	.651	<.05
			422.76		253.44									
$9^\circ < \alpha < 14^\circ$	37	676.74		223.96		0.644	>.01	338.58	$1.256 \pm .25$	-271.35 ± 1024.65	1	35	24.842	>.001
			578.52		436.53									
$14^\circ < \alpha < 18^\circ$	31	516.55		266.06		0.554	>.01	208.71	$.513 \pm .14$	64.80 ± 406.99	1	29	12.827	>.01
			329.75		246.44									
$18^\circ < \alpha < 32^\circ$	7	777.83		8.77		0.910	>.01	167.06	38.24 ± 7.78	29194.33 ± 14823.22	1	5	24.159	>.01
			550.03		368.28									

TABLE 5.2
CORRELATION AND REGRESSION ANALYSIS OF MAP-AND RADAR-DERIVED RELIEF DATA —
OPPOSITE LOOK, SLOPE FACING SENSOR CONFIGURATION

Range of Terrain Slope from Maps	Number of Observations	Mean (Map Data)	Mean (Radar Data)	Standard Deviation (Maps)	Standard Deviation (Radar)	Correlation Coefficient (r)	Level of Significance	Standard Estimate of Error	Coefficient of Regression	Y-Intercept	Degrees of Freedom		F-Ratio	Level of Significance (F)
											Within	Between		
0° < α < 9°	105	124.95		211.84		0.148	<.1	393.34	0.277+ .18	303.25+ 235.20	1	103	2.31	<.05
			337.86	395.82										
9° < α < 32°	75	619.96		248.10		0.596	>.01	305.69	0.909+ .14	-90.515+ 764.68	1	13	40.28	>.001
			473.03	378.21										

TABLE 5.3
CORRELATION AND REGRESSION ANALYSIS OF MAP-AND RADAR-DERIVED RELIEF DATA —
OPPOSITE LOOK, SLOPE FACING AWAY FROM SENSOR CONFIGURATION

Range of Terrain Slope from Maps	Number of Observations	Mean (Map Data)	Mean (Radar Data)	Standard Deviation (Maps)	Standard Deviation (Radar)	Correlation Coefficient (r)	Level of Significance	Standard Estimate of Error	Coefficient of Regression	Y-Intercept	Degrees of Freedom		F-Ratio	Level of Significance (F)
											Within	Between		
$0^\circ \leq \alpha < 32^\circ$	180	331.21		333.78		0.431	>.01	319.19	$0.456 \pm .07$	230.333 ± 317.63	1	178	40.620	>.001
			381.21		352.75									
$0^\circ \leq \alpha < 1^\circ$	74	2.66		9.01		0.051	<.1	336.04	1.905 ± 4.36	267.27 ± 106.66	1	72	0.191	<.05
			272.33		334.18									
$1^\circ \leq \alpha < 9^\circ$	31	416.88		174.41		0.149	<.1	257.34	$0.218 \pm .27$	329.05 ± 616.88	1	29	0.655	<.05
			419.91		255.85									
$9^\circ \leq \alpha < 14^\circ$	37	676.74		223.96		0.644	>.01	338.60	$1.256 \pm .25$	-271.527 ± 1024.70	1	35	24.847	>.001
			578.48		436.57									
$14^\circ \leq \alpha < 18^\circ$	31	516.55		266.06		0.552	>.01	209.68	$.513 \pm .15$	63.721 ± 408.88	1	29	12.725	>.01
			528.84		247.28									
$18^\circ \leq \alpha < 32^\circ$	7	777.83		8.77		0.910	>.01	167.07	38.241 ± 7.78	29194.63 ± 14823.95	1	5	24.157	>.01
			550.02		368.29									

TABLE 5.4

CORRELATION AND REGRESSION ANALYSIS OF MAP-AND RADAR-DERIVED RELIEF DATA —
 OPPOSITE LOOK, SLOPE FACING AWAY FROM SENSOR CONFIGURATION

Range of Terrain Slope from Maps	Number of Observations	Mean (Map Data)	Mean (Radar Data)	Standard Deviation (Maps)	Standard Deviation (Radar)	Correlation Coefficient (r)	Level of Significance	Standard Estimate of Error	Coefficient of Regression	Y-Intercept	Degrees of Freedom		F-Ratio	Level of Significance (F)
											Within	Between		
0° ≤ α < 9°	105	124.95		211.84		0.220	>.05	312.83	0.331+ 0.15-	274.52+ 187.05-	1	103	5.23	>.05
			315.90		319.13									
9° ≤ α < 32°	75	619.96		248.10		0.596	>.01	306.016	0.910+ 0.14-	-91.436+ 765.50-	1	13	40.268	>.001
			472.64		378.60									

TABLE 5.5
CORRELATION AND REGRESSION ANALYSIS OF MAP-AND RADAR-DERIVED RELIEF DATA --
SAME LOOK, SLOPE FACING AWAY FROM SENSOR CONFIGURATION

Range of Terrain Slope from Maps	Number of Observations	Mean (Map Data)	Mean (Radar Data)	Standard Deviation (Maps)	Standard Deviation (Radar)	Correlation Coefficient (r)	Level of Significance	Standard Estimate of Error	Coefficient of Regression	Y-Intercept	Degrees of Freedom		F-Ratio	Level of Significance (F)
											Within	Between		
$0^\circ \leq \alpha < 32^\circ$	51	505.76	780.12	209.48	624.82	0.337	>.02	594.191	$1.006 \pm .40$	271.418 ± 1437.03	1	49	6.287	<.05
$0^\circ \leq \alpha < 1^\circ$	0													
Included in Same Look-Slope Toward Since Slopes $< 1^\circ$ have no preferred orientation														
$1^\circ \leq \alpha < 9^\circ$	13	344.40	811.10	115.38	644.34	-.088	<.1	670.41	$-.489 \pm 1.68$	979.611 ± 2010.37	1	11	.085	<.05
$9^\circ \leq \alpha < 14^\circ$	16	613.77	600.27	178.91	584.37	0.599	>.02	484.592	$1.955 \pm .70$	-599.538 ± 16667.16	1	14	7.813	>.05
$14^\circ \leq \alpha < 18^\circ$	15	492.00	1013.17	211.06	707.41	0.624	>.02	573.961	$2.090 \pm .73$	-14.990 ± 1346.73	1	13	8.267	>.05
$18^\circ \leq \alpha < 32^\circ$	7	588.06	634.29	243.33	390.68	.966	>.01	110.054	$1.552 \pm .185$	-278.116 ± 269.74	1	5	70.611	>.001

TABLE 5.6
CORRELATION AND REGRESSION ANALYSIS OF MAP-AND RADAR-DERIVED RELIEF DATA —
SAME LOOK, SLOPE FACING AWAY FROM SENSOR CONFIGURATION

Range of Terrain Slope from Maps	Number of Observations	Mean (Map Data)	Mean (Radar Data)	Standard Deviation (Maps)	Standard Deviation (Radar)	Correlation Coefficient (r)	Level of Significance	Standard Estimate of Error	Coefficient of Regression	Y-Intercept	Degrees of Freedom		F-Ratio	Level of Significance (F)
											Within	Between		
0° α <math>< 9^\circ</math>	13	344.40		115.38		0.088	<.1	670.405	-0.489+ 1.68	979.611+ 2010.37	1	11	0.085	<.05
			811.10		644.34									
9° α <math>< 32^\circ</math>	38	560.97		206.65		0.495	>.01	515.746	1.501+ .44	-72.690+ 1500.47	1	36	11.700	>.01
			769.52		626.47									

TABLE 5.7
CORRELATION AND REGRESSION ANALYSIS OF MAP-AND RADAR-DERIVED RELIEF DATA —
SAME LOOK, SLOPE FACING SENSOR CONFIGURATION

Range of Terrain Slope from Maps	Number of Observations	Mean (Map Data)	Mean (Radar Data)	Standard Deviation (Maps)	Standard Deviation (Radar)	Correlation Coefficient (r)	Level of Significance	Standard Estimate of Error	Coefficient of Regression	Y-intercept	Degrees of Freedom		F-Ratio	Level of Significance (F)
											Within	Between		
0° < α < 32°	144	288.44		347.96		0.102	<.1	6967.536	2.050+ 1.67	-351.544+ 5804.85	1	142	1.499	<.05
			239.77		6979.68									
0° < α < 1°	73	2.965		10.023		.063	<.1	9575.138	59.790+ 112.59	-710.885+ 3049.44	1	71	.282	<.05
			-533.58		9527.28									
1° < α < 9°	14	382.35		196.27		0.412	<.1	1190.378	2.636+ 1.68	774.129+ 2342.38	1	12	2.456	<.05
			1782.06		1255.26									
9° < α < 14°	26	611.59		257.82		0.048	<.1	2737.604	.500+ 2.12	272.271+ 6517.17	1	12	.056	<.05
			578.59		2685.39									
14° < α < 18°	17	544.67		249.45		0.224	<.1	1260.672	1.124+ 1.26	-41.656+ 2770.70	1	15	.791	<.05
			570.48		1252.42									
18° < α < 32°	14	771.74		273.86		.383	<.1	1368.620	1.988+ 1.39	-228.154+ 3875.43	1	12	2.057	<.05
			1306.13		1423.19									

look configuration with the slope either towards or away from the sensor (Tables 5.1 and 5.3; $0^\circ < \alpha < 32^\circ$).

An overall evaluation of the correlation and regression analysis of the four imaging configurations strongly indicates that the most promising imaging configurations for obtaining relative relief data are opposite look, slope towards and opposite look, slope away (Tables 5.1 to 5.4); next is the same look, slope away imaging configuration (Tables 5.5 and 5.6); followed by same look, slope towards imaging configuration, a poor third (Tables 5.7 and 5.8).

5.1.4 Explanation and Limitations of Results

A source of error in this method that was not a consideration in the Dalke-McCoy method is the determination of the radar scale and therefore the accurate conversion of L_F to L . As can be seen in Equation 2.47, the determination of radar scale is related to both the near and far range depression angles and the aircraft altitude above the imaged terrain. Since the depression angles used are constant for a given imaging system, the major source of error encountered would stem from the determination of aircraft altitude. The flight logs report barometric altitude instead of radar altitude and as such do not compensate for either the passing of weather systems or the change in terrain elevation below the aircraft.

Another consideration as a source of error is that both equations for determining α from radar foreshortening (Equations 2.43 and 2.44) occasionally behave in a hyperbolic fashion and as such introduce a non-linear, bi-directional error that can be either compensated for or drastically magnified by an unrelated error in the measurement of L_F and subsequent conversion of L_F to L .

5.1.5 Recommendations

More accurate means of measuring L_F should increase the accuracy of the method as would the recording of radar altitude in the flight logs or on the imagery.

5.2 Radar Shadow

5.2.1 Background

The geometry, equations, and general assumptions for using radar shadows for determining relative relief were given in section 2.5.2, and the rationale for using Route 17 as a test area was presented in section 4.1.1. The total sample number was 51 and the range of relative relief was from 0.0 feet to 1164.4 feet.

Three equations were tested for association or correlation with relative relief data from maps; the first (Equation 2.30) was derived by Levine (1960), the second (Equation 2.33) by McAnerney (1966), and the third (Equation 2.32) by the author. Testing the three equations was carried out not only because measuring relative relief from radar shadows had not been evaluated previously as an operational method but also to determine which of the three equations, if any, most accurately determined relative relief under the conditions of the experiment.

5.2.2 Methodology

The parameters necessary for solving each of the three equations were measured on slant range imagery and then converted to true ground range. The radar measurements necessary for solving each of the three equations were taken from the same 51 sites so that the statistical results from each equation could be compared.

More details concerning what parameters were measured for each equation can be found in section 2.5.2.

5.2.3 Results

The high correlation coefficients ($r \approx 0.86$), small standard estimates of error ($SEE \approx 108$ feet), and high levels of significance ($P > .001$ for F-ratio and $> .01$ for r) strongly indicate that the measurement of relative relief can be effectively accomplished using radar shadows (see Table 5.9).

TABLE 5.9

CORRELATION AND REGRESSION ANALYSIS OF RELATIVE RELIEF DATA
 DERIVED FROM SAMPLING TOPOGRAPHIC MAPS AND FROM RADAR SHADOW METHODS

Source of Data	Number of Cases	Mean	Standard Deviation	Correlation Coefficient (r)	Level of Significance P	Standard Error of Estimate	Coefficient of Regression (b)	Y-Intercept	Degrees of Freedom		F-Ratio	Level of Significance F
									Within	Between		
Map Data	51	445.11	189.17									
Levine Method	51	452.2	205.59	0.864	>.01	105.15	0.95+ 0.079	28.86+ 247.85	1	49	145.03	>.001
McAnerney Method	51	450.22	207.13	0.864	>.01	104.48	0.94+ 0.078	34.13+ 246.29	1	49	144.59	>.001
Lewis Method	51	475.88	224.95	0.867	>.01	113.19	1.03+ 0.085	16.91+ 266.81	1	49	148.49	>.001

Although the statistics for all three equations are very similar, on the basis of the standard estimate of error (SEE), McAnerney's equations would rank first (SEE = 104.48 ft.), Levine's equation second (SEE = 105.15 ft.), and the author's equation third (SEE = 113.19 ft.). In all three cases the standard estimate of error is approximately one-half the standard deviation for the data set, an indication that the error factor is relatively small. In fact a statistical comparison was made of the standard estimates of error (SEE) that corresponded to each of the three equations. The criterion of likelihood (L) was calculated according to the method described by Croxton and Cowden (1940). The computed value for L was 1.00 which demonstrates that the three standard estimates of error are statistically identical. Since the author's equation requires fewer measurements for solving, it is deemed the most practical to use.

5.2.4 Explanation and Limitations of Results

Since all three of the equations for calculating relative relief from radar shadows are essentially based on the same geometry, the close agreement between the statistical results of the three equations was anticipated.

The high correlations, low standard estimates of error, and high levels of significance found in this test also helps to substantiate the evaluation of the radar foreshortening methods which involved collecting the identical or similar data from the same topographic maps and radar imagery.

5.2.5 Recommendations

The recommendations given in sections 4.1.5 and 5.1.5 relating to increasing the accuracy of measuring L , L_F , and β would also apply to the radar shadow method for determining relative relief.

CHAPTER 6

SUMMARY

6.1 Conclusions

The use of radar imagery for identifying individual landform features, inferring processes, delimiting geomorphic regions, and collecting qualitative and quantitative geomorphic data is a relatively new innovation to the field of geomorphology. Radar as a tool for the geomorphologist has several advantages. It has the ability to scan a broad band of terrain with a single pass, presenting the imaged area on a continuous strip of film. Although the resolution of the radar imagery employed is less than that of aerial photographs, the detail provided on radar imagery of a given scale is greater than that on a map of a comparable scale. The reduction of excessive detail, when combined with the synoptic view of radar also aids in the discrimination of geomorphic regions. Radar imaging systems therefore provide a means of gathering data from regional size areas allowing both generalization of large areas and identification of individual features. Near all-weather, 24-hour, imaging capability of radar is of special importance for studies of tropical regions so frequently masked by cloud-cover.

The large ratio of radar return from land and water — primarily a function of surface roughness — provides a striking interface which is extremely advantageous for delineating and mapping the coastline configuration as well as updating hydrographic charts and maps. This high dependence of radar return on surface roughness also aids in the detection of many other landform features associated with the land-water interface. Several of the features are tidal flats, barrier reefs, shell reefs, estuarine meanders, cienagas (round lakes), and kelp beds.

Within the near-shore and off-shore zones, wave refraction, sea state, surf zones, and river-mouth bars have been identified on radar imagery. Landward of the coastline, mangrove and associated non-vegetated areas, beach ridges, levees, crevasses, meander scars, and other features have also been detected.

Karst topography is also easily delineated on radar imagery when topographically expressed. Volcanic cones, dikes, calderas and other geologically important features have been detected and mapped from radar imagery of Panama.

Radar-derived drainage nets compare favorably with drainage nets from maps with a scale at 1:50,000 and contour intervals of 20 meters. Low order streams with little or no topographic expression are not identifiable. In karst areas drainage patterns are difficult to detect. Drainage nets are easily delineated in regions of high relief; however, caution should be used if multiple look direction imagery is not available and part of the drainage pattern is obscured by radar shadows.

Anomalous stream patterns vital to geological interpretations of the sub-surface, as well as stream piracy, have also been interpreted from radar imagery of Panama.

Although the detecting and mapping of geomorphic features is in itself important to geomorphic investigations of relatively unknown areas, the real importance of such interpretations is the additional information relating to geologic, geomorphic, and hydrologic processes involved in the past or active in the present. The use of geomorphic features as surrogates for obtaining genetic and environmental information has been illustrated throughout the study; however, several warrant reiteration. For example, mangrove coasts, non-vegetated areas behind mangrove coasts, tidal flats, and estuarine meanders provide tidal information for the area; the orientation of the shell bars indicates the near-shore circulation pattern; the presence of coral indicates the amount of suspended sediment and temperature-salinity properties of the water; and the relative distance of the river mouth bar strongly suggests the relative importance of delta distributaries.

Drainage pattern anomalies and volcanic and structural geomorphic features identified on radar suggest areas worthy of further geological exploration. Additional information regarding the energy environment, landform classification, climate, stream flow, etc. relating to specific geomorphic features were given in the study.

The major geomorphic regions derived using apparent relief and textural appearance on radar imagery of Route 17 compared favorably with those from topographic maps. Using the same criteria as in Route 17, a map of the regional geomorphology of the entire Darien Province and part of Colombia was compiled from radar imagery. The radar method of discriminating landform regions, although entirely qualitative, is more efficient and apparently just as accurate as the map method.

Statistical analysis of the terrain slope measurements (α) from radar foreshortening indicated that the method as tested is not operational for determining individual slope values; however, the accurate calculation of mean regional slope and the range of slope values is feasible using radar foreshortening. Although the opposite look direction equation, because of its behavioral characteristics, is more functional for calculating α than the same look equation, neither equation exhibited any definite range of map-derived terrain slope values where the calculation of α was significantly more accurate than any other range tested.

The linear relationship between radar power return (P_r) and terrain slope (α) was statistically significant for the total data set; however, it was much too low to be of any value to the geomorphologist without further testing with a higher order polynomial equation.

Cumulative frequency slope curves from radar shadowing correlate well with similar curves derived from topographic maps. The correlation between the map-derived and the radar-derived curves increases as the map scale increases and the contour interval decreases. This method appears to apply best in areas of high relief and high slope angles where the accuracy or even the existence of topographic maps diminishes. When extended into the Darien Province of Panama, the cumulative frequency curves from the radar shadow method resulted in four distinct

cumulative frequency curves , one for each general landform region previously discriminated qualitatively. This lends support to the reliability of both the qualitative methods employed in the construction of the landform map and the radar shadow method for constructing cumulative frequency slope curves .

The determination of relative relief from radar foreshortening is as feasible as calculating terrain slope from the same radar characteristic. With the improvement of the data collection techniques and more control and knowledge of flight parameters , both terrain slope and relative relief could probably be measured with an acceptable level of consistency and reliability .

The statistical correlation between map-derived and radar shadow derived relative relief values was very good. The other results of the statistical analysis also indicated that the relative relief can be determined accurately and reliably from radar shadows . Three equations that use radar-derived shadow data were evaluated , and the statistical results for all three equations were remarkably close . On the basis of the standard estimate of error , McAnerney's equation was ranked as first , followed by Levine's equation and then the author's equation . The standard estimates of error are so close that statistically there is no difference between the equations ; however based on the number of parameters that need to be measured for solving the equations , the author's equation is judged the easiest to use .

6.2 Recommended Future Work

The documentation of the value of radar imagery in geomorphic investigations has barely been initiated in this and previous studies (Barr , 1968; Beatty , et al. , 1965; Feder , 1960; McAnerney , 1966; McCoy , 1967; and Wing , 1970) . Direct and indirect relationships between radar-derived information and corroborative data must be worked out . For example , the practicality of using shoreline geometry and other radar-derived information to classify coastal environments , descriptively and genetically , should be studied .

Several interesting studies using cross power spectrum techniques with radar data would be to correlate:

1. shoreline or river meander geometry derived from maps with the same information taken from radar imagery;
2. radar shoreline geometry with the direction, frequency, and strength of on-shore winds, and the fetch of wind waves;
3. radar river meander geometry with channel slope, lithology, average and maximum flow, and flood frequency; and
4. dune orientation from radar with the resultant on-shore winds.

Following the implementation of several of the recommendations made regarding more accurate collection of radar data, such as in the measurement of slope length and depression angle, the use of radar foreshortening to calculate terrain slope and relative relief should be re-evaluated. Further testing of the consistency of relative relief from radar shadows should be undertaken.

Radar shadow frequency as a discriminate of cumulative frequency curves also needs further testing of reliability in different types of landform environments.

The use of radar shadow area as an indicator of both topographic texture and relative relief has never been documented although the relationship appears to be a natural one.

The feasibility of utilizing radar scatterometry data for determining low terrain slope angles from relative power return warrants investigation as an accurate means of determining slope angles less than 10° . This would be an extremely valuable supplement to the slope data derived from radar imagery using other methods.

The use of radar power return as a surrogate to terrain slope angle is a very exciting possibility. The testing with higher order polynomial equations, as well as, rectifying the densitometry readings so that they are more closely related to radar power return has not been accomplished to date. Further studies relating terrain slope to power return should also test the correlation at various depression angles.

Further documentation into the value of radar geomorphology is paramount, and pending the completion of such documentation, the true worth of radar imagery to the geomorphologist can only be speculated.

BIBLIOGRAPHY

- Ahnert, Frank, 1960, "Estuarine Meanders in the Chesapeake Bay Area," Geographic Review, vol. 50, no. 3, pp. 390-401.
- Ahnert, Frank, 1963, "Distribution of Estuarine Meanders," Final Report Project NR 388-069, Contract Nonr (G)-0048-62, Office of Naval Research, 69 pp.
- Bakhtina, I. and E. Smirnova, 1968, "Methods for Estimating the Suitability of Natural Conditions at Various Stages in the Drawing Eye of Architectural Plans," In: Land Evaluation G. A. Stewart, ed., MacMillan of Australia, pp. 179-186.
- Barr, D. J., 1968, "Use of Side-Looking Airborne Radar Imagery for Engineering Soil Studies," Final Technical Report for Contract DA-44-009-AMC-1847(x), Geographic Sciences Division, U. S. Army Engineer Topographic Laboratories, Fort Belvoir, Virginia, 193 p.
- Beatty, F. D., and others, 1965, Geoscience Potentials of Side-Looking Radar, Raytheon Autometric Corp., Alexandria, Virginia, 90 p.
- Chorley, J., 1957, "Climate and Morphometry," Journal of Geology, vol. 65, no. 11, pp. 628-638.
- Coleman, J. M., 1966, "Recent Coastal Sedimentation: Central Louisiana Coast," Coastal Studies Institute Technical Report No. 29, Louisiana State University Press, Baton Rouge, 73 pp.
- Cosgriff, R. L., W. H. Peake, and R. C. Taylor, 1960, "Terrain Scattering Properties for Sensor System Design (Terrain Handbook II)," Engineering Experiment Station Bulletin No. 181, Ohio State University Press, Columbus, Ohio, 117 pp.
- Croxton, F. E. and D. J. Cowden, 1940, Applied General Statistics, Prentice-Hall, Inc., 944 pp.
- Dalke, G. W. and R. M. McCoy, 1969, "Regional Slopes with Non-Stereo Radar," Photogrammetric Engineering, vol. 35, no. 5, pp. 446-452.
- Dudley, Wm. W., 1966, "Geomorphic Analysis of Route 17," IOCS Memorandum NCG-202-17 Serial No. NCG-11, 32 pp.
- Feder, A. M., 1960, "Interpreting Natural Terrain from Radar Displays," Photogrammetric Engineering, vol. 26, no. 4, pp. 618-630.

- Fosberg, F. R., 1961, "Vegetation-Free Zone on Dry Mangrove Coasts," USGS Professional Paper No. 424D, pp. D216-D218.
- Glendinning, R. M., 1937, "The Slope and Slope-Direction Map," Michigan Papers in Geography, vol. 7, pp. 359-364.
- Goodyear Aerospace Corporation, 1966, Textbook of Radar Interpretation, vol. 1, Basic Radar and Imaging Principles (U) (Secret Report), Goodyear Aerospace Corporation, Litchfield Park, Arizona.
- Goodyear Aerospace Corporation, 1964, "Coherent High-Resolution Radar Interpretation and Analysis Techniques Study (U)," (Secret Report), Technical Documentary Report prepared for the Reconnaissance Data Extraction Branch, Rome Air Development Center, New York, pp. 30-48.
- Grave, Caswell, 1905, "Investigations for the Promotion of the Oyster Industry of North Carolina," Report, US Commissioner of Fish and Fisheries for 1903, pp. 247-341.
- Hammond, E. H., 1954, "Small-Scale Continental Landform Maps," Annals, A.A.G., vol. 44, pp. 33-42.
- Hoag, L. P., 1962, "Location Determinants for Cash-Grain Farming in the Corn Belt," Professional Geographer, no. 3, pp. 1-6.
- Keen, A. Myra, 1958, Sea Shells of Tropical West America, Stanford University Press, Stanford, California, 624 pp.
- Kolb, C. R. and J. R. Van Lopik, 1958, "Geology of Mississippi River Deltaic Plain, Southeastern Louisiana," US Army Corps of Engineers, Waterways Experiment Station, Tech. Report 3-483 and 3-484, 2 vols.
- Langbein, W. B. and L. B. Leopold, 1966, "River Meanders — Theory of Minimum Variance," US Geological Survey Professional Paper 422-H, 15 pp.
- LaPrade, G. L., 1963, "An Analytical and Experimental Study of Stereo for Radar," Photogrammetric Engineering, vol. 29 no. 2, pp. 294-300.
- LaPrade, G. L. and E. S. Leonardo, 1969, "Elevations from Radar Imagery," Photogrammetric Engineering, vol. 35, no. 4, pp. 366-371
- Leonardo, E. S., 1963, "Comparison of Imaging Geometry for Radar and Camera Photographs," Photogrammetric Engineering, vol. 29, no. 2, pp. 287-293.
- Levine, Daniel, 1960, Radargrammetry, McGraw-Hill Book Company, Inc., New York, N.Y., 330 pp.

- Lewis, A. J. and H. C. MacDonald, 1970, "Significance of Estuarine Meanders Identified from Radar Imagery of Eastern Panama and Northwestern Colombia," Modern Geology, vol. 1, no. 4, pp. 187-196.
- MacDonald, H. C., 1970, "Geologic Evaluation of Radar Imagery from Darien Province, Panama," Modern Geology, vol. 1, pp. 1-63.
- MacDonald, H. C. and A. J. Lewis, 1969_a, "Applications of Radar Imagery in Geologic and Geomorphic Reconnaissance of Tropical Environments: Program Abstracts, Geological Soc. Amer. Sectional Meeting, Lawrence, Kansas, p. 18-19, paper presented March 1969; paper also presented IEEE Geoscience Electronics Symposium, Washington, D. C., April 1969.
- MacDonald, H. C. and A. J. Lewis, 1969_b, "Terrain Analysis with Radar — A Preliminary Study: Interim Tech. Progress Report, Fourth Semi-Annual Technical Report," Project THEMIS, October 1969, p. F1-F12.
- MacDonald, H. C., A. J. Lewis, and R. S. Wing, 1971, "Mapping and Landform Analysis of Coastal Regions with Radar," accepted for publication, Geological Soc. Amer. Bulletin.
- MacGregor, P. R., 1957, "Some Observations on the Geographical Significance of Slopes," Geography, vol. 42, pp. 167.
- McAnerney, J. M., 1966, "Terrain Interpretation from Radar Imagery," Proceedings of the 4th Symposium on Remote Sensing of Environment, University of Michigan, Ann Arbor, pp. 731-750.
- McCoy, R. M., 1967, "An Evaluation of Radar Imagery as a Tool for Drainage Basin Analysis," CRES Technical Report 61-31, University of Kansas, Lawrence, Kansas, 101 pp.
- Melton, M. A., 1958, "Correlation Structure of Morphometric Properties and Their Controlling Agents," Journal of Geology, vol. 66, pp. 442-460.
- Moore, R. K., and D. S. Simonett, 1967, "Potential Research and Earth Resource Studies with Orbiting Radars," AIAA Paper No. 67-767, 22 pp.
- Norris, R. M., 1953, "Buried Oyster Reefs in Some Texas Bays," Journal of Paleontology, vol. 27, pp. 569-576.
- Nunnally, N. R., 1969, "Integrated Landscape Analysis with Radar Imagery," Remote Sensing of Environment, vol. 1, no. 1, pp. 1-6.

- Parker, R. H., 1960, "Ecology and Distributional Patterns of Marine Macro-Invertebrates, Northern Gulf of Mexico," Amer. Assoc. Petrol. Geol., pp. 302-327.
- Parry, J. T., J. A. Heginbottom, and W. R. Cowan, 1968, "Terrain Evaluation in Mobility Studies for Military Vehicles," In: Land Evaluation, G. A. Stewart, ed., MacMillan of Australia, pp. 160-170.
- Peltier, L. C., 1954, "Some Properties of the Average Topographic Slope," Annals, Assoc. American Geog., vol. 44, pp. 229-230.
- Peterson, R. M., 1968, "Observations on the Geomorphology and Land Use of Part of the Wasatch Range, Utah: Interim Technical Progress Report, First Semi-Annual Technical Report," Project THEMIS, April 1968, pp. F1-F18.
- Pierson, W. J., Jr., B. B. Scheps, and D. S. Simonett, 1965, "Some Applications of Radar Return Data to the Study of Terrestrial and Oceanic Phenomena," Proceedings of the Third Goddard Memorial Symposium on Scientific Experiments for Manned Orbital Flights, March 1965, Washington, D. C., pp. 87-137.
- Robertson, V. C., et al., 1968, "The Assessment of Land Quality for Primary Production," In: Land Evaluation, G. A. Stewart, ed., MacMillan of Australia, pp. 88-103.
- Salisbury, N. E., 1965, "Landform-Lithologic Relationships in Portions of the Mississippian Plateaus of Kentucky," paper presented at the annual meetings Assoc. American Geog., Columbus, Ohio.
- Salisbury, N. E., 1962, "Relief-Slope Relationships in Glaciated Terrain," paper presented at the annual meetings of the Assoc. American Geog., Miami, Florida.
- Scheps, B. B., 1960, "To Measure is to Know-Geometric Fidelity and Interpretation in Radar Mapping," Photogrammetric Engineering, vol. 26, no. 4, pp. 637-644.
- Schwarz, D. E. and R. D. Mower, 1969, "The Potential for Deriving Land Form Regions from Radar Imagery: A Puerto Rican Example," In: "The Utility of Radar and Other Remote Sensors in Thematic Land Use Mapping from Spacecraft, Annual Report," Technical Letter NASA-140, NASA Contract R-09-020-024, U. S. Geological Survey, pp. 22-35.

- Shaudys, V. K., 1956, "A Study of Selected Geographic Factors Adjacent to Topographic Boundaries in South Central Ohio," unpublished Ph. D. Dissertation, Ohio State University.
- Shepard, F. P. and David Moore, 1956, "Sediment Zones Bordering the Barrier Islands of Central Texas Coast," In: Finding Ancient Shorelines, Society of Economic Paleontologists and Mineralogists, Special Publication No. 3, pp. 79-95.
- Simonett, D. S., 1967, "Landslide Distribution and Earthquakes in the Bewani and Torricelli Mountains, New Guinea," In: Landform Studies from Australia and New Guinea, J. N. Jennings and J. A. Mabbut, eds. Cambridge University Press, New York, pp. 64-84.
- Simons, J. H. and A. P. Beccassio, 1964, An Evaluation of Geoscience Applications of Side-Looking Airborne Mapping Radar, Raytheon/Autometric Corp., Alexandria, Virginia, 70 pp.
- Storie, R. E., 1933, "An Index for Rating of Agricultural Value of Soils," University of Calif. Agr. Exp. St. Bull. 556.
- Strahler, A. N., 1956, "Quantitative Slope Analysis," Geological Society of America Bulletin, vol. 67, pp. 571-596.
- Thompson, W. C., 1956, "Sandless Coastal Terrain of the Atchafalaya Bay Area, Louisiana," In: Finding Ancient Shorelines, Society of Economic Paleontologists and Mineralogists, Special Publication No. 3, pp. 59-76.
- Tuan, Yi-Fu, 1960, "Coastal Landforms of Central Panama," Department of Geography, University of California, Berkeley, Contract ONR-222(11) NR 388 067, AD No. 239 568, 30 pp.
- Vann, J. H., 1959, "Landform-Vegetation Relationships in the Atrato Delta," Annals, Assoc. American Geog., vol. 49, no. 4, pp. 345-360.
- Walters, R. L., 1968, "Radar Bibliography for Geosciences," CRES Technical Report 61-30, University of Kansas, Lawrence, Kansas, 27 pp.
- Wing, R. S., 1970, "Structural Analysis from Radar Imagery, Eastern Panamanian Isthmus," Ph. D. Dissertation, University of Kansas, CRES Technical Report 133-15; accepted for publication Modern Geology, 180 pp.
- Wood, W. F. and J. B. Snell, 1960, "A Quantitative System for Classifying Landforms," U.S. Army, Quartermaster Research Center, Natick, Mass., Technical Report EP-124, 20 pp.

Young, R. N., 1953, "A Geographic Classification of the Land Forms of Puerto Rico," In: Symposium on the Geography of Puerto Rico, C. F. Jones and R. Pico, eds., University of Puerto Rico Press, pp. 24-46.

Zakrzewska, B., 1967, "Trends and Methods in Land Form Geography," Annals, Assoc. American Geog., vol. 57, pp. 128-165.

RADAR IMAGERY



RADAR LANDFORM CLASSIFICATION WITH CUMULATIVE FREQUENCY SLOPE CURVES

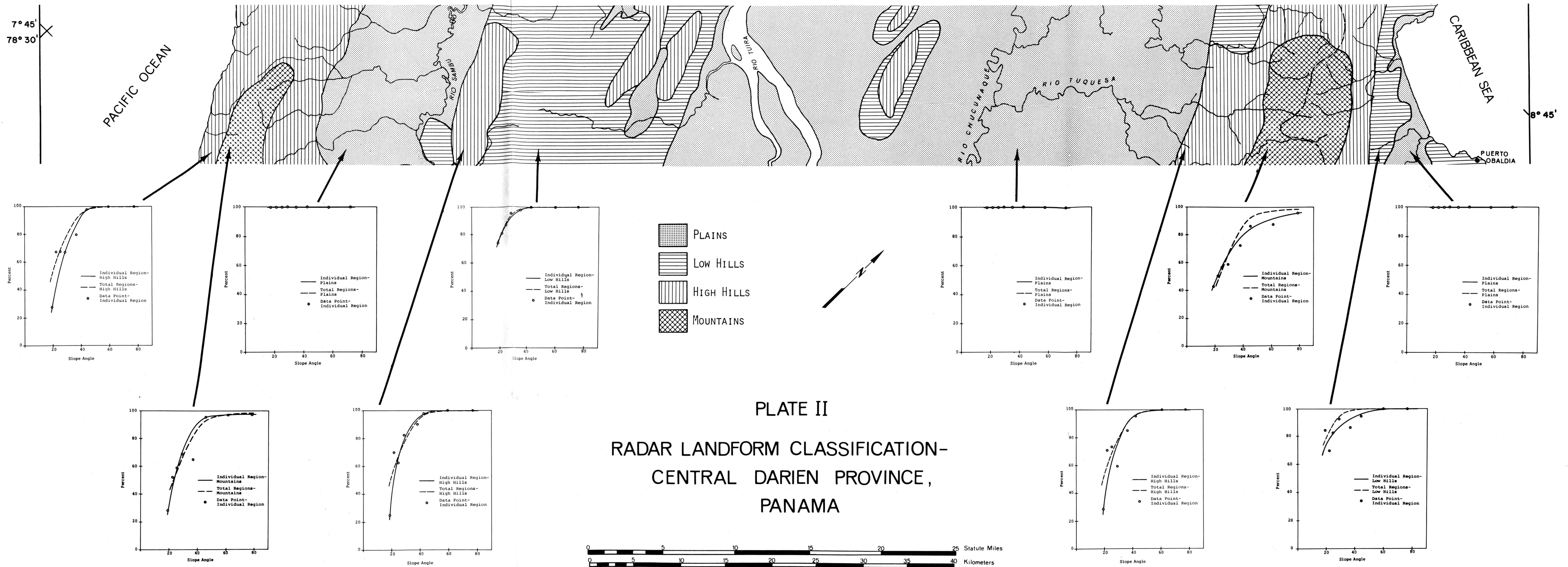
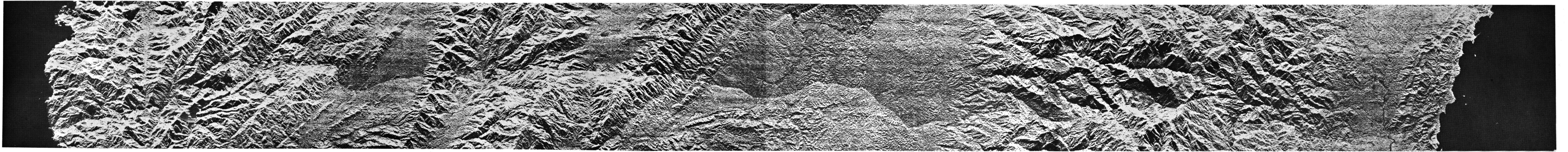


PLATE II

RADAR LANDFORM CLASSIFICATION- CENTRAL DARIEN PROVINCE, PANAMA

RADAR IMAGERY



RADAR LANDFORM CLASSIFICATION WITH CUMULATIVE FREQUENCY SLOPE CURVES

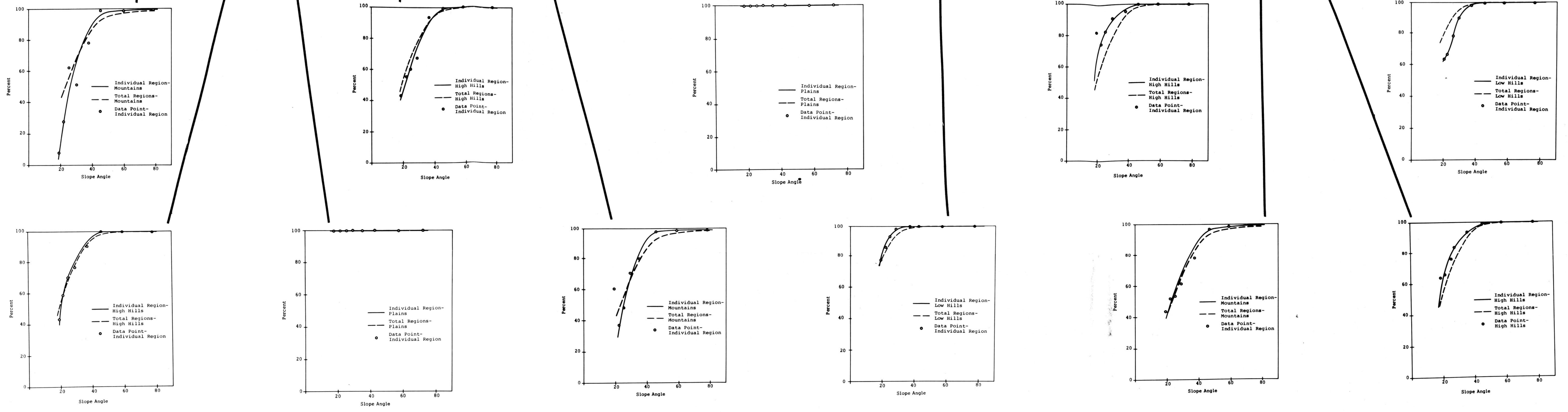
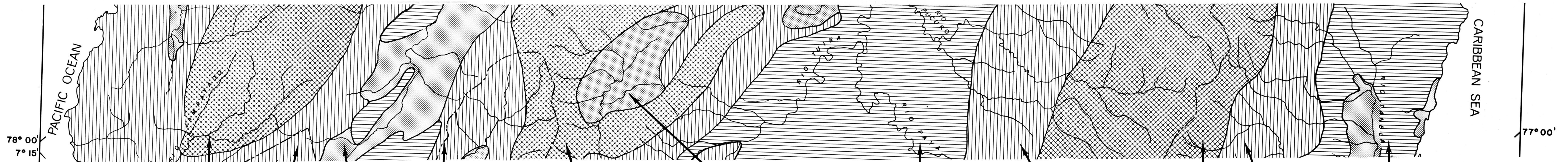


PLATE III

RADAR LANDFORM CLASSIFICATION SOUTHEASTERN DARIEN PROVINCE, PANAMA

